High-power green diode laser systems for biomedical applications

Ph.D. thesis at the Technical University of Denmark

by
André Müller

Supervisors: Professor Paul Michael Petersen
Research Professor Peter Eskil Andersen
Senior Scientist Ole Bjarlin Jensen

DTU Fotonik, Department of Photonics Engineering

June, 2013

Abstract

Due to their unique characteristics, diode lasers are increasingly attractive for numerous applications. For example, in the biomedical field the provided output power, spatial quality, and wavelength coverage of diode lasers has enabled their applications in, e.g., dermatology, diffuse spectroscopy and imaging, and fluorescence measurements. A major challenge in diode laser technology is to obtain high-power laser emission at wavelengths < 600 nm. Especially the green spectral range is of high importance, for example, in dermatology or for direct pumping of ultrashort pulsed lasers in conjunction with optical coherence tomography, two-photon microscopy or coherent anti-Stokes Raman scattering microscopy.

In order to provide high-power green diode laser emission, nonlinear frequency conversion of state-of-the-art near-infrared diode lasers represents a necessary means. However, the obtained output power of frequency doubled single emitters is limited by thermal effects potentially resulting in laser degradation and failure. In this work new concepts for power scaling of visible diode laser systems are introduced that help to overcome current limitations and enhance the application potential.

The underlying principle is spectral beam combining of multiple, comparable diode lasers with subsequent nonlinear frequency conversion. In the former approach multiple lasers are incoherently combined with an external optical component. With two 1062 nm tapered diode lasers and a reflecting volume Bragg grating more than 16 W of output power at combining efficiencies > 93% are obtained. Utilizing the wavelength tunability of diode lasers enables less critical optical alignment compared to lasers limited to specific atomic transitions. It is shown that spectral beam combining does not affect the beam propagation parameters and therefore efficiently increases the brightness of compact and cost-effective diode laser systems.

The condition of overlapping beams is an ideal scenario for subsequent frequency conversion. Based on sum-frequency generation of two beam combined diode lasers a 3.2 fold increase in visible output power compared to frequency doubling of a single emitter is achieved. It is shown that nonlinear frequency conversion significantly improves the spatial quality, which results in 3.9 W of diffraction-limited green light at maximum performance.

In order to increase the output power even further, the developed concept is expanded combining multiple diode lasers in a multiplexed grating. In case of three diode lasers, the unique tunability allows for matching emission wavelengths of simultaneous second harmonic generation and sum-frequency generation. The obtained output power is given by the sum of the individual contributions and indicates the potential for power scaling. Limited mainly by the acceptance bandwidths of nonlinear crystals and the practical realization of multiplexed gratings, this concept can be extended towards higher numbers of simultaneous

nonlinear frequency conversions in advanced, visible, high-power diode laser systems with increased application potential.

In order to prove the application potential of green diode laser systems a frequency doubled tapered diode laser is applied for direct pumping of a mode-locked titanium sapphire laser. The resulting pump efficiencies are reduced to 75% of the values achieved with a commercial green solid state laser. However, due to a superior wall-plug efficiency of the diode laser the overall efficiency of the titanium sapphire laser is improved by a factor of 2. In mode-locked operation, a spectral bandwidth of 112 nm allows for sub-20 fs pulses and proves the potential for future diode based compact and efficient titanium sapphire lasers.

Applying such a diode pumped titanium sapphire laser in optical coherence tomography of the retina and skin shows similar results as obtained by solid state pumped systems. Implementing the developed concept of frequency converted, beam combined diode laser systems will help to overcome the high pump thresholds for ultrabroad bandwidth titanium sapphire lasers, leading towards diode based high-resolution optical coherence tomography with enhanced image quality.

In their entirety, the obtained results clearly strengthen the application potential of diode lasers, including the biomedical field.

Abstrakt

Diodelasere er meget attraktive til mange anvendelser på grund af deres unikke egenskaber. For eksempel i det biomedicinske område gør parametre som høj udgangseffekt, god rumlig kvalitet og fleksibelt bølgelængde-område det muligt at anvende diodelasere i for eksempel dermatologi, diffus spektroskopi og billeddannelse eller fluorescensmålinger.

En stor udfordring i diodelaser teknologi er at opnå højt effekt ved bølgelængder < 600 nm. Især lys ved grønne bølgelængder har stor betydning, for eksempel i dermatologi eller til direkte pumpning af ultrakort pulsede lasere sammen med optisk kohærens tomografi, to-foton mikroskopi eller kohærent anti-Stokes Raman mikroskopi.

En egnet metode til at få høj effekt ved grønne bølgelængder er ikke-lineær frekvenskonvertering af state-of-the-art infrarøde diodelasere. Desværre er frekvensfordobling af enkelte emittere begrænset på grund af termiske effekter som potentielt resulterer i dårligere performance eller ødelagte lasere. I dette arbejde introduceres nye koncepter for effekt skalering af synlige diodelaser systemer, som hjælper med at overvinde de nuværende begrænsninger og styrke anvendelses-potentialet.

Det grundlæggende princip er inkohærent, spektral kombinering af flere sammenlignelige diodelasere med efterfølgende ikke-lineær frekvenskonvertering. Med to 1062 nm taperede diodelasere og et reflekterende volumen Bragg gitter er der opnået mere end 16 W udgangseffekt ved en kombinationseffektivitet > 93%. I forhold til lasere begrænset til bestemte atomare overgange tillader tuningen af diodelaseres bølgelængde mindre kritisk optisk opligning. Det vises, at denne slags inkohærent kombinering ikke påvirker den rumlige kvalitet af laseren og derfor effektivt øger lysstyrken af kompakte og omkostningseffektive diodelaser systemer.

Den resulterende stråle bestående af to overlappende stråler er ideel til efterfølgende frekvenskonvertering. Baseret på sum-frekvens generering af to kombinerede diodelasere er der opnået en 3.2 gange forøgelse i synlig udgangseffekt i forhold til frekvensfordobling af en enkelt emitter. Det vises også at ulineær frekvenskonvertering forbedrer den rumlige kvalitet, hvilket resulterer i 3.9 W diffraktionsbegrænset grønt lys ved maksimal strøm.

For at øge udgangseffekten yderligere, er det udviklede koncept udvidet til kombinering af flere diodelasere i et gitter. Kombineres tre diodelasere kan frekvensfordobling og sum-frekvens generering opnås samtidig og den unikke tunebarhed af diodelasere tillader at generere de samme emissionsbølgelængder for de to uafhængige processer. Den opnåede udgangseffekt er givet ved summen af de enkelte bidrag og indikerer potentialet for effekt skalering. Dette koncept er mest begrænset af den spektrale acceptans af ulineære krystaller og den praktiske realisering af overlappende gitre og kan derfor anvendes til at udvide mod et højere antal samtidige ikke-lineære konverteringer i avancerede, synlige, høj-effekt diodelaser systemer med øget potentiale indenfor mange anvendelser.

For at vise det fordelagtige i anvendelse af grønne diodelaser systemer, anvendes en frekvensfordoblet taperet diodelaser til direkte pumpning af en mode-locked titanium safir laser. Den resulterende pumpe effektivitet reduceres til 75% i forhold til en kommerciel grøn faststoflaser. Imidlertid øger den høje elektro-optiske effektivitet af diodelasere den samlede effektivitet af titanium safir laseren med en faktor to. Mode-locking resulterer i en spektral båndbredde på 112 nm som tillader sub-20 fs pulser og beviser potentialet for fremtidige diodelaser baserede kompakte og effektive titanium safir lasersystemer.
Anvendelse af en diode-pumpet titanium safir laser i optisk kohærens tomografi af nethinden og huden viser sammenlignelige resultater i forhold til kommercielle systemer. Tilføjelse af de udviklede koncepter af frekvenskonverterede kombinerede diodelaser systemer vil hjælpe med at overstige den høje pumpe tærskel for ultrabredbåndede titanium safir lasere og føre til diodelaser baseret optisk kohærens tomografi med høj opløsning og forbedret billedkvalitet.
I deres helhed styrker de opnåede resultater anvendelses-mulighederne af diodelasere, herunder i det biomedicinske område.

Preface

This thesis summarizes the results obtained during my Ph.D. project at DTU Fotonik, Department of Photonics Engineering at the Technical University of Denmark. The work was carried out between March 2010 and February 2013 under supervision of Professor Paul Michael Petersen, Research Professor Peter Eskil Andersen and Senior Scientist Ole Bjarlin Jensen. The project was mainly funded by the PhD program at DTU Fotonik. In addition, equipment and travel expenses were partially funded by the Danish Agency for Science, Technology and Innovation (Grant number 09-076196), FP7 FUN OCT (HEALTH, 2008-12), FP7 FAMOS (ICT, 2012-16), Otto Mønsted Fond, and Oticon Fonden.

During this project I performed the experimental work on spectral beam combining of diode lasers with subsequent nonlinear frequency conversion. Furthermore, I assisted in the development of compact diode laser based systems as pump sources for titanium sapphire lasers and their application in optical coherence tomography.

This thesis was presented for public examination on June 14, 2013 at the Technical University of Denmark. The evaluation committee consisted of Professor Michael Drewsen (Aarhus University), Professor Edik Rafailov (University of Denmark), and Professor Karsten Rottwitt (Technical University of Denmark). Minor corrections have been made to the originally submitted thesis before printing.

Acknowledgement

I would like to take the chance and express my gratitude to my supervisors for their trust, encouragement and support. It was a great pleasure to be part of your group and I'm thankful for our fruitful discussions and for sharing your knowledge and practical expertise. You made this an invaluable experience.

Within this project I had the opportunity to collaborate with colleagues in Berlin and Vienna. I'm especially grateful to Götz Erbert and Bernd Sumpf from Ferdinand-Braun-Insitut, Leibniz-Institut für Höchstfrequenztechnik in Berlin for providing me with state-of-the-art diode lasers for my experimental work and their commitment and helpful advice on technical and scientific matters.

Regarding the practical application of developed laser systems, I really enjoyed the cooperation with colleagues at Femtolasers Produktions GmbH in Vienna. Here I would like to thank Andreas Stingl and Tuan Le for their willingness to investigate the application potential of green diode laser systems as direct pump sources for titanium sapphire lasers.

I am also very thankful for the collaboration with our colleagues at the Medical University of Vienna. I explicitly thank Wolfgang Drexler for the opportunity of joint biomedical experiments and Angelika Unterhuber for her efforts implementing and testing our light source in optical coherence tomography systems.

Finally, I would like to thank all my colleagues at DTU Fotonik for creating such an excellent working atmosphere. I always felt welcome and it was a pleasure to work with you.

Table of contents

List of publications

Peer-reviewed journal publications

1. O. B. Jensen, A. K. Hansen, A. Müller, B. Sumpf, A. Unterhuber, W. Drexler, P. M. Petersen, and P. E. Andersen,
"Nonlinear frequency converted diode lasers for biophotonics,"
IEEE J. Sel. Top. Quantum Electron. **20**, 7100515 (2013).

2. A. Unterhuber, B. Povazay, A. Müller, O. B. Jensen, T. Otto, I. Boettcher, M. Duelk, R. Kessler, R. Engelhardt, M. Esmaeelpour, T. Le, P. E. Andersen, C. Velez, G. Zinser, and W. Drexler,
"Simultaneous dual wavelength eye tracked ultrahigh resolution retinal/choroidal OCT,"
Opt. Lett. **38**, 4312-4315 (2013).

3. A. Müller, S. Marschall, O. B. Jensen, J. Fricke, H. Wenzel, B. Sumpf, and P. E. Andersen,
"Diode laser based light sources for biomedical applications,"
Laser Phot. Rev. **7**, 605-627 (2013).

4. A. Müller, O. B. Jensen, K.-H. Hasler, B. Sumpf, G. Erbert, P. E. Andersen, and P. M. Petersen,
"Efficient concept for generation of diffraction-limited green light by sum-frequency generation of spectrally combined tapered diode lasers,"
Opt. Lett. **37**, 3753-3755 (2012).

5. A. Müller, O. B. Jensen, A. Unterhuber, T. Le, A. Stingl, K.-H. Hasler, B. Sumpf, G. Erbert, P. E. Andersen, and P. M. Petersen,
"Frequency-doubled DBR-tapered diode laser for direct pumping of Ti:sapphire lasers generating sub-20 fs pulses,"
Opt. Express **19**, 12156-12163 (2011).

6. A. Müller, D. Vijayakumar, O. B. Jensen, K.-H. Hasler, B. Sumpf, G. Erbert, P. E. Andersen, and P. M. Petersen,
"16 W output power by high-efficient spectral beam combining of DBR-tapered diode lasers,"
Opt. Express **19**, 1228-1235 (2011).

Conference proceedings

1. A. Müller, O. B. Jensen, K.-H. Hasler, B. Sumpf, G. Erbert, P. E. Andersen, and P. M. Petersen,
"Efficient concept generating 3.9 W of diffraction-limited green light with spectrally combined tapered diode lasers,"
Proc. SPIE **8604**, 860404 (2013).

2. P. E. Andersen, O. B. Jensen, A. Müller, and P. M. Petersen,
"Green, Compact Diode Laser-based Systems for Biophotonics Application,"
Asia Communications and Photonics Conference, OSA Technical Digest (Optical Society of America, 2012), paper AS4E.1.

3. A. Müller, D. Vijayakumar, O. Jensen, K. Hasler, B. Sumpf, G. Erbert, P. E. Andersen, and P. M. Petersen,
"Spectral beam combining of diode lasers with high efficiency,"
Lasers, Sources, and Related Photonic Devices, OSA Technical Digest (Optical Society of America, 2012), paper AM4A.10.

4. A. Müller, O. B. Jensen, A. Unterhuber, T. Le, A. Stingl, K.-H. Hasler, B. Sumpf, G. Erbert, P. E. Andersen, and P. M. Petersen,
"Frequency-doubled diode laser for direct pumping of Ti:sapphire lasers,"
Proc. SPIE **8235**, 82351F (2012).

5. A. Müller, O. B. Jensen, A. Unterhuber, T. Le, A. Stingl, K.-H. Hasler, B. Sumpf, G. Erbert, P. E. Andersen, and P. M. Petersen,
"Direct pumping of ultrashort Ti:sapphire lasers by a frequency doubled diode laser,"
Proc. SPIE-OSA-IEEE Asia Communications and Photonics **8311**, 831110 (2011).

Other contributions

1. O. B. Jensen, P. E. Andersen, P. M. Petersen, and A. Müller,
"Method of stabilizing a laser apparatus with wavelength converter,"
Patent application PCT/EP2012/054338 (2012).

2. A. Müller, O. B. Jensen, P. E. Andersen, and P. M. Petersen,
"Efficient generation of 3.9 W of diffraction-limited green light with spectrally combined tapered diode lasers,"
Oral presentation at Northern Optics 2012.

List of abbreviations

CW	Continuous Wave
RW	Ridge-Waveguide
BA	Broad Area
TA	Tapered Amplifier
DBR	Distributed Bragg Reflector
DFB	Distributed Feedback
COMD	Catastrophic Optical Mirror Damage
DPSS	Diode Pumped Solid State
SHG	Second Harmonic Generation
SFG	Sum-Frequency Generation
QPM	Quasi Phase-Matching
LN	Lithium Niobate
PPLN	Periodically Poled Lithium Niobate
AR	Antireflection
NA	Numerical Aperture
FWHM	Full Width at Half Maximum
SBC	Spectral Beam Combining
PTR	Photo-Thermo-Refractive
VBG	Volume Bragg Grating
DE	Diffraction Efficiency
OCT	Optical Coherence Tomography

This page intentionally left blank

To my parents,
Elke and Thomas

And to Anne,
for your sacrifices, patience, and love

1. Introduction

1.1. Key advantages of diode laser based systems

In 1960 Theodore Maiman demonstrated the first practical realization of a laser [1]. Since then the range of laser applications has increased enormously. Among the different types especially diode lasers became and are increasingly attractive. Compared to optically pumped lasers, such as diode pumped solid state lasers [2], diode lasers are electrically pumped and are by far the most efficient light sources currently available [3],[4]. In addition, chip technology enables to manufacture diode lasers at low cost and in high numbers. Dimensions of a few mm^3 allow for realization of compact laser systems, increasing their application potential.

In the biomedical field the applications of diode based laser systems range from diagnostics and imaging applications, such as optical coherence tomography [5], fluorescence lifetime imaging [6], diffuse optical imaging [7], THz imaging [8] or laser Doppler imaging [9], to direct treatments, such as photocoagulation [10], photo-dynamic therapy [11] or biomodulation/bioactivation [12]. A more detailed review explaining the impact of diode lasers on selected biomedical applications is given in [13].

The application potential of diode lasers is strongly related to their emission properties. Regarding the continuous wave (CW) output power of edge-emitting diode lasers, several watts with nearly diffraction-limited beams are obtained with ridge-waveguide (RW) and tapered diode lasers [14],[15]. At the expense of spatial quality the output power can be increased even further with broad area (BA) diode lasers or diode laser bars and stacks [16],[17]. Additional optical feedback may help to improve the poor spatial properties of these devices [18]. With techniques such as mode-locking or gain-switching, diode lasers can also be operated in pulsed mode, resulting in picosecond pulses with repetition rates in the GHz range [19],[20].

Special types of diode lasers excluded from this work are vertical cavity surface emitting lasers. They are characterized by laser emission normal to the substrate surface and low threshold currents [21]. The limiting factor towards high-power emission with good spatial quality is the heat removal from the short active region [22].

Unlike lasers limited to specific atomic transitions, a much wider spectral range of 400 nm - 2 µm can be accessed by engineering the material composition of diode lasers [23]. Within the gain bandwidth the emission wavelengths can be tuned by injection current or laser temperature [21]. While spectral side-modes are suppressed at higher injection currents [24], improved single-mode emission can be obtained by intrinsic or external feedback [24],[25]. The latter also enables wavelength tuning over several tens of nanometers [26]. Wavelengths not obtained with current technology can be accessed by nonlinear frequency conversion [27]. This also

enables to increase the output power in certain regions such as the green spectral range where obtaining high-power diode laser emission is still challenging.
All aspects such as output power, spatial quality, wavelength coverage and tunability, efficiency, size and production cost, are the reasons for diode laser technology being versatile and increasingly applicable, including the biomedical field.

1.2. Motivation for this work

For all laser applications certain laser parameters need to be fulfilled. As discussed above, diode lasers have proven their superior performance in many of these aspects. Figure 1 gives an overview on the obtained maximum output power (CW) of edge-emitting diode lasers within a spectral range of 300 nm - 1200 nm [13]. Within that range the highest output powers are obtained at near-infrared wavelengths. For example, up to 25 W were achieved with BA lasers between 800 nm - 1000 nm [28]. These lasers are ideally suited for dermatological applications, where output power, emission wavelength and absorption by blood are the key parameters.

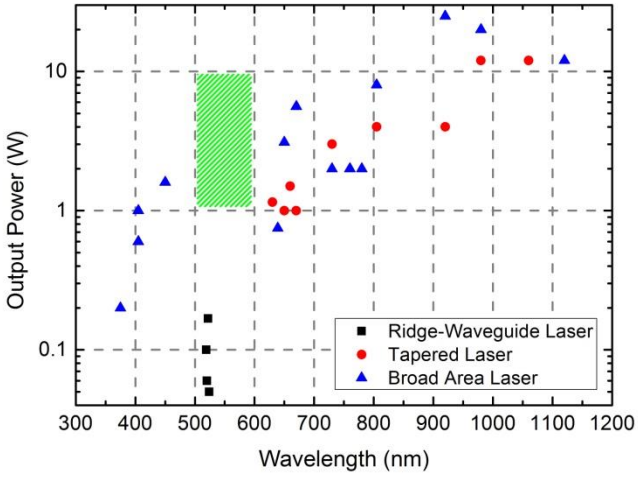

Figure 1: Overview on CW-output power versus emission wavelength reported for BA, RW and tapered diode lasers [13]. The striped rectangular shape between 500 nm and 600 nm indicates one current major challenge in diode laser technology, i.e., obtaining > 1 W of direct laser emission in the green-yellow spectral range.

In the visible spectral range up to 5.6 W were reported for red-emitting BA lasers [29]. Due to their size, efficiency, and low power requirements, red diode lasers are preferred for applications such as diffuse spectroscopy and imaging. At blue emission wavelengths up to 1.6 W were obtained [30], applicable in fluorescence measurements that typically require low power laser emission.

A major challenge in diode laser technology is to obtain high-power emission in the green and yellow spectral range, as indicated by the marked region in Figure 1. Especially green lasers are of high importance in the biomedical field, for example, in dermatology or as direct pump sources of ultrashort pulsed lasers, see below. Nonlinear frequency conversion represents a necessary means to meet this challenge. State-of-the-art 1062 nm tapered diode lasers were reported with up to 12 W of output power and good spatial qualities [31]. These lasers have been shown to be very well suited for efficient, high-power frequency conversion, resulting in 1.58 W of green light [32]. At this level, green diode lasers have a competitive application potential in direct pumping of titanium sapphire (Ti:sapphire) lasers, required for biomedical applications such as two-photon microscopy [33], coherent anti-Stokes Raman scattering microscopy [34], or optical coherence tomography [35]. However, higher performance is required in order to overcome increased pump thresholds for ultrabroad bandwidth Ti:sapphire lasers in high-resolution OCT systems or to address other applications such as photocoagulation in conjunction with vascular diseases [36],[37],[38]. Unfortunately, increasing the output power of single emitter systems is limited by undesired heat effects that may lead to laser failure. The motivation for this work is to overcome these limitations and develop state-of-the-art high-power green diode laser systems. Based on spectral beam combining of comparable lasers and subsequent nonlinear frequency conversion, the developed concepts utilize the unique characteristics of diode lasers and significantly increase the performance of visible diode laser systems by individual or simultaneous nonlinear interactions.
A second motivation is to prove the competitiveness of green diode laser systems in the biomedical field by applying them as direct pump sources for Ti:sapphire lasers in optical coherence tomography (OCT) measurements.

1.3. Structure of this thesis

In the beginning, the chapters 2 and 3 provide a theoretical overview on diode lasers and nonlinear frequency conversion. Based on the example of tapered diode lasers used throughout the work, the basic principle of diode lasers, their vertical structure, and the emission characteristics of diode lasers are discussed.
The large field of nonlinear frequency conversion in this work is restricted to 2^{nd} order phenomena, more precisely, second harmonic generation and sum-frequency generation. The overview on frequency conversion includes the basic concept behind these nonlinear phenomena, a brief discussion of well-established phase-matching techniques, and Boyd-Kleinman theory regarding the optimum focusing condition. All theoretical examples are based on lithium niobate crystals as applied in this work. In addition, alternative nonlinear materials for green light generation and different approaches towards frequency conversion are briefly discussed.

The second part of this thesis summarizes the obtained experimental results. While chapter 4 describes the concept of spectral beam combining, chapter 5 discusses the utilization of this concept in generating multiple watts of green light by efficient sum-frequency generation of spectrally combined diode lasers. Chapter 6 illustrates how multiplexed gratings can be applied in order to efficiently extent this new concept, generating visible laser emission from simultaneous nonlinear interactions.
The final two chapters focus on the application potential of green diode laser systems. While chapter 7 shows the results obtained with direct pumping of ultrashort pulsed Ti:sapphire lasers, chapter 8 summarizes the results achieved in OCT measurements of the retina and skin with a diode pumped Ti:sapphire laser system.
A summary of the obtained results and brief outlooks on power scaling of future visible diode laser systems and their application in OCT measurements concludes this work.

2. Diode lasers

2.1. Basic principle of diode lasers

Compared to other laser types with sharp energy levels, diode lasers are based on broad energy bands. The lower band referred to as the valance band and the upper band referred to as the conduction band are separated by a band gap with the energy E_g. The band gap energy of typical III-V compound semiconductors is in the range of 0.5 eV - 2.5 eV, depending on the material composition. Based on the following relation [21]

$$E_{\text{Photon}} = h\nu = h\frac{c}{\lambda}, \tag{1}$$

the available emission wavelengths λ range from the blue to the near-infrared [23]. Here E_{Photon} is the photon energy, h the Planck constant ($h = 4.135 \cdot 10^{-15}$ eVs), ν the frequency, and c the vacuum speed of light ($c = 3 \cdot 10^8$ m/s).
Without external excitation and at a temperature of $T = 0$ K, the valance band of undoped semiconductors is occupied with electrons while the conduction band is empty. Applying an injection current to the diode increases the concentrations of electrons in the conduction band and electron holes in the valence band. The generation and recombination of these electron-hole pairs enables band to band transitions (Figure 2).

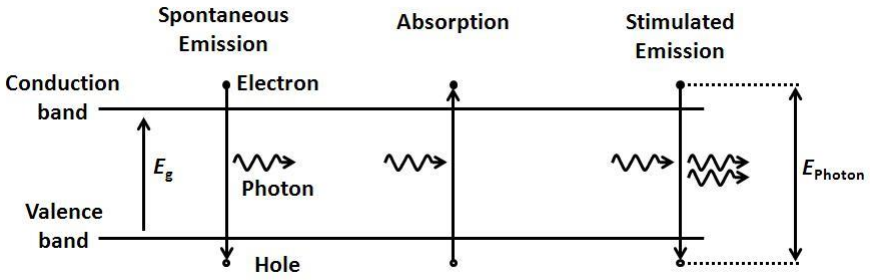

Figure 2: Illustration of three possible band-to-band transitions in diode lasers. While spontaneous and stimulated emissions are caused by recombination of electrons and holes, photon absorption can generate new pairs of electrons and holes.

Spontaneous recombination of electrons and holes results in emission of photons that are random in direction and phase. This principle is utilized in light-emitting diodes. The emitted photons can be absorbed to generate new pairs of electrons and holes. The third transition mandatory for laser operation is stimulated emission. Generated photons stimulate recombination of additional electrons and holes, resulting in simultaneous generation of additional photons that are coherent with the initial photons. In order to obtain an operating laser the stimulated emission needs to

be amplified, compensating losses such as photon absorption. This is referred to as threshold condition. It is obtained by population inversion, i.e., the number of electrons in the conduction band needs to exceed the number in the valence band, and by positioning the laser medium inside a resonant cavity providing optical feedback. For diode lasers the cavity is typically constructed between the coated end facets of the diode. While the rear facets typically show high reflectivities (R_r > 90%), the high gain of diode lasers allows for front facets that can be anti-reflection coated ($R_f \leq 1\%$) [31].

2.2. Vertical structure and edge-emitting laser devices

The basic elements for diode lasers are a medium providing optical gain by stimulated emission, a resonant cavity for optical feedback, an optical waveguide confining the photons to the active region, and lateral confinement of photons, injection current and carriers [21]. Most diode lasers are based on p-i-n double heterostructures consisting of an un-doped semiconductor layer embedded between p- and n-doped semiconductors with higher band gaps (Figure 3). This structure has the advantage that injected carriers are confined between the barriers in the conduction and valence bands. The intrinsic layer therefore acts as the active region providing optical gain. In addition, the lower refractive indices of larger band gap semiconductors result in optical wave guiding in vertical direction.

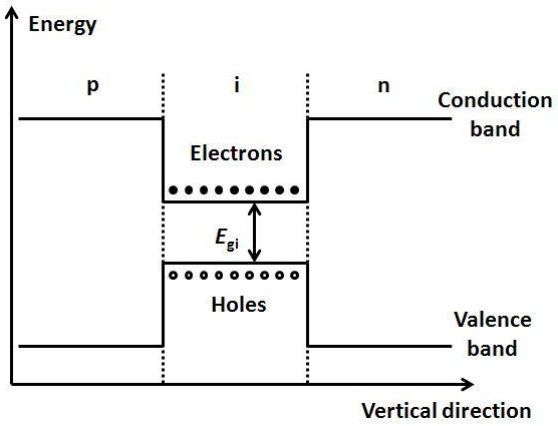

Figure 3: Energy band diagram of a p-i-n double heterostructure. This type of structure enables carrier confinement between the barriers of p- and n-doped semiconductors and provides optical wave guiding in vertical direction.

The active region can be based on a number of quantum wells or quantum dots. Figure 4 shows the vertical layer structure of 1062 nm diode lasers applied in this work. The active region of these lasers is composed of a triple indium gallium arsenide (InGaAs) quantum well in a super large optical cavity [15]. Super large

optical cavities are characterized by a few micron high waveguide cores that reduce the vertical far field divergence [39], posing a potential issue when collimating the laser emission. The high number of quantum wells compensates the related reduction of the overlap between the optical field and the active region, improving the efficiency of the lasers [15].

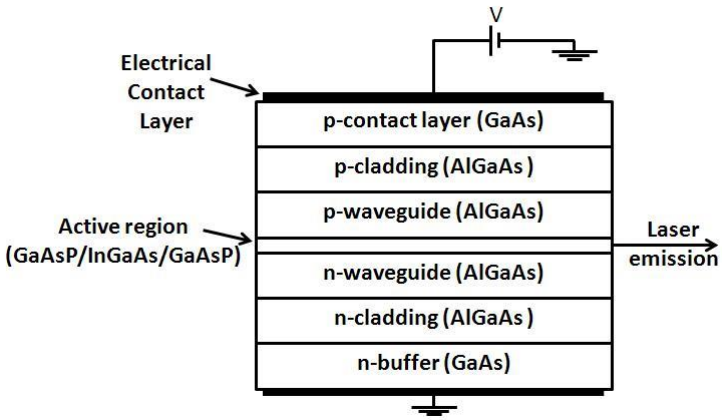

Figure 4: Vertical layer structure of diode lasers based on the example of 1062 nm diode lasers as applied in this work [40]. The active region is sandwiched between p- and n-side aluminum gallium arsenide (AlGaAs) waveguides surrounded by cladding layers. A highly doped contact layer completes the p-side.

The vertical layer structures of diode lasers are grown by different techniques such as metal organic vapour phase epitaxy [41] or molecular beam epitaxy [42]. Afterwards these structures are processed into different laser devices. First the stripe width is defined along which the light is gain- or index-guided in lateral direction of the device.

Gain-guiding is enabled by defining a current aperture in the contact layer that spatially limits the carrier injection [21]. Optical waves outside this aperture experience high losses, resulting in lateral confinement of generated laser emission. Gain-guiding is typical for BA lasers where stripe widths of a few hundred microns enable tens of watts of output power [43]. Several emitters can be combined within a laser bar to increase the output power even further [17]. One disadvantage of such BA lasers is the poor spatial quality of their emission, caused by high-order lateral modes in the wide active region [44].

A better spatial quality is obtained in index-guided devices. Index-guiding is based on an induced refractive index step in lateral direction. The resulting ridge provides additional wave guiding in lateral direction [21]. The spatial mode characteristic of a three-layer waveguide is determined by the normalized waveguide thickness D [24], given by

$$D = d\frac{2\pi}{\lambda}\sqrt{n_{\text{core}}^2 - n_{\text{cladding}}^2}. \quad (2)$$

Here *d* represents the core dimension of the waveguide and *n* the refractive index. In such a waveguide single mode propagation is obtained at $D < \pi$. In diode lasers this condition is typically satisfied in vertical direction. By optimizing the width and etching depth of the ridge, index-guided lasers potentially enable single lateral mode emission. Index-guiding is typical for a few microns wide RW lasers providing output powers of a few watts [14].

In addition to gain- and index-guiding that provide current and optical confinement, respectively, buried heterostructures also provide carrier confinement. This prevents a lateral diffusion of carriers by introducing additional current blocking layers and therefore lowers the laser threshold [21].

The most promising concept towards high output power and improved spatial quality is the tapered laser [45]. In these devices laser emission from a RW section is monolithically coupled into a flared section, acting as a passive amplifier. This tapered amplifier (TA) is typically gain-guided. The mode-area in the flared section broadens at an angle chosen with respect to the diffraction of the beam leaving the RW. Therefore, the tapered section amplifies the emission while maintaining the single lateral mode profile provided by the ridge-waveguide. Based on the above shown vertical structure, 6 mm long distributed Bragg reflector (DBR)-tapered diode lasers were reported with up to 12 W and nearly diffraction-limited beams [31]. The layout of a DBR-tapered diode laser applied in this work is illustrated in Figure 5. The 6 mm long diode laser consists of a 1 mm passive DBR grating serving as wavelength selective rear side mirror, a 1 mm RW section and 4 mm TA with a tapered angle (φ_{TA}) of 6°. The injection currents to the RW and TA are controlled separately, enabling independent control of output power, spatial quality, and spectral behavior [31]. A more detailed explanation of the intrinsic DBR grating is given in section 0.

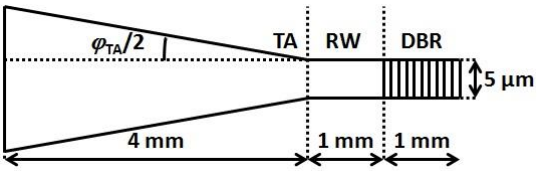

Figure 5: Layout of a DBR-tapered diode laser as applied in this work.

After the processing and metallization of diode lasers they are cut according to the desired length and their facets are coated. The lasers are then mounted on heat spreaders and different actively or passively cooled mounts. A common approach is p-side down mounting to lower the thermal resistance [46]. Long lasers with reduced thermal resistance also enable p-side up mounting to lower mounting induced stress [31]. In order to enable separate control of the RW and TA without

using structured contacts the lasers applied in this work are mounted p-side up on a copper tungsten heat spreader. The heat spreader itself is mounted on a conduction cooled package mount with a 25 mm x 25 mm footprint.

2.3. Emission characteristics of diode lasers

2.3.1. Power characteristics

In lasers the generated emission needs to be amplified by stimulated emission in order to compensate all losses occurring within the resonant cavity. For a Fabry-Pérot resonator, consisting of two mirrors separated from another by the length L, this threshold condition [21] is expressed by

$$\Gamma g_{\mathrm{th}} = \alpha_{\mathrm{i}} + \alpha_{\mathrm{mirror}} = \alpha_{\mathrm{i}} + \frac{1}{2L} ln\left(\frac{1}{R_1 R_2}\right). \tag{3}$$

Here Γg_{th} represents the modal gain, given by the product of the threshold material gain g_{th} and the confinement factor Γ. The latter depends on the overlap of the optical mode-pattern with the active region of the diode laser. α_{mirror} represents the combined photon losses at the diode laser end facets and α_{i} the losses by intrinsic absorption, respectively. The reflectivities of the end facets are expressed by R_1, and R_2. It can be seen that the threshold is reduced by increasing the length of the gain medium and the reflectivities of the resonant cavity. However, choosing the proper reflectivities is crucial with respect to performance and lifetime.
Once the threshold condition is obtained, the output power P shows a linear dependence on the injection current I [21], according to

$$P = \eta_{\mathrm{i}} \frac{\alpha_{\mathrm{mirror}}}{\alpha_{\mathrm{i}} + \alpha_{\mathrm{mirror}}} \frac{h\upsilon}{q} (I - I_{\mathrm{th}}) = \eta_{\mathrm{d}} \frac{h\upsilon}{q} (I - I_{\mathrm{th}}). \tag{4}$$

Here η_{i} represents the internal efficiency, i.e., the fraction of the injection current generating carriers in the active region. q is the elementary charge of electrons (q = 1.602·10^{-19} C), I_{th} the threshold current and η_{d} the differential efficiency. The latter defines how many photons are generated with respect to the injected electrons per time and is given by

$$\eta_{\mathrm{d}} = \frac{\mathrm{d}P}{h\upsilon} \frac{q}{\mathrm{d}I}. \tag{5}$$

Here dP/dI is the slope efficiency in W/A. Figure 6 shows a typical power current characteristic for a 1062 nm DBR-tapered diode laser as introduced above. The laser is operated at a laser temperature of T = 20 °C and an injection current to the ridge section of I_{RW} = 300 mA. The injection current to the tapered amlifier (I_{TA}) is increased in 1 A steps. The measurement shows a threshold current of 2 A. The maximum output power of 10.8 W at 16 A results in a slope efficiency of 0.8 W/A.

The corresponding wall-plug efficiency, i.e., the electro-optical efficiency, is in the range of 30%.

Despite high wall-plug efficiencies [3],[4], the output power of diode lasers is mostly limited by heat effects. Increased temperatures in the active region reduce the carrier confinement and increase the amount of non-radiative recombinations [47]. These effects increase the threshold current and lower the differential efficiency. This potentially causes a reversible thermal rollover in the power-current characteristics before the diode lasers are destroyed by catastrophic optical mirror damage (COMD). Without COMD the lifetimes of diode lasers can exceed 10,000 h [48]. In Figure 6 it can be seen that the 1062 nm DBR-tapered diode lasers do not show signs of thermal rollover or COMD within the specified current range.

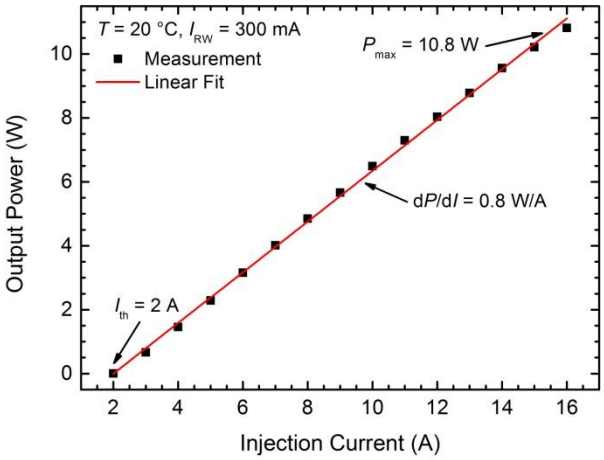

Figure 6: Power current characteristic of a 1062 nm DBR-tapered diode laser at T = 20 °C and I_{RW} = 300 mA.

2.3.2. Spectral properties

As mentioned above, laser operation requires optical feedback in resonant cavities of the length L. Resonant feedback in a Fabry-Pérot resonator is based on the development of standing waves. This requires

$$L = m\frac{\lambda_0}{2n_{\text{eff}}}, \tag{6}$$

with m being the order number of the longitudinal modes (m = 1, 2, 3, ...), λ_0 the vacuum wavelength, and n_{eff} the effective refractive index of the waveguide inside the diode laser [21]. Fabry-Pérot resonators allow multiple longitudinal modes separated by the free spectral range. In a gain medium above threshold only the longitudinal modes closest to the maximum modal gain are amplified. In diode lasers a gain-spectrum wider than the FSR enables multimode emission [24].

Although side-modes are to some extent suppressed at high injection currents, additional techniques are required in order to obtain single-mode emission preferred for certain applications. For example, the emission spectra of diode lasers can be narrowed by external or internal gratings. In external cavity configurations an anti-reflection coated facet enables wavelength selective optical feedback provided by an external grating [49]. Two well-established techniques are Littrow and Littman-Metcalf configurations. In a Littrow configuration the first order diffraction of a flexible external grating is coupled back to the diode [25]. In Littman-Metcalf configurations a combination of a fixed grating and a flexible mirror are used [50],[51]. Both configurations enable wavelength tuning over several tens of nanometers [26].

Compared to these external approaches, distributed feedback (DFB)-lasers or DBR-lasers provide intrinsic wavelength stabilization. In DFB-lasers the feedback is distributed throughout the device by introducing periodic perturbations of the refractive index along the length of the active region [52]. The underlying principle for selective feedback is Bragg scattering. The Bragg condition

$$2\Lambda \sin\theta = m\lambda_B, \tag{7}$$

with Λ being the grating period, θ the angle of incidence, m the order of Bragg diffraction (m = 1, 2, 3, ...), and λ_B the Bragg wavelength [53], implies that counter propagating waves inside the cavity couple coherently only at $\Lambda = m\lambda_B/2$ [24]. Proper engineering of the grating period consequently provides selective feedback, resulting in spectral single-mode emission. In DBR-lasers Bragg scattering is limited to regions beyond the active region and the passive intrinsic gratings act as wavelength selective mirrors of the resonator [54].

The DBR-tapered diode lasers applied in this work are based on 6^{th}-order surface gratings with periods of about 1 µm and duty cycles of 0.9 [15],[55]. The gratings are produced by stepper lithography. Compared to low order gratings these high order gratings are characterized by a lower number of reflecting elements (grooves). The low number of grooves reduces the reflectivity which can be compensated by optimizing the duty cycle [15]. In addition a low number of grooves allows for further simplification of the fabrication process suitable for cost-effective mass production [56]. It is also assumed that a resulting improvement of the overlap of the fundamental mode with the grating and reduced scattering losses compensate the reduced reflectivity of these gratings. In order to solely provide optical feedback from the intrinsic gratings, the rear facets of the applied lasers are anti-reflection coated ($R_r < 10^{-3}$%). The front facets have a reflectivity of R_f = 0.5%.

Figure 7 shows a typical spectrum of a 1062 nm DBR-tapered diode laser at T = 20 °C, I_{RW} = 300 mA, and I_{TA} = 16 A. All spectra in this work are measured with an optical spectrum analyzer (*Advantest Q8347*) that has a maximum resolution of 1 pm - 10 pm within a wavelength range of 500 nm - 1550 nm, respectively, and a dynamic range of 35 dB. Due to the intrinsic wavelength stabilization spurious

spectral modes are not reflected back into the tapered section, resulting in a significantly narrowed spectral width of $\Delta\lambda_{FWHM} \leq 10$ pm. In addition, a side-mode suppression ≥ 20 dB is obtained.

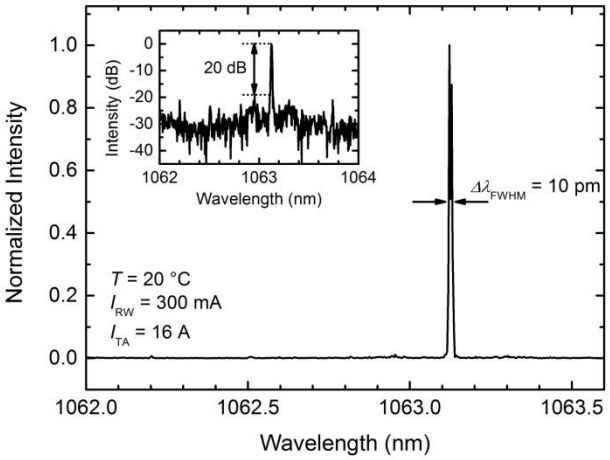

Figure 7: Spectrum of a 1062 nm DBR-tapered diode laser at T = 20 °C, I_{RW} = 300 mA, and I_{TA} = 16 A. The inset shows the same spectrum on a logarithmic scale. FWHM: abbreviation for full width at half maximum.

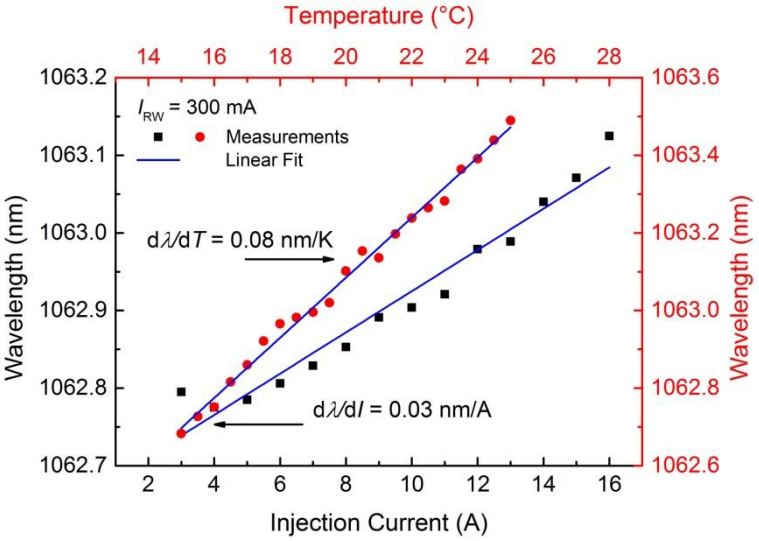

Figure 8: Emission wavelength of a 1062 nm DBR-tapered diode laser versus injection current (bottom-left) and temperature (top-right), measured at 20 °C or at I_{TA} = 16 A, respectively.

One unique characteristic of diode lasers is an emission wavelength tunable with temperature or injection current [21]. Both mechanisms affect the length of the device as well as the temperature dependent refractive index, shifting the emission

wavelength according to equation (6). Figure 8 illustrates that the emission wavelength of a 1062 nm DBR-tapered diode laser changes with approximately 0.03 nm/A and 0.08 nm/K, respectively. This feature enables wavelength tuning applicable in applications such as frequency conversion or beam combining.

2.3.3. Spatial characteristics

Due to the facet dimensions of diode lasers and diffraction at the facets, laser emission leaving the resonator diverges differently in both transverse directions, which results in elliptical emission profiles. The narrow waveguides in vertical direction result in large divergence angles. The corresponding axis is referred to as fast axis. The lateral direction is referred to as slow axis and shows a reduced divergence.

Depending on the lateral structure, diode lasers can additionally show astigmatic laser emission (Figure 9). For example, beams along the fast axis of tapered diode lasers experience vertical wave-guiding and diverge from the laser facet. Beams along the slow axis experience diffraction when coupled into the TA. This results in curved wave fronts in lateral direction. Due to this lateral curvature and diffraction at the laser facet, slow axis beams seem to originate from a virtual source inside the device [57]. The distance of that virtual source to the laser facet is referred to as astigmatism, approximately given by the ratio of the tapered amplifier length and its refractive index (L/n_{eff}) [23]. For example, the astigmatism of the applied 1062 nm DBR-tapered diode lasers is in the range of 1.4 mm.

The astigmatism of tapered diode lasers slightly increases with the injection current, probably caused by changes in the transverse refractive index profile [23],[44]. Most applications such as frequency conversion preferably require collimated laser sources with circular emission profiles and corrected for astigmatism. In practice this is often obtained by collimating the two axes separately and operating the laser at a fixed or maximum current. The power available for further experiments can then be adjusted, e.g., by using a waveplate and a polarizer.

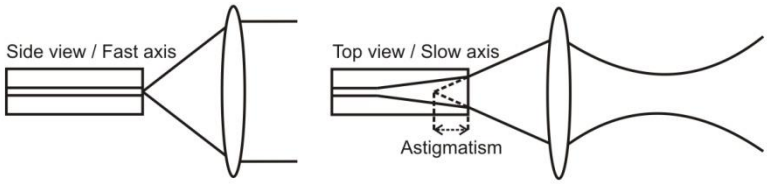

Figure 9: Side and top view of an astigmatic beam emitted by a tapered diode laser. Using a lens, the beam is collimated in the fast axis but focused to a waist in lateral direction. An additional cylindrical lens can be applied to collimate the beam along the slow axis as well.

An additional important parameter of lasers is the beam parameter product (BPP). A focused beam is mainly described by its beam waist w_0 and its divergence θ,

illustrated in Figure 10. The BPP is given by the product of these two parameters. In case of diffraction limited Gaussian beams the BPP results in the following relation [58]

$$w_0\theta = \frac{\lambda}{\pi}. \tag{8}$$

For beams with higher order modes the BPP is increased by a factor M^2. For each transverse axis the M^2 value therefore indicates to what extent the corresponding laser emission differs from an ideal Gaussian beam ($M^2 = 1$).
The propagation of a Gaussian beam along its beam waist is given by [53]

$$w(z) = w_0\sqrt{1 + \left(\frac{z}{z_R}\right)^2}. \tag{9}$$

Here z_R is the Rayleigh length that refers to the distance at which the beam radius $w(z)$ is increased by a factor of $\sqrt{2}$ with respect to the beam waist. Twice that length determines the confocal parameter b. The Rayleigh length is given by the following relation

$$z_R = \frac{\pi w_0^2}{\lambda}. \tag{10}$$

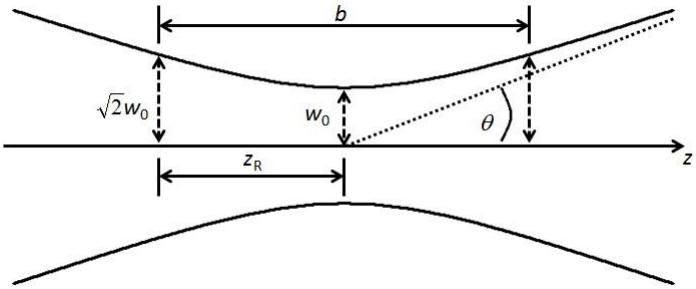

Figure 10: Beam propagation of a focused beam defined by its beam waist and the divergence angle.

Different approaches can be applied in order to measure the M^2 values of a laser beam. Two common criteria are the $1/e^2$ method and the variance definition. For measurements reported in this work a collimated laser is focused by an additional lens. The beam diameters are then measured along the generated beam waist. Using the $1/e^2$ criteria, the beam diameter is defined as the width where the intensity has dropped to 13.5% of its maximum. In order to obtain the M^2 values the beam widths are measured at multiple positions inside and outside the Rayleigh length. The applied hyperbolic fit for the measured widths is given by modifying equation (9):

$$d(z) = d_0 \sqrt{1 + \left(\frac{4M^2 \lambda (z - z_0)}{\pi d_0^2} \right)^2}. \tag{11}$$

Here d_0 and z_0 are the beam waist diameter and its position, respectively.
Figure 11 shows the results for a 1062 nm DBR-tapered diode laser at T = 20 °C, I_{RW} = 300 mA, and I_{TA} = 16 A, measured with a beam scanner (*Photon, Inc.*). From the location of the beam waist it can be seen that the laser is corrected for astigmatism. The measured values are M^2 = 2 in the slow axis and M^2 = 1.5 in the fast axis. From the beam waist profiles the power contents in the central lobe ($1/e^2$) can be estimated, resulting in 73.4% and 88.6% in lateral and vertical direction, respectively.

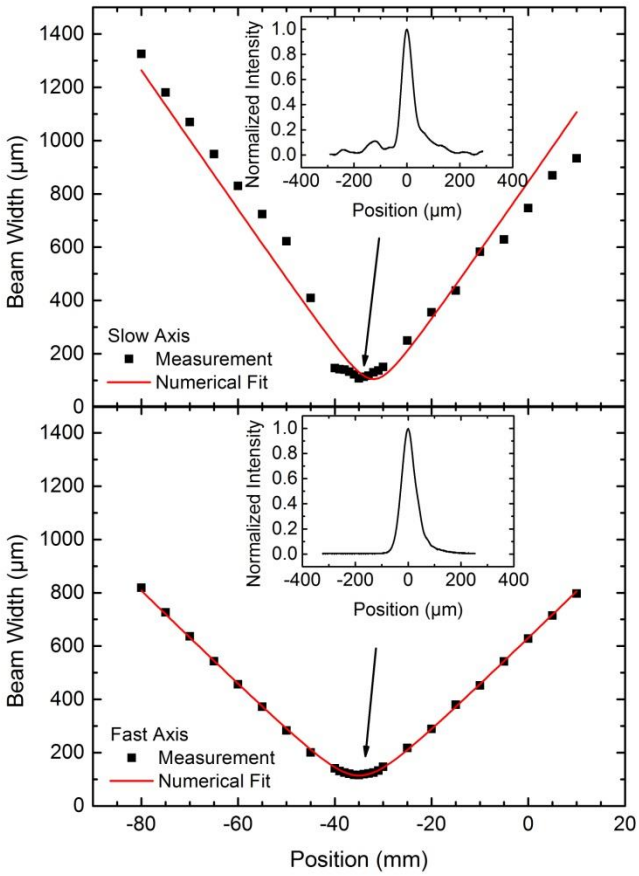

Figure 11: Beam widths of a 1062 nm DBR-tapered diode laser measured along the beam waist according to the $1/e^2$ criteria. The images show the measurements in the slow axis (top) and fast axis (bottom). The laser is operated at I_{RW} = 300 mA, I_{TA} = 16 A and T = 20 °C. The insets show the corresponding beam waist profiles.

The lateral beam waist profile shown in Figure 11 illustrates the major drawback of the $1/e^2$ method. As the Gaussian beam emitted by the RW propagates through the TA, the gain along the propagation axis saturates due to higher intensities in the center of the beam [57]. This results in an increased gain towards the edges of the TA, leading to a top-hat like intensity distribution. Deviations from an ideal top-hat profile can be caused by fabrication induced strains at the edges of the TA or non-uniformities in the electrical or optical material properties. The beam waist intensity profile of such a beam can show noticeable side-lobes, as seen in Figure 11. By measuring the $1/e^2$ values closest to the maximum intensity these side-lobes are neglected and result in improved M^2 values.

A more accurate definition of beam widths is the variance definition, weighing the outer wings. This method is based on the second moments σ^2 of the beam widths that are obtained by integration over the entire intensity profiles [58] according to

$$\sigma_x^2 = \frac{\int_{-\infty}^{\infty}(x - x_0)^2 I(x,y)\mathrm{d}x\mathrm{d}y}{\int_{-\infty}^{\infty} I(x,y)\mathrm{d}x\mathrm{d}y}. \tag{12}$$

Here x_0 is the center of the beam along one transverse axis. The square root of the second moments is the standard deviation σ. With the second moment based beam radii, corresponding to $W = 2\sigma$ [58], the hyperbolic fit for the measured beam widths in equation (11) can be changed to

$$D_{4\sigma}(z) = D_{0,4\sigma}\sqrt{1 + \left(\frac{4M_{4\sigma}^2\lambda(z - z_0)}{\pi D_{0,4\sigma}^2}\right)^2}. \tag{13}$$

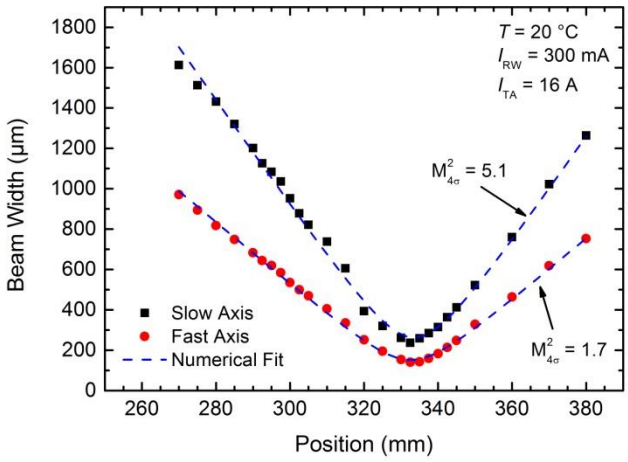

Figure 12: Beam widths of the same 1062 nm DBR-tapered diode laser as in Figure 11 measured according to the second moments criteria.

In comparison to the $1/e^2$ method, measurements with a commercial system (*Spiricon M²-200s*) for the same laser result in $M^2_{4\sigma} = 5.1$ and $M^2_{4\sigma} = 1.7$ in lateral

and vertical direction, respectively (Figure 12). While the M^2 value in the fast axis is comparable to the $1/e^2$ method, the value in the slow axis is significantly increased.
It is shown that DBR-tapered diode lasers provide high-power laser emission with narrow spectral bandwidths and reasonably good spatial quality. This makes them highly attractive laser sources for efficient, high-power frequency conversion as discussed in the following chapter.

3. Frequency conversion

Typical III-V compound semiconductors provide emission wavelengths from the blue to the near-infrared spectral range. However, the output power at certain wavelengths can be limited. Nonlinear frequency conversion represents a means to overcome these limitations [59]. In conjunction with the spectral range accessible with diode lasers, frequency conversion enables compact and efficient laser systems giving access also to new emission wavelengths. This chapter provides an overview on the fundamental aspects of frequency conversion.

3.1. Basic concept of nonlinear frequency conversion

3.1.1. Frequencies of the induced polarization

An electromagnetic wave incident on a material induces an oscillating polarization. The relation between the induced polarization P and the applied electric field E associated with the wave is described by the power series [27]

$$P(z,t) = \varepsilon_0\left[\chi^{(1)}E(z,t) + \chi^{(2)}[E(z,t)]^2 + \chi^{(3)}[E(z,t)]^3 + \ldots\right]. \quad (14)$$

Here ε_0 is the vacuum permittivity (ε_0 = 8.85·10^{-12} F/m). The first term in that relation represents the linear material response determined by the linear susceptibility $\chi^{(1)}$. The induced polarization oscillates at the same frequency as the incident wave. A linear response gives rise to linear phenomena such as dispersion or absorption.

The other terms represent nonlinear responses. The second term including the second-order nonlinear susceptibility $\chi^{(2)}$ describes second-order phenomena such as second harmonic generation (SHG) or sum-frequency generation (SFG). The third-order nonlinear susceptibility $\chi^{(3)}$ gives rise to third-order phenomena such as the intensity dependent refractive index or third harmonic generation. In this work the focus is on second-order nonlinear interactions. The time-varying electric field of a plane wave propagating in z-direction at a frequency ω can be written as [60]

$$E(z,t) = Ae^{i(kz-\omega t+\varphi)} + c.c., \quad (15)$$

with A being the amplitude, k the wave vector, φ the phase and c.c. indicating the complex conjugate. In case of SHG in a $\chi^{(2)}$ material, the second-order nonlinear polarization $P^{(2)}$ depends on the square of the incident electric field, which results in the following relation

$$P^{(2)}(z,t) = \varepsilon_0\chi^{(2)}\left[2AA^* + \left(A^2e^{2i(kz-\omega t+\varphi)} + c.c.\right)\right]. \quad (16)$$

According to this relation the induced second-order nonlinear polarization consists of contributions at zero frequency and $\pm 2\omega$. The former contribution leads to a static electric field within the medium, a process known as optical rectification. The latter contribution leads to the generation of second harmonic waves. In that case two

fundamental photons are replaced with one photon of twice the frequency, i.e., half the emission wavelength (Figure 13).

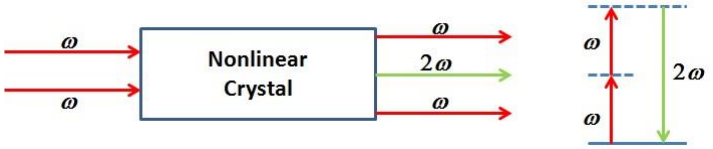

Figure 13: Illustration and energy-level diagram in case of second harmonic generation. Based on conservation of energy, two photons of the fundamental wave with a frequency ω are replaced with one photon of twice the frequency.

In case of two incident fields with different frequencies (ω_1, ω_2), the nonlinear polarization consists of frequency components at $\pm 2\omega_1$, $\pm 2\omega_2$, $\omega_1+\omega_2$, $\omega_2-\omega_1$ and 0. Besides generating the second harmonics of the individual fundamental waves, this scenario also enables sum-frequency generation (SFG) and difference-frequency generation (DFG), which are illustrated in Figure 14. The types of nonlinear interactions taking place is limited by experimental conditions known as phase-matching, as explained in section 0.

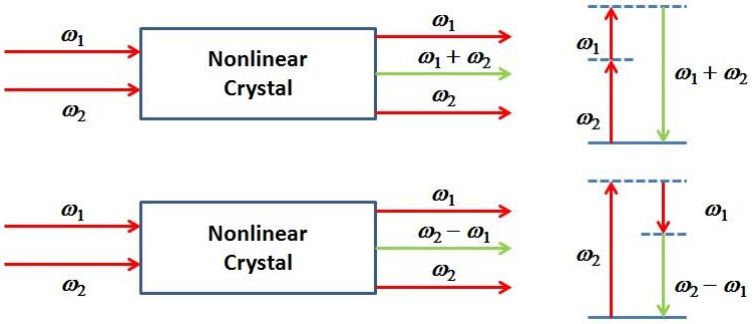

Figure 14: Illustrations and energy-level diagrams for SFG (top) and DFG (bottom). In case of SFG the frequency of a generated photon is given by the sum of the fundamental frequencies ω_1 and ω_2. In case of DFG the frequency of a generated photon is given by the frequency difference of the incident photons.

3.1.2. The nonlinear coefficient

For simplicity, the discussion above completely neglected the vector nature of the electric field and nonlinear polarization. Both can be represented by three scalar components in a Cartesian coordinate system. Second-order nonlinear interactions are based on two incident photons. Therefore, nine possible combinations of scalar components of the electric fields contribute to three scalar components of the

nonlinear polarization. As a consequence $\chi^{(2)}$, describing the relation between the incident fields and the second-order nonlinear polarization, consists of 27 components.
In the literature $\chi^{(2)}$ is often replaced by the nonlinear coefficient d with $d_{ijk} = \chi^{(2)}_{ijk}$. In case of SHG and most cases of SFG the indices j and k, related to the incident waves, are interchangeable and a contracted notation of d represented by an 18 element matrix can be applied ($d_{il} = 0.5\ \chi^{(2)}_{ijk}$). Fortunately, due to different symmetries the number of d components can often be reduced even further [60]. For example, in case of a lithium niobate (LN) crystal, a common nonlinear material for green light generation and applied in this work, the nonlinear coefficient is represented by the following matrix

$$\begin{bmatrix} 0 & 0 & 0 & 0 & d_{15} & -d_{22} \\ -d_{22} & d_{22} & 0 & d_{15} & 0 & 0 \\ d_{31} & d_{31} & d_{33} & 0 & 0 & 0 \end{bmatrix}. \tag{17}$$

SHG with a z-polarized fundamental wave (E_z) therefore results in

$$P_z(2\omega) = 2\varepsilon_0 d_{33}[E_z(\omega)]^2. \tag{18}$$

The induced polarization is also polarized in z-direction (P_z) and the nonlinear interaction is based on the nonlinear coefficient d_{33}. Generating green light the utilization of that coefficient is often preferred, being the largest in crystals typically applied for this interaction [60].

3.1.3. Intensity of the generated wave

The intensity of generated waves is calculated using the nonlinear wave equation [61]

$$-\nabla^2 E + \frac{n^2}{c^2}\frac{\partial^2 E}{\partial t^2} = -\frac{1}{\varepsilon_0 c^2}\frac{\partial^2 P}{\partial t^2}. \tag{19}$$

Here ∇ is a differential operator. Using an example with fields only depending on the z coordinate, this operator can be replaced by d^2/dz^2. The nonlinear wave equation indicates that the induced polarization acts as a source for an electric field in the nonlinear medium. In case of SHG, the nonlinear polarization

$$P_2(z,t) = 2\varepsilon_0 d_{\text{eff}} A_1^2 e^{i(2k_1 z - 2\omega_1 t + 2\varphi_1)} \tag{20}$$

gives rise to an electric field [60]

$$E_2(z,t) = A_2 e^{i(k_2 z - \omega_2 t + 2\varphi_1)}. \tag{21}$$

Here d_{eff} represents the effective, i.e., applied nonlinear coefficient, and A_1 and A_2 the amplitudes of the fundamental and second harmonic waves, respectively. Solving the nonlinear wave equation for this example results in a coupled amplitude equation

$$\frac{dA_2}{dz} = i\frac{\omega_2 d_{\text{eff}}}{n_2 c} A_1^2 e^{i\Delta kz}, \tag{22}$$

with Δk being the wave vector mismatch ($\Delta k = 2k_1 - k_2$) and n the refractive index. A more detailed derivation is provided in [27]. The phase of the incident field is canceled during the derivation, indicating the coherent nature of the generated emission. It should be noted that the derivation is based on the slowly-varying amplitude approximation. This approximation, described in the appendix, is valid for amplitudes changing minimally with the propagation direction over an optical wavelength and is practically applicable for every problem in nonlinear optics [61]. It should also be noted that the complex conjugate terms are neglected without violating the equality of the nonlinear wave equation. The amplitude of the generated second harmonic is obtained by integration over the entire crystal length L [27], resulting in

$$A_2(L) = i\frac{\omega_2 d_{\text{eff}}}{n_2 c} A_1^2 \int_0^L e^{i\Delta kz}\,\mathrm{d}z = i\frac{\omega_2 d_{\text{eff}}}{n_2 c} A_1^2 \left(\frac{e^{i\Delta kL} - 1}{i\Delta k}\right). \tag{23}$$

Substituting the amplitude with

$$I = 2n\varepsilon_0 c|A|^2 \tag{24}$$

provides the intensity of the generated emission [61]. In this example the intensity is expressed by

$$I_2 = \frac{2\pi^2 d_{\text{eff}}^2}{n_2 n_1^2 \lambda_2^2 \varepsilon_0 c} I_1^2 L^2\, sinc^2\left(\frac{\Delta kL}{2}\right). \tag{25}$$

It becomes obvious that the generated intensity highly depends on the crystal length, the applied nonlinear coefficient, and the fundamental intensity I_1. Therefore, long crystals with high nonlinearity and lasers with increased output power and good spatial quality, such as DBR-tapered diode lasers, are preferred for efficient, high-power nonlinear interactions.

The most important parameter towards efficient frequency conversion is the wave vector mismatch. Figure 15 shows, that the intensity of a generated wave reaches a maximum at $\Delta k = 0$ and decreases significantly at $\Delta k \neq 0$. For example a mismatch of $\Delta k = 2.5$ reduces the intensity to less than 60% compared to the optimum. The scenario of $\Delta k = 0$ is referred to as phase-matching and methods to obtain phase-matching are discussed in section 0.

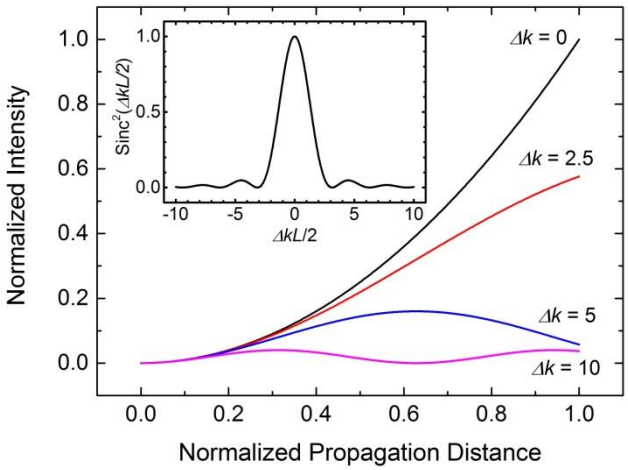

Figure 15: Sinc function in dependence of a wave vector mismatch (Inset) and its effect on the generated intensity. A mismatch of Δk = 2.5, 5, and 10 reduces the intensity to 58%, 5.7%, and 3.7% of the maximum intensity, respectively.

3.1.4. Pump depletion

The efficiency of nonlinear interactions is determined by the ratio of the generated to the fundamental intensity. According to the example above, phase-matching would enable the efficiency to exceed unity at high fundamental intensities and long crystal lengths, violating the principle of conservation of energy. Depletion of the fundamental intensity as a result of nonlinear interactions prevents that scenario. In case of pump depleted SHG the nonlinear efficiency η is given by [61]

$$\eta = \frac{I_2}{I_1} = tanh^2\left(\frac{L}{L_{\mathrm{NL}}}\right), \tag{26}$$

with

$$L_{\mathrm{NL}} = \frac{1}{4\pi d_{\mathrm{eff}}}\sqrt{\frac{2n_2 n_1^2 \lambda_1^2 \varepsilon_0 c}{I_1(0)}}. \tag{27}$$

Figure 16 shows that all incident radiation is converted into the second harmonic at $L/L_{\mathrm{NL}} \rightarrow \infty$, preventing the case of $\eta > 1$. It can also be seen that the undepleted pump approximation is valid up to $\eta \approx 10\%$.

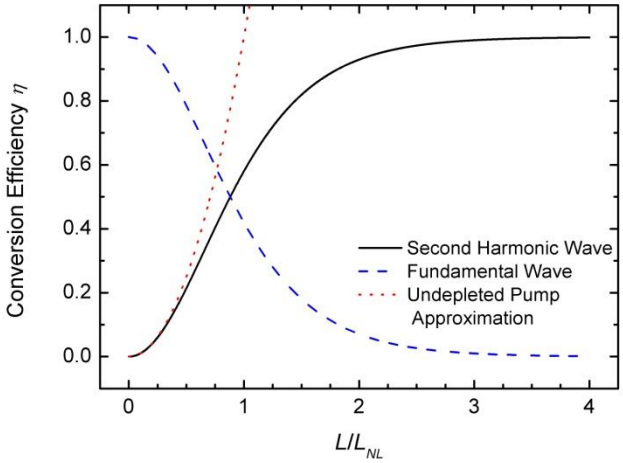

Figure 16: Conversion efficiency of phase-matched SHG in case of pump depletion and undepleted pump approximation assuming $I_2(0) = 0$.

3.2. Phase-matching

Efficient frequency conversion requires phase-matching between the interacting waves. Only then will the coherent fields generated within the crystal add constructively. With the wave vector at specific wavelengths defined by the refractive index [27]

$$k = \frac{2\pi n}{\lambda} = \frac{\omega n}{c}, \tag{28}$$

phase-matching ($\Delta k = 0$) requires the fundamental and generated waves to propagate at the same phase velocity. This is prevented by normal dispersion, resulting in longer wavelengths propagating faster than shorter ones. A solution to this challenge is birefringent phase-matching [62],[63].

3.2.1. Birefringent phase-matching

Birefringence describes the phenomenon of polarization dependent refractive indices in anisotropic crystals. Such crystals are characterized by direction dependent properties. Figure 17 illustrates how birefringence in such crystals can be utilized to obtain phase-matching. An electromagnetic wave polarized in the plane of the optic axis of a birefringent material and the propagation vector of the wave experiences the extraordinary refractive index n_e. Light polarized perpendicular to that plane experiences the ordinary refractive index n_o. In case of LN crystals ($n_e < n_o$), an extraordinary beam travels faster than an ordinary beam. This can be applied to compensate normal dispersion by choosing a nonlinear interaction involving ordinary polarized fundamental waves generating extraordinary polarized second

harmonic waves. For example, in case of LN crystals a corresponding interaction between orthogonal polarized waves could be based on the nonlinear coefficient d_{31} (d_{31} = 4.4 pm/V at 1064 nm, [64]). Methods to obtain birefringent phase-matching are temperature and angle tuning. In case of temperature tuning, the desired wavelengths are phase-matched by properly adjusting the crystal temperature, which affects the refractive indices to a different extent. However, this can potentially result in high temperatures and may limit practical applications of such interactions.

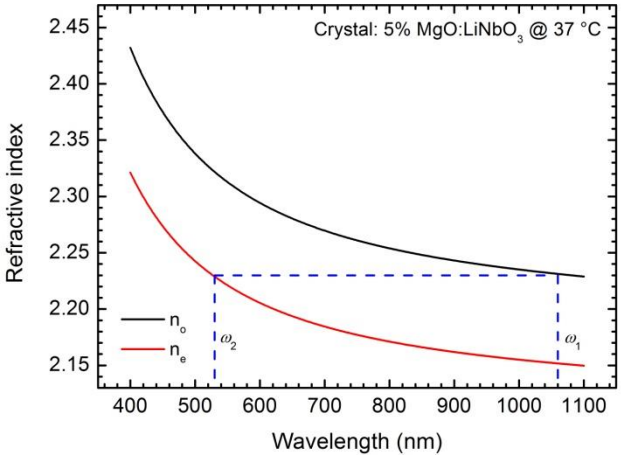

Figure 17: Ordinary and extraordinary refractive indices of 5% magnesium oxide doped LN (MgO:$LiNbO_3$), as applied in this work, at a crystal temperature of 37 °C. The calculations are based on temperature and wavelength dependent Sellmeier equations provided in [65].

In comparison to temperature tuning, angle tuning potentially enables phase-matching at lower temperatures. In this case, phase-matching is achieved by changing the orientation of the crystal's optic axis by an angle θ with respect to the propagation direction of extraordinary beams. This changes the experienced extraordinary refractive index according to [27]

$$\frac{1}{n_{\mathrm{e}}^2} = \frac{\sin^2(\theta)}{\bar{n}_{\mathrm{e}}^2} + \frac{\cos^2(\theta)}{n_{\mathrm{o}}^2}. \tag{29}$$

It can be seen that the extraordinary refractive index equals its principle value $\bar{n}_{\mathrm{e}}$ at $\theta = 90°$ and n_{o} at $\theta = 0°$.

A disadvantage of angle-tuning is the potential walk-off effect [60]. Obtaining phase-matching may require the beams not to propagate along a crystal axis ($0° < \theta < 90°$). This situation is referred to as critical phase-matching. In that case ordinary and extraordinary beams begin to diverge from each other by an angle ρ, according to

$$\tan(\rho) = \frac{\tan(\theta)\left(\frac{n_o^2}{n_e^2} - 1\right)}{1 + \frac{n_o^2}{n_e^2}\tan^2(\theta)}. \tag{30}$$

For example, birefringent phase-matching of 1062.4 nm wavelengths in LN crystals at 37 °C requires an angle of $\theta = 79.9°$ that results in a walk-off angle of $\rho = 0.8°$ for the extraordinary second harmonic emission. This walk-off reduces the spatial overlap with the fundamental beam and therefore the nonlinear conversion efficiency. In order to avoid the walk-off effect one has to choose noncritical phase-matching, which limits the accessible phase-matched wavelengths. Another solution is quasi phase-matching.

3.2.1. Quasi phase-matching

In addition to the walk-off effect a general drawback of birefringent phase-matching is the requirement of birefringent materials, limiting the number of nonlinear crystals providing phase-matching at the desired wavelengths. Furthermore, it does not enable nonlinear interactions involving the nonlinear coefficient d_{33}, which is the highest in crystals commonly used to generate green light [60]. For example, LN crystals are characterized by a nonlinear coefficient of d_{33} = 25 pm/V at 1064 nm [64]. This is a factor of 6 larger compared to the coefficient d_{31}, given above in case of birefringent phase-matching.

A phase-matching technique giving access to that much larger nonlinear coefficient is quasi phase-matching (QPM) [66],[67]. It is based on nonlinear materials with periodic inversions of one crystal axis (Figure 18). This can be obtained by different methods. For example, periodically poled lithium niobate (PPLN) crystals were realized with techniques such as electric field poling [68], electron beam writing [69] or proton exchange [70].

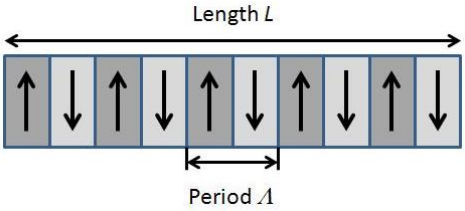

Figure 18: Illustration of a periodically poled material with a poling period Λ.

As discussed above, the intensity of a generated wave is obtained by integrating the amplitude over the entire crystal length, resulting in

$$I \propto \left(\int_0^L e^{i\Delta kz}\mathrm{d}z\right)^2 \tag{31}$$

Once phase-matching is obtained ($\Delta k = 0$) the intensity shows a quadratic dependence on the crystal length. Utilizing the nonlinear coefficient d_{33} requires the fundamental and second harmonic waves to be polarized in z-direction. This scenario does not allow compensation for normal dispersion, resulting in a wave vector mismatch ($\Delta k \neq 0$) and an oscillating behavior of the SHG intensity (Figure 19). The net output in this scenario becomes zero at $\Delta k = 2m\pi/L$, with m being an integer. On the other hand, maximum intensity is achieved at $\Delta k = (2m\text{-}1)\pi/L$. At this point the fundamental and generated waves experienced a phase shift of π. The corresponding length is referred to as coherence length L_c. By periodically inverting the sign of the nonlinear coefficient at that location an additional phase shift of π is introduced. Due to that phase shift, the generated field continues to grow in a stepwise manner (Figure 19). The corresponding poling period Λ is given by

$$\Lambda = 2mL_c, \tag{32}$$

with m representing the QPM order. In case of periodic poling with 50% duty cycle the QPM order is an odd number. Deviations of that duty cycle also enable even-order QPM [72].

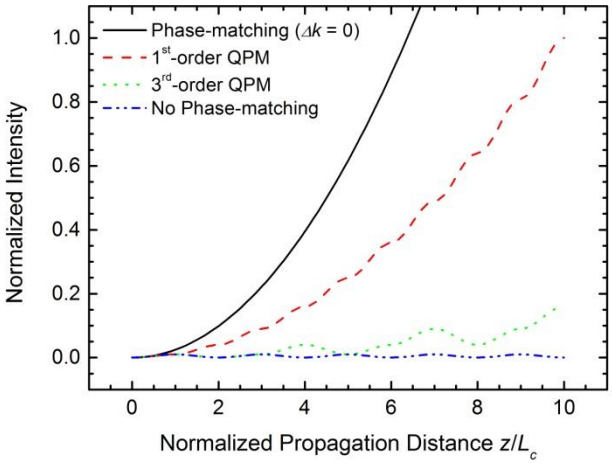

Figure 19: Normalized intensity versus propagation distance in case of phase-matching ($\Delta k = 0$), 1st and 3rd-order QPM and no phase-matching ($\Delta k \neq 0$).

In case of odd-order QPM the longitudinal dependence of the nonlinear coefficient can be written as [27]

$$d(z) = d_{\text{eff}} \operatorname{sign}\left[\cos\left(\frac{2\pi z}{\Lambda}\right)\right]. \tag{33}$$

Compared to birefringent phase-matching, QPM results in a reduced nonlinear coefficient according to

$$d_{\mathrm{QPM}} = \frac{2d_{\mathrm{eff}}}{m\pi}. \tag{34}$$

Therefore, first-order QPM has to be preferred in order to minimize this reduction. The corresponding wave vector mismatch is given by

$$\Delta k_{\mathrm{QPM}} = 2k_1 - k_2 + \frac{2\pi}{\Lambda}, \tag{35}$$

and results in an optimum period of

$$\Lambda = \frac{2\pi}{k_2 - 2k_1}. \tag{36}$$

As an example, the optimum period for first-order, noncritical quasi phase-matched SHG of 1062.4 nm lasers at 37 °C in 5% MgO:$LiNbO_3$ crystals is around 6.92 µm. Such short periods represent the major challenge in realizing such crystals. However, proper periodic poling enables noncritical quasi phase matching at any temperature and desired wavelengths within the transparency range of the crystal.

3.2.2. Phase-matching tolerances

With the phase-matching requirement expressed in equation (35) and the intensity proportional to a sinc-function,

$$I \propto sinc^2\left(\frac{\Delta k_{\mathrm{QPM}} L}{2}\right), \tag{37}$$

the wavelength, temperature and poling period tolerances can be estimated. Figure 20 and Figure 21 show the wavelength and temperature tuning curves for a 30 mm long, 5% MgO:$LiNbO_3$ crystal with a poling period of 6.92 µm.

The simulation results in a spectral acceptance bandwidth of $\Delta\lambda_{\mathrm{FWHM}}$ = 69 pm and a temperature acceptance of ΔT_{FWHM} = 0.8 °C. At 95% of maximum intensity the tolerances are significantly reduced to $\Delta\lambda_{95\%}$ = 19 pm and $\Delta T_{95\%}$ = 0.2 °C, respectively. Corresponding nonlinear interactions consequently require a precise control of crystal temperatures and lasers with narrow spectral emission, such as DBR-tapered diode lasers.

Regarding the tolerance for the poling period, Figure 22 indicates acceptance bandwidths of $\Delta\Lambda_{\mathrm{FWHM}}$ = 1.4 nm and $\Delta\Lambda_{95\%}$ = 0.4 nm at the above conditions. The required precision indicates the potential difficulty in production of these devices, desired to operate at specific conditions. For example, a poling period slightly increased by 0.1 µm shifts the phase-matching wavelength at 37 °C by a few nanometers. A compensation by crystal temperature results in a large shift of several tens of degree Celsius.

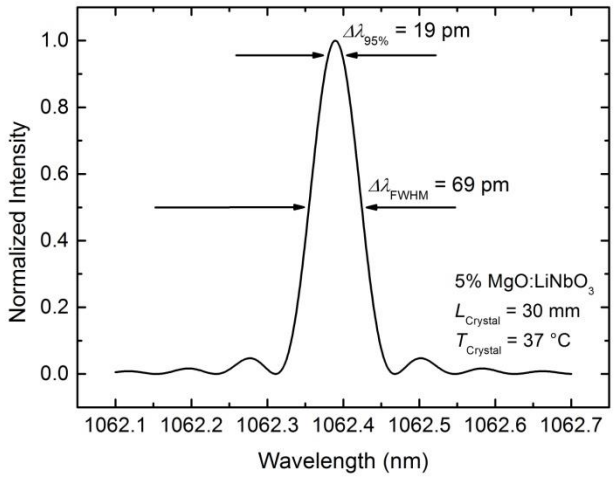

Figure 20: Simulated wavelength tolerance for QPM with a 30 mm long PPLN crystal. The calculations are based on temperature and wavelength dependent extraordinary refractive indices according to Sellmeier equations [65], and a thermal expansion coefficient of $\alpha = 1.59 \cdot 10^{-5}$/K [71].

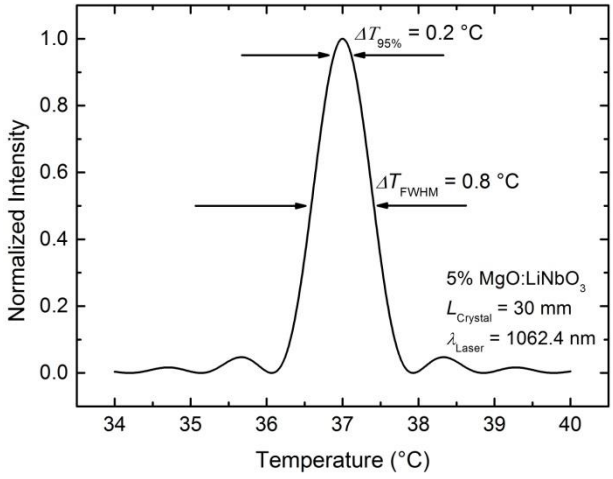

Figure 21: Simulated temperature tolerance for QPM with a 30 mm long PPLN crystal.

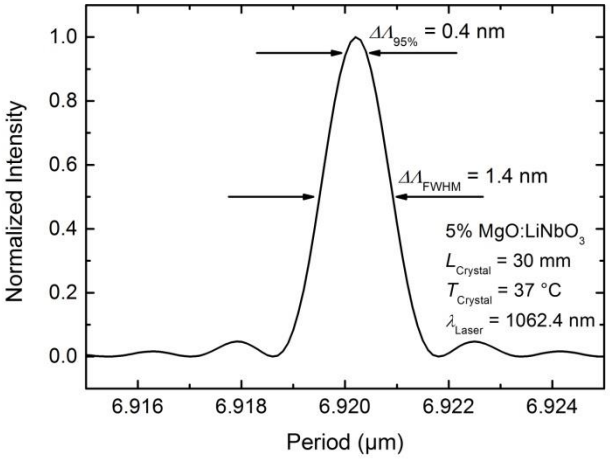

Figure 22: Simulated poling period tolerance for QPM in a 30 mm long PPLN crystal.

The acceptance bandwidths are also obtained using the following relations [72]:

$$\Delta\lambda_{\mathrm{FWHM}} = \frac{0.4429 \times \lambda_1}{L}\left|\frac{n_2 - n_1}{\lambda_1} + \frac{\partial n_1}{\partial \lambda} - \frac{1}{2}\frac{\partial n_2}{\partial \lambda}\right|^{-1} \tag{38}$$

$$\Delta T_{\mathrm{FWHM}} = \frac{0.4429 \times \lambda_1}{L}\left|\frac{\partial (n_2 - n_1)}{\partial T} - \alpha(n_2 - n_1)\right|^{-1} \tag{39}$$

$$\Delta\Lambda_{\mathrm{FWHM}} = \frac{3.55 \times L_{\mathrm{c}}^2}{L}. \tag{40}$$

All equations indicate that longer crystals preferred for efficient nonlinear interactions simultaneously narrow the acceptance bandwidths and a trade-off has to be made.

In the above scenarios it is assumed that the propagation of the fundamental waves is perpendicular to the periodic domain inversions. In practice, deviations by an angle θ shift the phase-matching wavelength λ according to

$$\Delta\lambda = \frac{\lambda^2 n_1}{2\Lambda n_2}\sin\theta. \tag{41}$$

Figure 23 shows the resulting wavelength shift $\Delta\lambda$ as a function of the angle of incidence with respect to the surface normal.

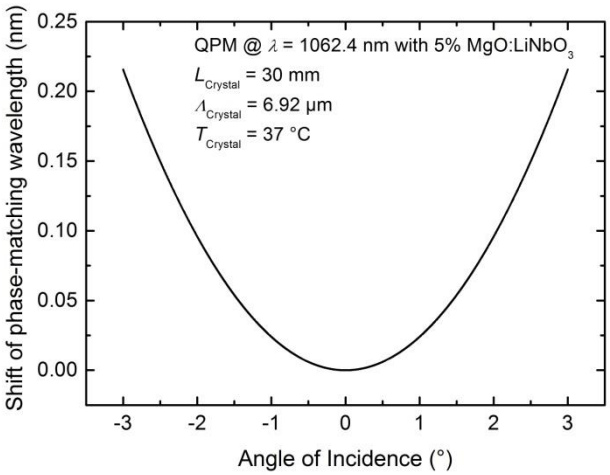

Figure 23: Simulated shift of the phase-matching wavelength for fundamental waves incident at an angle with respect to the surface normal of a 30 mm long PPLN nonlinear crystal.

It can be seen that angular deviations of 3° on a PPLN crystal with the provided parameters shift the phase-matching wavelength by roughly 0.2 nm. In case of diode lasers with tunable emission wavelengths such shifts are less critical. Applying the resulting wavelength shifts in the calculation of the wave vector mismatch provides the angular tolerance at fixed experimental conditions. In this example, Figure 24 reveals acceptance bandwidths of $\Delta\theta_{\mathrm{FWHM}} = 2.39°$ and $\Delta\theta_{95\%} = 1.25°$, respectively. The corresponding wavelength shifts match the spectral acceptance given above.

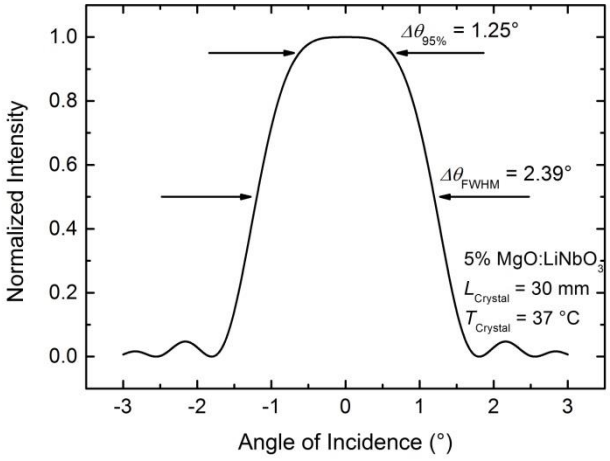

Figure 24: Considering phase-matching wavelength shifts for fundamental waves incident at an angle for the calculation of the wave vector mismatch provides the angular tolerances.

3.3. Boyd Kleinman analysis for frequency conversion

The intensity of generated beams scales with the fundamental intensity and the length of the nonlinear crystal. At fixed power settings, high intensities are obtained by focusing the fundamental beam into the nonlinear crystal. In nonlinear interactions the divergence of a focused beam limits the interaction length within the nonlinear crystal at tight confinements. Therefore, optimum focusing has to be selected with respect to the crystal length. In order to decouple these two parameters nonlinear waveguides can be used. However, it has been shown that the use of waveguides can be limited to low fundamental power [73]. Another solution is to optimize the focusing with respect to the crystal length, as described by Boyd and Kleinman [74]. In case of SHG in a lossless material, the generated output power P_2 is given by [60]

$$P_2 = \frac{16\pi^2 d_{\text{eff}}^2}{\varepsilon_0 c_0 \lambda_1^3 n_1 n_2} P_1^2 L h(\sigma, \beta, \kappa, \xi, \mu). \tag{42}$$

Here $h(\sigma,\beta,\kappa,\xi,\mu)$ represents the Boyd-Kleinman function with σ accounting for a phase mismatch, β accounting for the walk-off effect, κ accounting for absorption, ξ accounting for the strength of focusing and μ accounting for the focal position. Assuming noncritical phase-matching in a lossless material with the focus positioned in the center of the crystal (β = 0, κ = 0, μ = 0) simplifies the Boyd-Kleinman function to

$$h(\sigma, \xi) = \frac{1}{4\xi} \int \int_{-\xi}^{\xi} \frac{e^{i\sigma(\tau-\tau')}}{(1+i\tau)(1-i\tau')} \mathrm{d}\tau \mathrm{d}\tau', \tag{43}$$

with

$$\sigma = \frac{b\Delta k}{2} \tag{44}$$

and

$$\xi = \frac{L}{b}. \tag{45}$$

The maximum Boyd-Kleinman factor is obtained by optimizing Δk with respect to ξ, resulting in h = 1.07 at a confocal parameter of $b = L/2.84$. As an example, the optimum beam waist for phase-matched SHG of 1062.4 nm lasers in a 30 mm long LN crystal at 37 °C is around 28 µm (Figure 25). It should be noted that according to Boyd-Kleinman theory the optimum results are obtained at $\Delta k > 0$, compensating for a phase shift experienced by focused beams [75].

In case of elliptic beams or critical birefringent phase-matching the Boyd-Kleinman analysis can be expanded taking elliptic focusing into consideration. Numerical studies have shown that loose focusing in critical directions, compensating the walk-off effect, and strong focusing in noncritical directions are recommended to increase

the efficiency in large walk-off crystals [76],[77],[78]. In addition, an increased optimum spot size with respect to Boyd-Kleinman analysis was experimentally demonstrated for non-diffraction limited lasers [79].

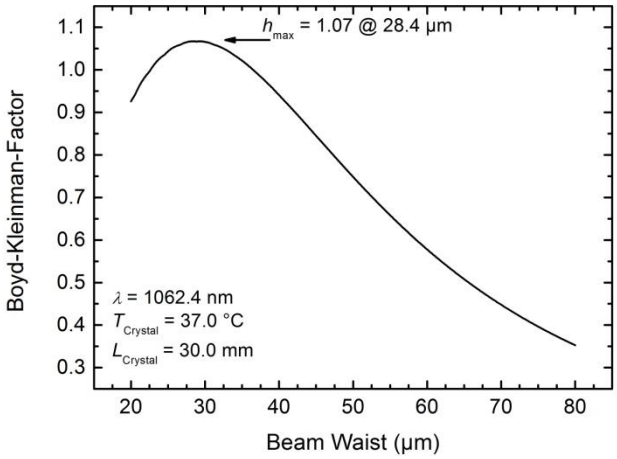

Figure 25: Boyd-Kleinman factor as a function of beam waist in case of SHG of 1062.4 nm wavelengths in a 30 mm long, 5% MgO:$LiNbO_3$ crystal at 37 °C.

3.4. Nonlinear materials for generation of green light

Different types of crystals can be applied for frequency conversion into the green spectral range. Two common crystals for birefringent phase-matched generation of visible laser emission are beta-barium borate (BBO) and lithium triborate (LBO). Due to their transparency, ranging from approximately 0.2 µm - 2.6 µm [80],[81], both crystals are preferably applied for frequency conversion into the UV spectral range. Applying these crystals for green light generation at room temperature requires critical phase-matching [92]. The maximum nonlinear coefficients at 1064 nm are d_{22} = 2.2 pm/V for BBO and d_{32} = 3.0 pm/V for LBO, respectively [82],[83]. Using a BBO crystal, up to 7 W (CW) of green light were generated with a vertical external cavity surface emitting laser in a resonant cavity configuration [84]. With a LBO crystal more than 130 W (CW) were obtained [85]. The absence of gray-tracking in LBO crystals, which is otherwise caused by light induced absorption that reduce the efficiency of pulsed and CW nonlinear interactions [86],[87], results in a good long-term stability and long lifetimes [92]. This was demonstrated by stable operation over more than 100 h at power levels > 100 W [85].

In comparison to birefringent phase-matching, QPM gives access to the larger nonlinear coefficient d_{33} of corresponding periodically poled crystals and allows for more efficient frequency conversion. Common poled crystals for green light

generation are potassium titanyl phosphate (KTP), lithium tantalate (LT) and lithium niobate (LN).

KTP crystals show a transparency range between 350 nm - 4500 nm and have a maximum nonlinear coefficient of d_{33} = 16.9 pm/V at 1064 nm [88],[89]. In addition, KTP is characterized by a high damage threshold, large acceptance bandwidths, a low coercive field value enabling large aperture poled crystals, and low photorefractive damage allowing for nonlinear interactions at room temperature [90],[91],[92]. One disadvantage of KTP crystals is gray tracking. Nevertheless, up to 6.2 W (CW) of green light were generated with 16% conversion efficiency by single-pass SHG of fiber lasers in 17 mm PPKTP crystals [93].

Of the three periodically poled crystals mentioned above LT has the lowest nonlinear coefficient (d_{33} = 13.8 pm/V at 1064 nm, [64]). Its transparency ranges from 280 nm - 5500 nm and the coercive field with up to 4.5 kV/mm is twice as high compared to KTP crystals [94]. Due to increased thermal conductivity and a high damage threshold, LT is very interesting for high-power applications [92]. Up to 18.3 W (CW) with 20.8% conversion efficiency were obtained by single-pass SHG of fiber lasers in 40 mm PPLT crystals [95].

Compared to the other nonlinear crystals above, LN has the highest nonlinear coefficient (d_{33} = 25 pm/V at 1064 nm, [64]) and is the crystal of choice in this work. It shows a transparency range between 400 nm - 5500 nm and the coercive field is comparable to that of LT crystals [96],[97]. Major disadvantages of LN crystals are the low damage threshold and low photorefractive damage threshold [98]. The latter causes an optically induced change of the refractive index that affects the phase-matching condition and leads to beam distortion preventing high-power nonlinear interactions [99]. This effect can be sufficiently reduced either by elevated crystal temperatures [98] or by adding > 4.5% magnesium oxide to the melt that increases the photoconductivity by 2 orders of magnitude [100]. Based on such magnesium doped crystals up to 3 W of green light (CW) were generated with 34% conversion efficiency by single-pass SHG of fiber lasers [101]. Using diode lasers more that 1.8 W with 23% conversion efficiency were demonstrated [102]. Beam combining with subsequent SFG of these lasers, as introduced in this work, resulted in up to 3.9 W and nearly 25% conversion efficiency [103]. Based on their performance and with respect to the above characterized DBR-tapered diode lasers, PPLN crystals are the preferred choice for efficient concepts of frequency conversion developed and applied in this work.

3.5. Basic setups for frequency conversion

Regarding experimental setups, the most straight-forward approach for nonlinear frequency conversion is the above mentioned single-pass configuration (Figure 26). The laser emission is directly focused into a nonlinear crystal. Optical isolation may be required in order to suppress undesired optical feedback that potentially harms

the pump laser. In that case, additional wave plates are used to adjust the fundamental power as well as to readjust the polarization direction as required for optimum conversion. For further experiments, the fundamental and generated waves are typically separated from each other by a dichroic mirror.

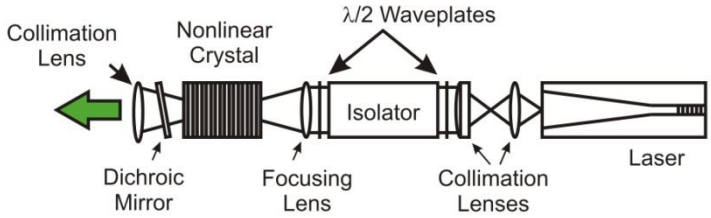

Figure 26: The example depicts the basic configuration applied in this work. The illustration shows single-pass frequency conversion of a collimated diode laser in a periodically poled nonlinear crystal.

A single-pass configuration can be realized with bulk or nonlinear waveguide crystals. With bulk material, conversion efficiencies up to 42% were demonstrated [104]. Tight confinement in nonlinear waveguides can be utilized in order to obtain even higher conversion efficiencies [105]. However, the performance of waveguide crystals can be limited by thermal non-uniformities at high pump powers [73]. In such cases planar waveguides with one-dimensional confinement represent a suitable alternative [106].

The principle of single-pass configurations can also be applied in a more complex cascaded frequency conversion using multiple crystals. This technique increases the effective length of the nonlinear material and leads to increased conversion efficiencies without affecting the phase-matching tolerances [107].

The obtained efficiencies can also be increased by multiple passes through the nonlinear crystal. For example, more than 45% conversion efficiency was obtained in a quadruple-pass regime [108]. This concept can be expanded using resonant cavities (Figure 27). Such configurations increase the fundamental intensity inside the cavity but become increasingly complex. Nevertheless, up to 134 W (CW) of green light and 90% efficiency were reported with an external cavity approach [85]. With intra-cavity configurations more than 60 W (CW) and optical conversion efficiencies up to 40% (pump to green) were obtained [109],[110],[111]. In order to simplify external cavity configurations, nonlinear crystals with curved facets were applied to realize monolithic cavity enhanced frequency conversion [112].

Comparing all these examples, the single-pass configuration with its simple and robust design is the preferred choice in this work.

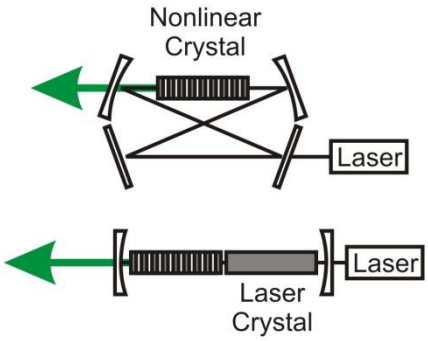

Figure 27: Principle setups for external cavity enhanced and intra-cavity frequency conversion. In external cavity configurations the nonlinear crystal is often positioned inside a bow tie resonator (top). Intra-cavity configurations are the basis for most frequency converted solid state lasers. Absorption of a fundamental laser generates new laser emission that is subsequently frequency converted (bottom). Additional components may be required to realize unidirectional ring cavities. Intra-cavity configurations also enable SFG utilizing the residual emission of the pump laser.

4. Power enhancement by spectral beam combining

The DBR-tapered diode lasers introduced in chapter 2 fulfill all requirements for efficient high-power green light generation, i.e., high output power, tunable laser emission with narrow spectral bandwidths, and good spatial emission properties with high percentages of power contained in the central-lobe. Applying them in a single-pass configuration resulted in 1.58 W of green light at wall-plug efficiencies of 5% [32]. At this level, green diode laser systems enable competitive direct optical pumping of Ti:sapphire lasers for OCT measurements, see below. Obtaining higher output powers with a single emitter for direct pumping or biomedical applications such as photocoagulation of vascular diseases [36],[37],[38] is rather challenging. According to equation (42), the generated output power scales with the square of the fundamental pump power. At maximum injection currents of 16 A SHG of these DBR-tapered diode lasers provides up to 2 W of green light (Figure 28). At higher injection currents the laser performance may suffer from heat generated inside the lasers, reducing the lifetime of devices and potentially leading to COMD.

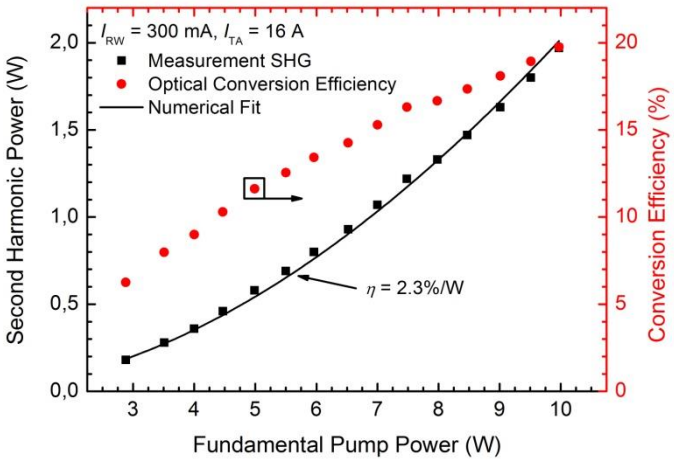

Figure 28: Second harmonic power and conversion efficiency versus fundamental pump power of a DBR-tapered diode laser at a maximum current of I_{TA} = 16 A. Frequency conversion is carried out in a 30 mm long, 5% MgO-doped PPLN crystal. The numerical fit is based on the depleted pump approximation, see section 5.3.

The question remains, how the output power of diode laser systems can efficiently be increased for nonlinear interactions without risking laser failure. A solution to this challenge is increasing the number of lasers in conjunction with beam combining [113]. It describes the scenario of two or more lasers being combined with external optical components. Thus, beam combining represents a means to efficiently increase the brightness of laser systems for subsequent nonlinear frequency conversion. This chapter summarizes the results obtained with volume Bragg grating based spectral beam combining of DBR-tapered diode lasers [114].

4.1. Beam combining of comparable lasers

Beam combining of comparable lasers can be carried out in a coherent or incoherent manner [113],[115]. In all cases power scaling is obtained by increasing the number of single emitters. Coherent beam combining requires spectral single-mode emission and phase stabilization. This implies precise control of wavelengths and phase relations of all emitters, so the individual fields add constructively. Therefore, coherent beam combining becomes increasingly complex the more elements that have to be combined. Nevertheless, output powers in the kW range with combining efficiencies > 78% were obtained with fiber laser arrays [116],[117],[118]. The term combining efficiency refers to the power ratio of the combined beam to the sum of fundamental power. Combining diode lasers, 12.8 W were obtained with a 47 emitter array [119].

In case of incoherent beam combining reduced requirements allow for much simpler setups [115]. The most straightforward technique for incoherent combining of two comparable lasers is polarization coupling [120]. With this technique orthogonally polarized lasers are combined with components such as polarizing beam splitters. However, the orthogonal polarizations may limit the efficiency of potential subsequent sum-frequency generation of the combined beams, see chapter 5.

Another technique is spectral beam combining (SBC), which describes incoherent combining of two or more lasers with shifted emission wavelengths [113],[115]. Using a diffraction grating a combined power in the kW range and a combining efficiency of 99% were demonstrated [121],[122].

However, diffraction gratings may limit incoherent combining of comparable diode lasers. For example, the applied 1062 nm DBR-tapered diode lasers are wavelength tunable with 0.08 nm/K (Figure 8). The wavelength difference between individual lasers in the above examples was > 5 nm. Obtaining such large wavelength separations with comparable diode lasers would require increased laser temperatures that may cause serious reductions in performance. According to the grating equation

$$\sin\theta = m\frac{\lambda}{\Lambda} \tag{46}$$

combining of comparable wavelengths requires similar angles of incidence, i.e., impractical large source-to-grating distances in order to spatially separate individual emitters [123]. In the equation θ represents the diffraction angle, m the diffraction order, λ the incident wavelength and Λ the grating period.

A solution to this limitation is the use of diode laser arrays described by the following relation

$$d \approx f\frac{1}{a\,cos(\alpha_0)}\Delta\lambda. \tag{47}$$

Here d is the spatial extent of the outer emitters, f the focal length of the lens between the array and the grating, a the grating period, α_0 the angle of incidence for

the central emitter, and $\Delta\lambda$ the wavelength spread of the array [124]. Combining a tapered diode laser bar, 9.3 W were obtained with a combining efficiency of 63% [125]. Major disadvantages in such setups are mounting induced smiles that negatively affect the spatial quality of the combined beam [126] and the loss in flexibility regarding an optimization of fundamental wavelengths for subsequent nonlinear interactions.

The method of choice in this work is spectral beam combining of diode lasers with volume Bragg gratings [127]. These gratings are written in photo-thermo-refractive (PTR) glass. The permanent change in refractive index is caused by UV radiation exposure followed by thermal development at temperatures around 520 °C [128]. PTR glass is virtually transparent within a spectral range of 350 nm - 2700 nm and provides excellent thermo-mechanical properties [129]. The latter includes a thermal stability up to 400 °C, a thermal expansion coefficient of $8.5 \cdot 10^{-6}$ K^{-1}, a temperature independent refractive index ($dn/dT = 5 \cdot 10^{-7}$ K^{-1}), a thermal conductivity of 0.01 W/cm, and a tolerance to CW radiation up to several tens of kilowatts per square centimeter. Thus, volume Bragg gratings (VBGs) are ideally suited for high-power laser applications. For example, up to 770 W were achieved by combining 5 fiber lasers with a combining efficiency of 91.7% [129]. The applied grating enabled wavelength shifts of 0.5 nm between individual lasers. Such short shifts are easily obtained with tunable diode lasers as well, making VBGs the preferred choice for spectral beam combining of comparable diode lasers.

4.2. Spectral and angular acceptance

The principle behind VBGs is based on Kogelnik's theory of coupled waves developed in 1969 [130]. For an unslanted reflecting VBG, characterized by planes of constant refractive index parallel to the surface of the PTR glass, the diffraction efficiency (*DE*) is given by

$$DE = \frac{sin^2\sqrt{\xi^2 - S^2}}{\frac{\xi}{S} - cos^2\sqrt{\xi^2 - S^2}}, \tag{48}$$

with

$$S = \frac{d2\pi n\delta n}{\lambda_B^2 f} \tag{49}$$

and

$$\xi = \frac{d\pi f \Delta\lambda}{\lambda_B}. \tag{50}$$

In these equations d is the grating thickness, n the refractive index of the PTR glass, δn the refractive index modulation, λ_B the Bragg wavelength, f the spatial frequency ($f = 1/\Lambda$, with Λ being the grating period), and $\Delta\lambda$ the deviation from the Bragg

wavelength [131]. It becomes obvious that the *DE* of a VBG depends to a large extent on the incident laser emission wavelength with respect to the Bragg wavelength. As an example, Figure 29 shows the simulation of the spectral sensitivity based on the parameters summarized in Table 1.

Table 1: Parameters used to simulate the *DE* of a reflecting VBG. The parameters not provided by the supplier are replaced by values found in the literature for beam combining at comparable wavelengths.

Parameter	Symbol	Value
Bragg wavelength	λ_B	1062 nm
Thickness	d	3.41 mm
Refractive index	n	1.5 [132]
Refractive index modulation	δn	300 ppm [129]
Grating period	Λ	360 nm [133]

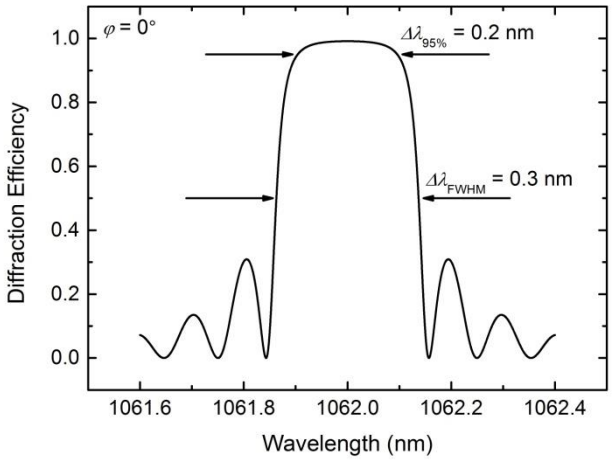

Figure 29: Simulation of the spectral sensitivity of an unslanted reflecting VBG (φ = 0°) specified for 1062 nm. The angle φ describes the angular deviation of the grating vector to the surface normal.

The plot in Figure 29 shows a typical characteristic for volume Bragg gratings. At the Bragg condition the *DE* is close to unity. At multiple points offset from the Bragg condition the *DE* is reduced to zero. The acceptance bandwidth in this example is $\Delta\lambda_{FWHM}$ = 0.3 nm. At 95% of maximum *DE* the acceptance bandwidth is slightly reduced ($\Delta\lambda_{95\%}$ = 0.2 nm). The resulting top-hat like profile is typical for reflecting VBGs. For comparison, transmitting VBGs are characterized by an increased sensitivity, resulting in a more defined wavelength selectivity and 33% lower efficiencies at incident emission with spectral widths equal to the acceptance bandwidth of the gratings [134].

Due to narrow acceptance bandwidths defined in the production process VBGs are highly attractive for beam combining of comparable diode lasers. For example, in case of a reflecting VBG one laser providing narrow spectral emission within the

acceptance bandwidth is wavelength tuned in order to fulfill the Bragg condition and to obtain diffraction. A second laser tuned to wavelengths that do not fulfill the Bragg condition is simply transmitted through the grating. SBC of these two beams is obtained by optimizing the overlap of the diffracted and transmitted emission.
In addition to the spectral sensitivity, the *DE* of VBGs also shows an angular dependence. In case of a reflecting VBG, the angular deviation from the Bragg angle $\Delta\theta$ is translated into a Bragg wavelength deviation using the following relation [134]

$$\Delta\theta = \sqrt{cot^2\,\theta_B + \frac{2\Delta\lambda}{\lambda_B}} - cot\,\theta_B. \tag{51}$$

Figure 30 shows the corresponding simulation of the angular sensitivity based on a Bragg angle of θ_B = 6.4° and grating parameters summarized in Table 1. With the specified grating the angular acceptance is as narrow as $\Delta\theta_{FWHM}$ = 0.13°. At 95% of maximum efficiency the angular acceptance is reduced to $\Delta\theta_{95\%}$ = 0.09°, which requires a precise adjustment of the angle of incidence at fixed emission wavelengths. Using diode lasers provides the advantage that beam combining can be optimized more easily, by actively adjusting the angle of incidence and the emission wavelength simultaneously.

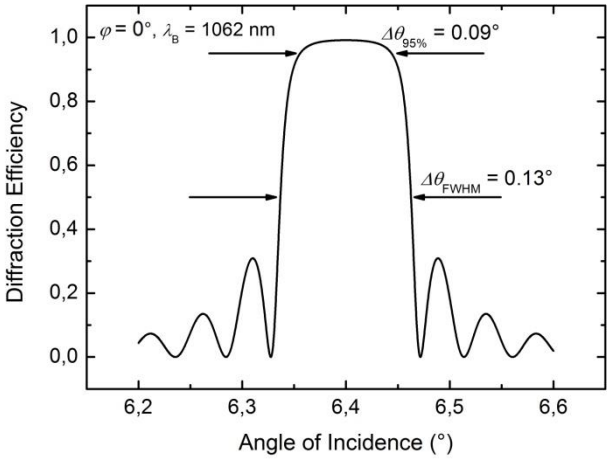

Figure 30: Simulation of the angular sensitivity of an unslanted reflecting VBG (φ = 0°). The grating is specified for 1062 nm and a Bragg angle of 6.4°. The applied parameters of the simulation are listed in Table 1.

4.3. Description of the experimental setup for beam combining

The applied setup for Bragg grating based SBC of comparable diode lasers is illustrated in Figure 31. It consists of two 1062 nm DBR-tapered diode lasers that are collimated and corrected for astigmatism using pairs of aspheric lenses

(f = 3.1 mm, NA = 0.68) and cylindrical lenses (f = 15 mm). All lenses are antireflection (AR)-coated in order to suppress optical feedback from back-reflections at the lens surfaces. The selected lenses result in a nearly circular emission with roughly 2 mm in diameter.

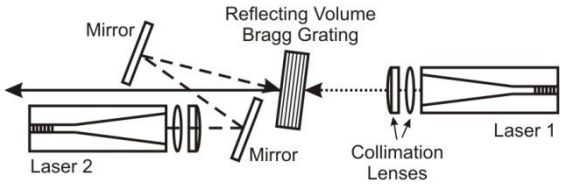

Figure 31: Setup for spectral beam combining of DBR-tapered diode lasers with a reflecting volume Bragg grating. The beam transmitted by the grating is indicated by dots. The diffracted beam fulfilling the Bragg condition is indicated by dashes.

Beam combining is carried out with a L x W x H = 3.4 mm x 10 mm x 10 mm reflecting VBG (*OptiGrate*). According to the supplier, the specified grating has an average *DE* of 99.2% at 1062 nm and a spectral selectivity of $\Delta\lambda_{FWHM}$ = 0.3 nm. The Bragg angles are 6.4° and -6.7°. Laser 1 not fulfilling the Bragg condition is transmitted by the grating. Beam combining with Laser 2 is achieved by properly adjusting its angle of incidence and wavelength, while monitoring the overlap at different positions. Once beam combining is obtained, the difference in emission wavelengths between the two lasers can easily be changed by temperature tuning of Laser 1 towards another minimum of the *DE* curve. However, a trade-off has to be made between wavelength separation and combining efficiency. At similar wavelengths both lasers will be diffracted equally preventing spectral beam combining.

4.4. Characterization of the applied diode lasers

Both lasers are operated at I_{RW} = 300 mA and T = 20 °C. Figure 32 shows the obtained output power versus the injection current to the tapered section. For Laser 1, a slope efficiency of 0.74 W/A is measured. The power of Laser 2 does increase with 0.71 W/A. At maximum currents the lasers emit 8.92 W (Laser 1) and 8.46 W (Laser 2), respectively, without showing signs of thermal roll over. The inset in Figure 32 shows the spectra at maximum currents. The center wavelengths of both lasers are located at 1063.0 nm (Laser 1) and 1062.9 nm (Laser 2), respectively. The spectra show a side-mode suppression ≥ 25 dB and spectral widths < 10 pm. The latter is well within the spectral acceptance bandwidth of the specified grating. Therefore, both lasers show a comparable performance and are suited for spectral beam combining with the specified grating.

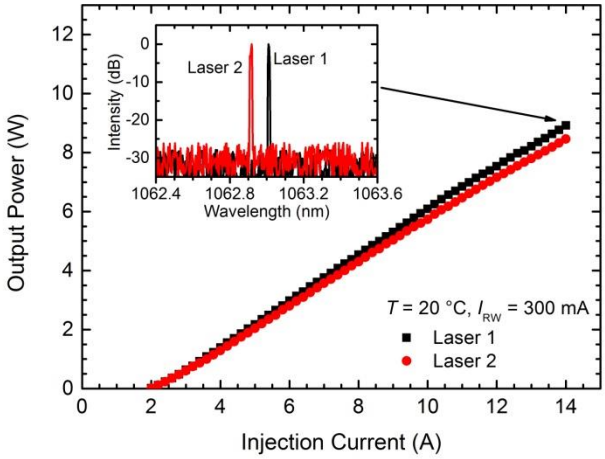

Figure 32: Power current characteristics and emission spectra of two DBR-tapered diode lasers at I_{RW} = 300 mA and T = 20 °C.

As mentioned above, spectral beam combining is obtained by adjusting the angles of incidence and emission wavelengths properly. Assuming a linear dependence between wavelengths and laser temperatures, a tunability of 0.09 nm/K is measured (Figure 33). Due to a VBG acceptance bandwidth of 0.3 nm, the required change in laser temperature for spectral beam combining of the two lasers is not critical.

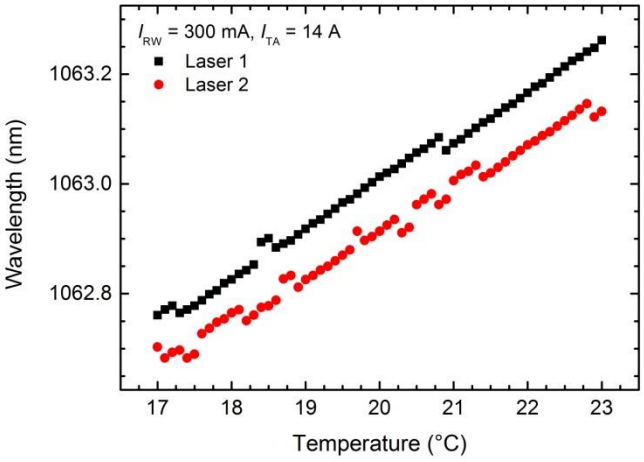

Figure 33: Wavelength versus laser temperature of two DBR-tapered diode lasers.

In addition to the power and spectral performance the spatial qualities of both lasers are measured according to the $1/e^2$ criteria (Figure 34). At maximum currents the M^2 values in the fast axis are 1.5 (Laser 1) and 1.4 (Laser 2). In the slow axis, values of 2.1 (Laser 1) and 3.2 (Laser 2) are obtained. In summary, both lasers are comparable in all aspects and are suitable for SBC with the specified grating.

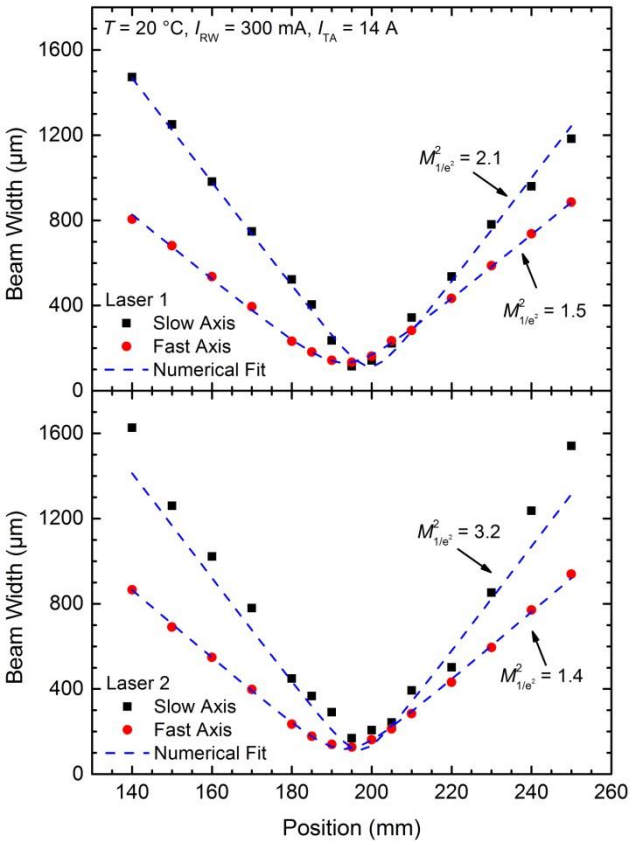

Figure 34: $1/e^2$ beam widths of two DBR-tapered diode lasers at T = 20 °C, I_{RW} = 300 mA, and I_{TA} = 14 A. The images show the measurements for Laser 1 (top) and Laser 2 (bottom), respectively.

4.5. Spectral beam combining of two DBR-tapered diode lasers

Spectral beam combining of two DBR-tapered diode lasers is carried out at different injection currents to the tapered sections (I_{TA} = 6 A, 8 A, 10 A, 12 A, 14 A). At each point both lasers are corrected for astigmatism, and the emission wavelengths and angles of incidence for Laser 2 are adjusted for maximum combining efficiency. At injection currents of 6 A, a combining efficiency of 95.4% is obtained and results in a combined power of 5.4 W (Figure 35). At 14 A to the tapered sections the output power increases up to 16.1 W. The corresponding combining and wall-plug efficiencies are 93.7% and 26%, respectively. The reduction in combining efficiency at higher currents can be explained by slight degradations of laser parameters. Additional losses within the setup are linked to finite divergences and potential grating non-uniformities [132].

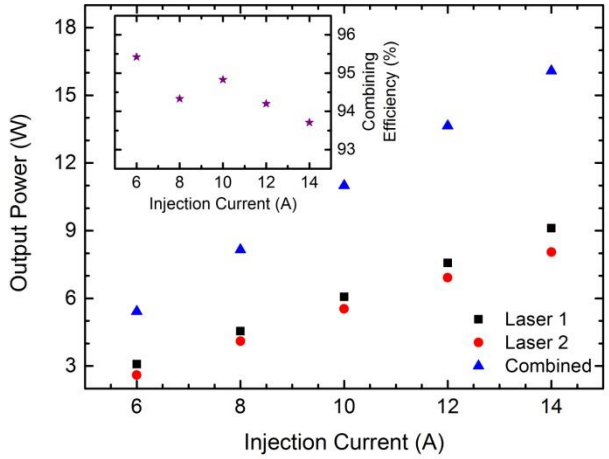

Figure 35: Output power of individual and beam combined DBR-tapered diode lasers at different injection currents. The inset shows the corresponding combining efficiencies.

At maximum currents, the laser temperatures are set to 15.5 °C (Laser 1) and 23.0 °C (Laser 2), respectively. The resulting emission wavelengths are located at 1062.7 nm and 1063.2 nm (Figure 36). In both cases the spectral widths and side-mode suppressions are not affected by SBC.

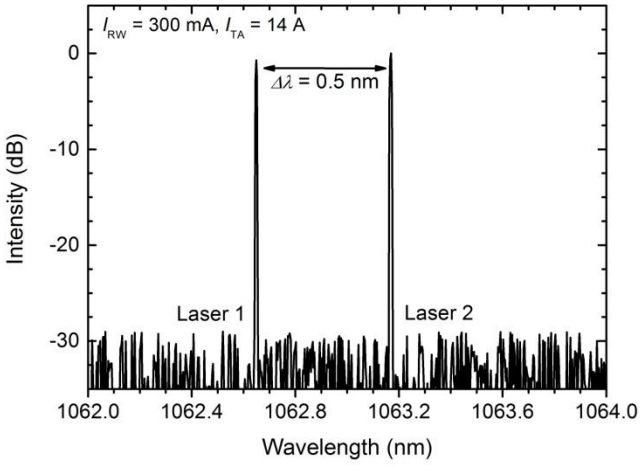

Figure 36: Emission spectrum of the combined beam showing a spectral separation of 0.5 nm between the individual lasers.

The spatial quality of the combined beam is comparable to the individual lasers (Figure 37). The M^2 values measured according to the $1/e^2$ criteria are $M^2 = 1.8$ (fast axis) and $M^2 = 3.3$ (slow axis), respectively. A similar behavior is observed at low injection currents (Table 2).

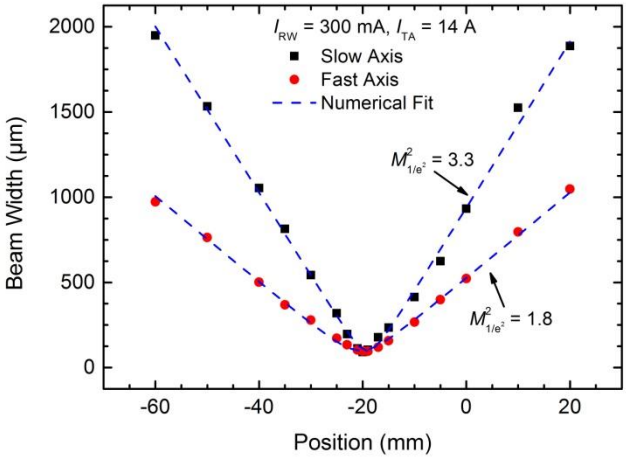

Figure 37: $1/e^2$ beam widths of the combined beam at I_{RW} = 300 mA, and I_{TA} = 14 A.

Table 2: Variation of M^2 values for Laser 1, Laser 2 and combined at low and high injection currents.

	I_{TA} = 6 A			I_{TA} = 14 A		
	Laser 1	Laser 2	Combined	Laser 1	Laser 2	Combined
$M^2_{\text{Slow Axis}}$	2.2	2.4	2.4	2.1	3.2	3.3
$M^2_{\text{Fast Axis}}$	1.5	1.4	1.6	1.5	1.4	1.8

These results clearly demonstrate the potential for efficient high-power diode laser systems based on SBC of comparable lasers. Utilizing the wavelength tunability of diode lasers enables less critical optical alignment compared to lasers limited to certain atomic transitions. Maintaining the spatial quality, spectral beam combining of diode lasers potentially leads to efficient, compact and low-cost systems with high-power, diffraction-limited emission. Subsequent nonlinear frequency conversion of combined lasers can benefit to a strong extent from this technique and enable diode laser systems generating multiple watts in the visible spectral range.

5. Sum-frequency generation of spectrally combined diode lasers

Spectral beam combining represents an efficient method to enhance the output power of laser systems that are otherwise limited by effects such as thermal degradation. In addition, the resulting overlap of two combined beams in the above example is an ideal condition for subsequent sum-frequency generation (Figure 14). This chapter summarizes the results achieved by SFG of beam combined DBR-tapered diode lasers [103].

5.1. Brief theoretical consideration

The coupled amplitude equation for the case of SFG is expressed by the following relation

$$\frac{dA_3}{dz} = i\frac{2\omega_3 d_{\text{eff}}}{n_3 c} A_1 A_2 e^{i\Delta kz}. \tag{52}$$

Here A_1 and A_2 represent the field amplitudes incident on the nonlinear crystal. From that equation the intensity of the generated emission can be derived [61]

$$I_3 = \frac{8\pi^2 d_{\text{eff}}^2}{n_3 n_2 n_1 \lambda_3^2 \varepsilon_0 c} I_1 I_2 L^2 \, sinc^2\left(\frac{\Delta kL}{2}\right). \tag{53}$$

A more detailed derivation is provided in [27]. A direct comparison with the case of SHG expressed in equation (25) shows that doubling the fundamental intensity using similar lasers (I_1, I_2) increases the amount of generated green light (I_3) by a factor of four. Therefore, SFG of comparable lasers can be applied to efficiently overcome performance limitations of single emitter based green diode laser systems.
For both nonlinear interactions the efficiency scales with the square of the nonlinear coefficient. As discussed above, efficient nonlinear frequency conversion into the green spectral range using lithium niobate crystals should preferably be based on the nonlinear coefficient d_{33} [60]. According to

$$P_z(\omega_1 + \omega_2) = 4\varepsilon_0 d_{33} E_z(\omega_1) E_z(\omega_2), \tag{54}$$

this requires the two lasers to be polarized in the same direction, which eliminates polarization coupling in favor of the above applied VBG based spectral beam combining.

5.2. Experimental setup for sum-frequency generation

In comparison to the setup for SBC applied in chapter 4, only minor changes are made (Figure 38). The concept consists of two collimated DBR-tapered diode lasers positioned at the same distance to the grating. Both lasers are corrected for astigmatism using the same pairs of aspheric and cylindrical lenses.

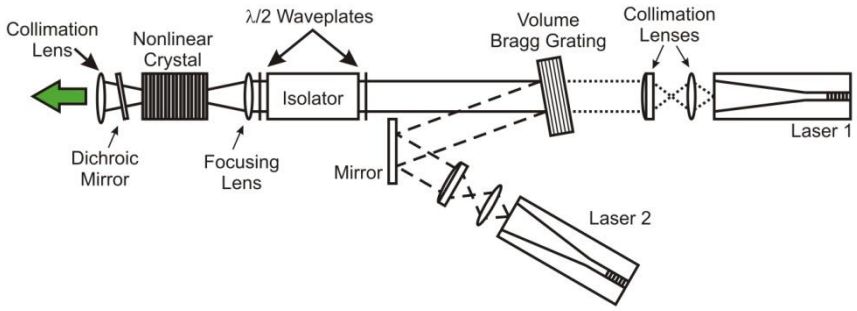

Figure 38: Experimental setup for spectral beam combining of DBR-tapered diode lasers with subsequent sum-frequency generation.

Beam combining is carried out with the same grating as specified in section 0 (*DE* > 99% at 1062 nm). In order to obtain high combining efficiencies both lasers are wavelength tuned while simultaneously adjusting the angle of incidence for Laser 2. As explained in section 0, the resulting wavelength separation between the two lasers is crucial and needs to be carefully observed. Similar emission wavelengths would to a certain extent be comparable to frequency conversion of multimode lasers, which led to increased conversion efficiencies in comparison to single-mode lasers [135],[136]. However, due to the characteristics of VBGs similar wavelengths will be diffracted equally preventing spectral beam combining.

Behind the grating a combination of two waveplates and a 30 dB optical isolator is used. The optical isolator suppresses unwanted back-reflections that otherwise can destabilize the diode laser [137]. This component consists of a Faraday rotator positioned in between two polarizers. In Figure 38 the waveplate to the right of the isolator adjusts the linearly polarized laser emission for transmission through the isolator. It therefore enables regulating the output power available for frequency conversion without changing the injection current. The Faraday rotator tilts the polarization according to the Faraday effect, which can be observed in certain materials placed in a static magnetic field [53]. The rotation depends on the propagation length, the magnetic flux, and the wavelength and material dependent Verdet constant. In this example the incident polarization is rotated by 45°. The obtained rotation does not reverse and therefore protects the lasers against potential back reflections. The second waveplate corrects the direction of polarization with respect to the requirements for efficient frequency conversion.

For efficient SFG an achromat (f = 75 mm) generates a 42 µm beam waist inside a plane cut, 5% MgO-PPLN crystal (*HCPhotonics*). This is slightly larger than predicted by Boyd-Kleinman theory for focused Gaussian beams but proved to be optimum in the experiments. The deviation may be explained by the reduced spatial quality of the lasers with respect to an ideal Gaussian beam [79]. The dimensions of the crystal are L x W x H = 30 mm x 2 mm x 0.5 mm. The poling period of the AR-coated crystal is 6.92 µm.

In order to separate the second harmonic and fundamental laser emission a dichroic mirror is positioned behind the crystal. An optional lens collimates the generated green light for further experiments.

5.3. Frequency conversion of spectrally combined diode lasers

In the experiments both diode lasers are operated at different injection currents to the tapered sections (I_{TA} = 6 A, 8.5 A, 11 A, 13.5 A, 16 A). Because the overlap of the individual beams is of tremendous importance for frequency conversion, the beams are observed using two beam scanners simultaneously. Figure 39 shows the obtained overlap of the beam waist profiles at injection currents of 6 A. Figure 40 displays an image of the collimated, combined beam at a long distance. The figures show a good overlap of the two lasers, obtained by optimizing laser wavelengths and angles of incidence on the VBG. The intensity contained in the wings of the lateral beam waist profiles is also reproduced in the lower image.

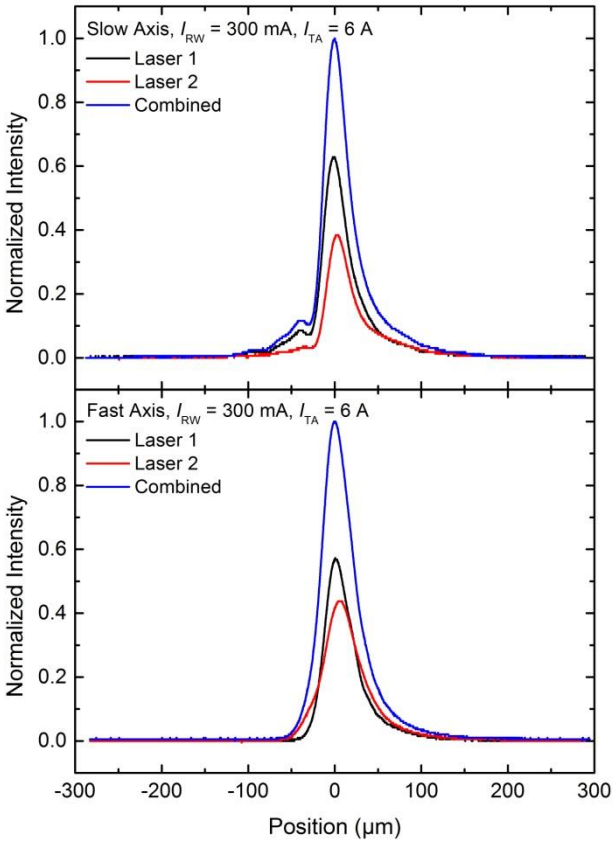

Figure 39: Beam waist profiles of two spectrally combined DBR-tapered diode lasers at injection currents of I_{TA} = 6 A. The profiles are measured along the slow axis (top) and fast axis (bottom).

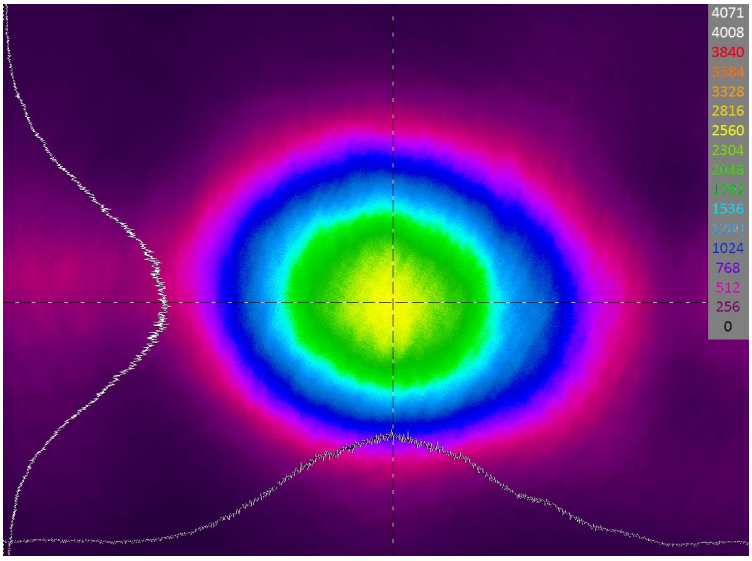

Figure 40: Image of the collimated beam of two spectrally combined DBR-tapered diode lasers at injection currents of I_{TA} = 6 A.

The results obtained with spectral beam combining are illustrated in Figure 41. At low currents (I_{TA} = 6 A) an output power of 5.1 W is obtained. The maximum output power at I_{TA} = 16 A is 18.0 W. The achieved combining efficiencies are within 90% - 92%, comparable to the results obtained above. The measured spatial qualities are $M^2_{4\sigma} \approx 2$ in the fast axis and $M^2_{4\sigma} \approx$ 4-5 in the slow axis, with reduced qualities at higher injection currents (Figure 42).

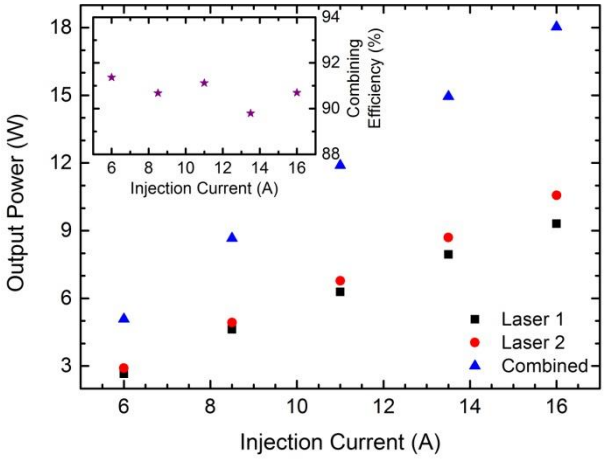

Figure 41: Output power of individual and beam combined DBR-tapered diode lasers at different injection currents. The inset shows the corresponding combining efficiencies.

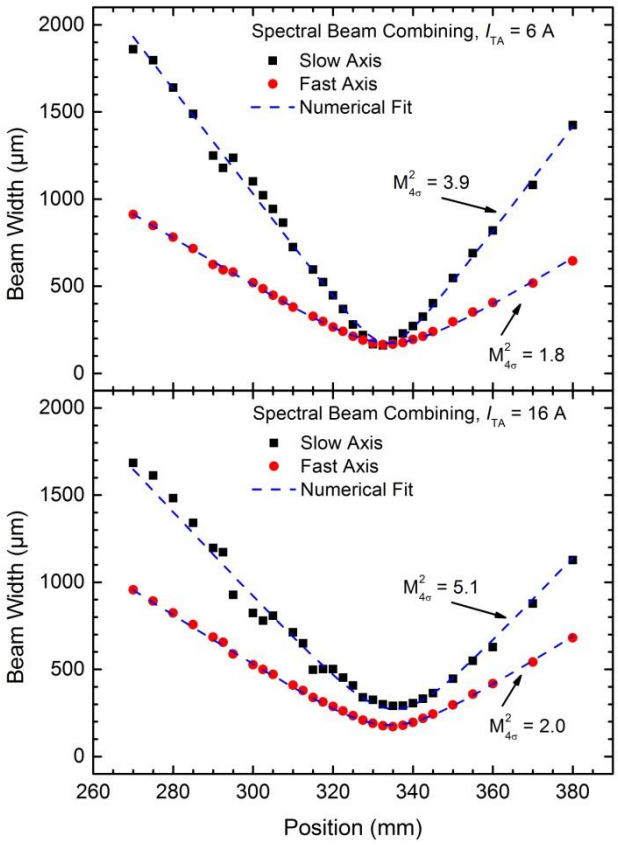

Figure 42: Beam widths measured along the beam waist of the combined beam at I_{TA} = 6 A (top) and I_{TA} = 16 A (bottom).

Two combined lasers enable three different nonlinear processes for green light generation that are individually selected by changing the crystal temperature. Figure 43 shows the temperature tuning curves measured at different wavelength separations between the two lasers. At closely spaced emission wavelengths the contributions by SHG and SFG are more difficult to be distinguished from another. By shifting the emission wavelength of Laser 1 towards longer wavelengths, the phase-matching temperatures for SHG of Laser 1 and SFG are increased. This results in an increased separation of the individual processes.

All interactions are characterized by a temperature acceptance around ΔT_{FWHM} = 1.4 °C. In addition, distinct side-lobes shifted by 1.5 °C from the corresponding phase-matching temperatures are observed. This behavior is potentially caused by poling non-uniformities along the crystal length. A rough estimation based on the equations (35) and (37) shows that this increase in phase-matching temperatures can already occur at poling period deviations of a few nanometers.

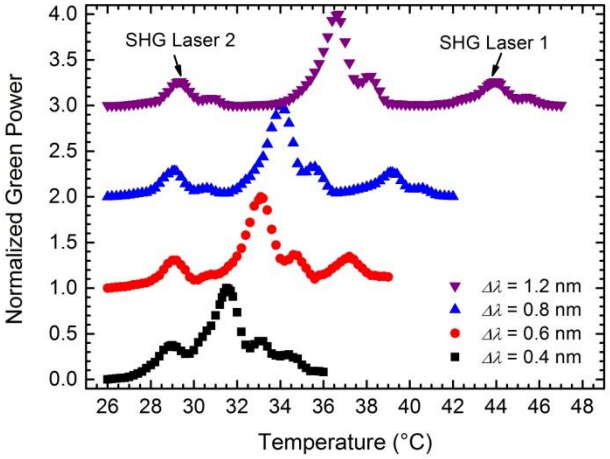

Figure 43: Output power of the generated green light versus crystal temperature at different wavelength separations between the combined lasers. The individual curves are shifted in vertical direction for better analysis.

Figure 44 shows the obtained output power at I_{TA} = 6 A for frequency doubling of Laser 1 and Laser 2, as well as the achieved amount of green light generated by SFG. In case of SHG, an available pump power of about 2.2 W results in 0.16 W of green light. This corresponds to conversion efficiencies of about 7% for each laser. The nonlinear efficiency under pump depletion is obtained with the following relation [32]

$$P_2 = P_1 tanh^2\left(\sqrt{\eta P_1}\right). \tag{55}$$

Here P_1 represent the fundamental pump power and P_2 the power obtained by SHG. The numerical fits show good agreement with the measured data and result in nonlinear efficiencies of η = 3.8 %/W for Laser 1 and η = 3.4%/W for Laser 2, respectively.

In case of SFG of the combined lasers 0.53 W at 3.2 %/W are measured. It should be noted that the nonlinear efficiency of SFG under depleted pump approximation is calculated slightly different by

$$P_3 = \frac{P_1 + P_2}{2} tanh^2\left(\sqrt{4\eta \frac{P_1 + P_2}{2}}\right). \tag{56}$$

Here P_1 and P_2 represent the fundamental pump powers and P_3 the power obtained by SFG. In comparison to the case of SHG, the depleted pump approximation is changed in order to express the above discussed increase by a factor of four with respect to SHG of a single laser.

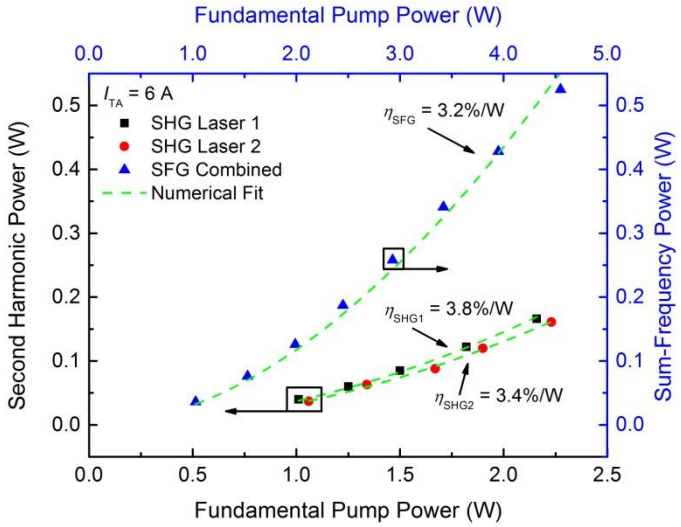

Figure 44: Second harmonic and sum-frequency power versus fundamental pump power at I_{TA} = 6 A. The case of SHG is plotted using the bottom-left scales. The top-right scales are used for SFG.

Comparing the output power obtained by SHG of a single laser and SFG of two combined lasers shows that the latter results in a 3.2-fold increase. The deviation to an ideal 4-fold improvement is mainly affected by the overlap of the two beams and fundamental pump depletion.

At maximum injection currents (I_{TA} = 16 A) an available pump power of 15.7 W generates an output power of 3.9 W by SFG (Figure 45). This corresponds to optical conversion and nonlinear efficiencies of 24.8% and 2.6 %/W, respectively. The wall-plug efficiency is 5.7%. Frequency doubling of the individual lasers results in an output power of 1.6 W at available pump powers of about 7.7 W. Based on the depleted pump approximation, nonlinear efficiencies of 3.0 %/W are calculated. The reduction of the improvement factor from 3.2 at 6 A to 2.5 at 16 A is to a high extent caused by reduced beam qualities in conjunction with a decreasing power content in the central lobe. While the values in the fast axis remain stable around 90%, the values in the slow axis drop from 81% at 6 A down to 73% at 16 A. This reduction makes it more difficult to obtain a proper overlap of the individual beams for efficient frequency conversion.

The inset in Figure 45 shows an emission spectrum obtained by sum-frequency generation at I_{TA} = 16 A. As shown above, tuning the pump wavelengths enables to separate phase-matching temperatures of individual nonlinear interactions. Therefore, single-mode emission can be obtained. The spectrum in Figure 45 shows a side-mode suppression > 15 dB and a spectral width of $\Delta\lambda_{FWHM}$ = 5 pm.

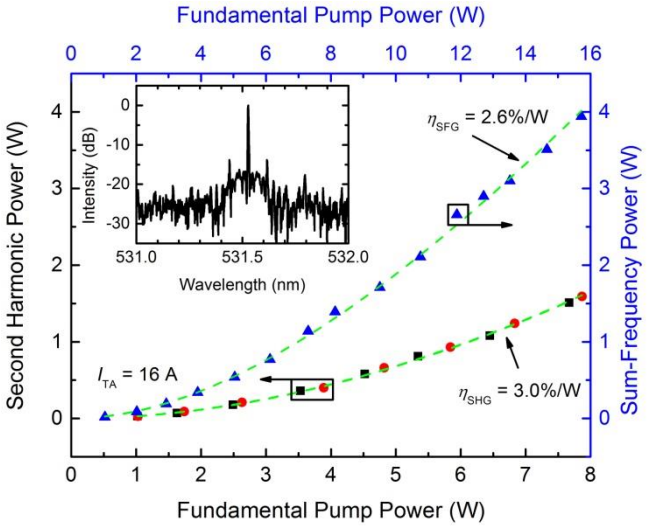

Figure 45: Second harmonic and sum-frequency power versus fundamental pump power at I_{TA} = 16 A. The inset shows an emission spectrum measured at maximum performance.

In order to analyze the power stability, the SFG output power at I_{TA} = 16 A is recorded over one hour (Figure 46). The plot shows a maximum deviation of 2.6%. The obtained stabilities can be significantly improved by implementing electronic feedback loops, see section 8.2.

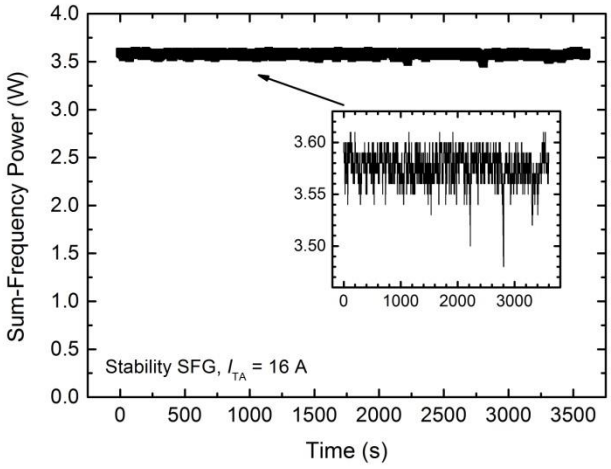

Figure 46: Output power of the sum-frequency generated beam measured over one hour at I_{TA} = 16 A. The inset shows an enlarged plot of the measured data.

The spatial properties of the generated green light reveal diffraction-limited emission with $M^2_{4\sigma}$ = 1.1 in the fast axis and $M^2_{4\sigma}$ = 1.3 in the slow axis, respectively

(Figure 47). The fact that very good spatial properties are obtained even at high pump power indicates the lack of photorefractive damage one might expect at high-power performance [99]. The improvement with respect to the fundamental emission can be explained by the central lobe contributing most efficiently to the green light generation as well as a spatial nonlinear beam clean-up, affected by the overlap of the involved beams [138].

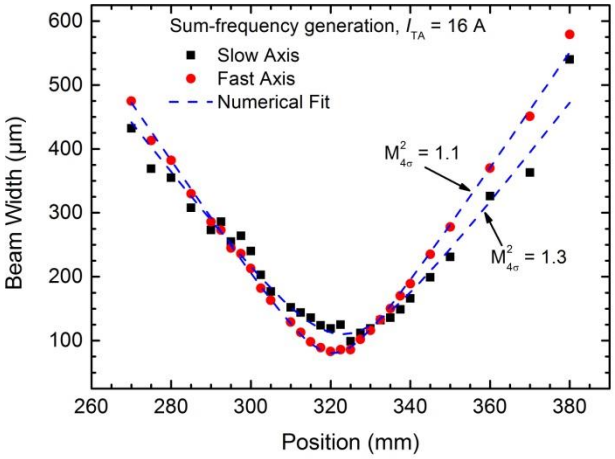

Figure 47: Beam widths of the sum-frequency generated beam measured along the beam waist at I_{TA} = 16 A.

In order to provide an overview on the performance at different injection currents, Figure 48 summarizes the corresponding output powers obtained by SHG and SFG. The inset shows the decreasing improvement factor, discussed above.

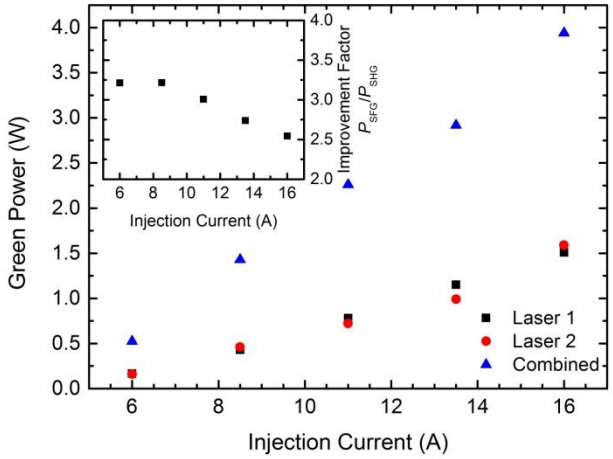

Figure 48: Output power in the green spectral range generated by SHG or SFG at various injection currents. The inset shows the improvement factor obtained for SFG with respect to SHG of a single laser.

The results show that the concept of SFG with spectrally combined diode lasers helps to efficiently enhance the output power of diffraction-limited visible diode laser systems. Based on their wavelength tunability these systems provide an additional spectral flexibility which is not achieved with laser systems limited to certain emission wavelengths. In order to increase the output power even further the concept can be expanded, for example, by combining multiple lasers with additional gratings or multiplexed VBGs [128],[139].

6. Extending the concept of spectrally combined diode lasers

It has been shown that beam combining with subsequent frequency conversion can be used to efficiently enhance the amount of visible laser emission. The question remains how to further increase the output power of visible diode laser systems in a compact and efficient manner. One key advantage of diode lasers is their wavelength tunability. This enables active adjustments of emission wavelengths in order to obtain phase-matching for nonlinear frequency conversion. In the above concept this principle is utilized to achieve sum-frequency generation at various crystal temperatures. The same principle can also be applied in an advanced approach involving multiple lasers. For example, in addition to SFG of two combined lasers, additional lasers can be added for simultaneous nonlinear interactions at the same crystal temperature. The generated emission will benefit from all contributions. In addition, the ability of wavelength tuning potentially enables single spectral mode emission. However, this new concept requires spectral beam combining of multiple laser. Using additional gratings increases the number of optical components and size of such setups. A more compact approach is to use multiplexed volume Bragg gratings [139]. This chapter summarizes the results obtained with frequency conversion of three diode lasers, spectrally combined in a multiplexed VBG [140].

6.1. Phase-matching for simultaneous SHG and SFG

The indicated concept of simultaneous nonlinear interactions at fixed crystal temperatures leaves the question about potential limitations. Regarding beam combining the total number of lasers is mainly limited by the custom design of the applied multiplexed grating. Each laser diffracted by the grating has to fulfill the Bragg condition. In a multiplexed grating the first combination of two lasers pre-determines the emission wavelengths and angles of incidence for any additional diffracted laser. The emission wavelength of a transmitted laser is still tunable for efficient frequency conversion. For example, in a scenario of three combined lasers one diffracted laser serves as a pump laser for frequency doubling. Obtaining the same emission wavelength by SFG of the other two lasers implies that their wavelengths are selected accordingly, using the simple relation

$$\lambda_1 = \frac{\lambda_{\mathrm{SHG}}}{1 - \frac{\lambda_{\mathrm{SHG}}}{\lambda_3}}. \tag{57}$$

Here λ_1 and λ_3 represent the fundamental wavelengths for sum-frequency generation required for obtaining the same emission wavelength as in case of SHG (λ_{SHG}). The limiting factor regarding possible wavelength combinations at fixed crystal temperatures is phase-matching. Figure 49 shows the spectral tolerance for SFG at fixed conditions. The simulation is based on the equations (35) and (37) for a lithium niobate crystal as applied in chapter 5. The crystal temperature is set to

37 °C for phase-matched SHG at 1062.4 nm. The shown curve is obtained by changing the fundamental wavelengths for SFG in accordance with equation (57).

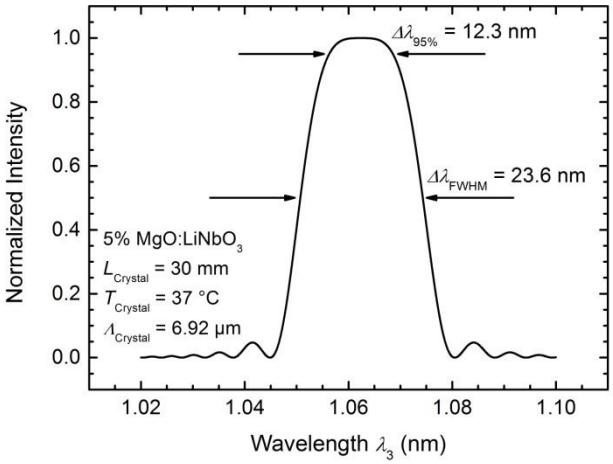

Figure 49: Simulated wavelength tolerance for quasi phase-matched SFG using a 30 mm long 5% MgO-PPLN crystal. The simulation is based on fixed crystal parameters and the fundamental wavelengths (λ_1, λ_3) are selected with respect to the desired emission wavelength of 531.2 nm.

At 50% of maximum intensity the spectral range for additional wavelength combinations at a constant crystal temperature is 23.6 nm. At 95% of maximum intensity the available wavelength span is still 12.3 nm. By engineering a multiplexed VBG with low spectral acceptance, many wavelength tunable lasers with narrow laser emission can be combined within this wavelength span. The requirements of this concept perfectly match with the unique key advantages of diode lasers, making it an ideal approach for power scaling of visible diode laser systems.

6.2. Theoretical description for simultaneous SHG and SFG

Assuming that the wavelengths of three beam combined lasers ($\lambda_1 > \lambda_2 > \lambda_3$) are selected in a manner that phase-matching is exclusively provided for SFG of λ_1, and λ_3 and SHG of λ_2, the scenario of simultaneous SHG and SFG is described by a total of five induced nonlinear polarizations and five electric fields. It should be noted that back coupling between these two processes is neglected in order to simplify the theoretical description. Under the assumption of phase-matching ($\Delta k_{SHG} = \Delta k_{SFG}$), single-mode emission ($\omega_{SHG} = \omega_{SFG}$), and zero phase delay between the second harmonic and the sum-frequency fields ($\varphi_{SHG} = \varphi_{SFG}$), solving the nonlinear wave equation results in the coupled amplitude equation for the generated emission

$$\frac{dA}{dz} = \frac{id_{\text{eff}}\omega e^{i\Delta kz}}{nc}(A_2^2 + 2A_1A_3). \tag{58}$$

Here the indices 1, 2, and 3 refer to the fundamental waves. It becomes obvious that under the above assumptions, the amplitude of the generated emission is given by the sum of the individual interactions. This also applies in case of multiple simultaneous interactions. A more detailed analysis is provided in the appendix.
The corresponding intensity is obtained by integration over the entire crystal length, which results in the following relation

$$\begin{aligned} I = &\left(\frac{2\pi^2 d_{\text{eff}}^2}{nn_2^2\lambda^2\varepsilon_0 c} I_2^2\right) L^2\, sinc^2\left(\frac{\Delta kL}{2}\right) \\ &+ \left(\frac{8\pi^2 d_{\text{eff}}^2}{nn_1n_3\lambda^2\varepsilon_0 c} I_1I_3\right) L^2\, sinc^2\left(\frac{\Delta kL}{2}\right) \\ &+ \left(\frac{4\pi^2 d_{\text{eff}}^2}{n\lambda^2\varepsilon_0 c} \frac{I_2\sqrt{I_1I_3}}{n_2\sqrt{n_1n_3}}\right) L^2\, sinc^2\left(\frac{\Delta kL}{2}\right). \end{aligned} \tag{59}$$

The equation reveals the individual contributions of SHG and SFG. A third term indicates a coupling between the two nonlinear interactions. Under the above assumptions this term represents the contribution from occurring interference effects that do not alter the total intensity, see below.

6.3. Setup for simultaneous nonlinear interactions

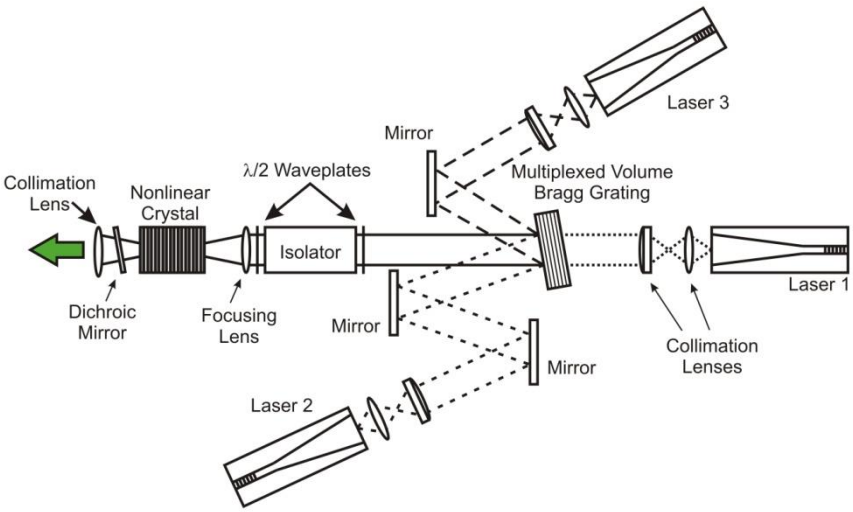

Figure 50: Setup for spectral beam combining of three lasers in a multiplexed VBG with subsequent frequency conversion.

The experimental setup for spectral beam combining in Figure 50 is similar to the setups applied above. It consists of three individual DBR-tapered diode lasers collimated and corrected for astigmatism. All lasers are positioned at roughly the same distance to a multiplexed volume Bragg grating. The VBG is 3.99 mm thick with a 10 mm x 10 mm aperture. It is designed for beam combining of three lasers and therefore contains two grating structures. The individual gratings have an average diffraction efficiency of $DE > 99\%$ and spectral acceptance bandwidths of 0.26 nm and 0.28 nm, respectively. One grating is designed for diffraction at 1062.5 nm and Bragg angles of 11.1° and 1.0° with respect to the surface normal. The second grating is designed for diffraction at 1062.0 nm wavelengths at 1.2° and -9.0°. Beam combining of three lasers is obtained by adjusting the emission wavelengths and angles of incidence until the diffracted beams overlap properly with the transmitted beam. The left part of the setup shows the optical isolation and frequency conversion analog to the setup discussed in section 5.2.

6.4. Spectral beam combining in a multiplexed grating

All three DBR-tapered diode lasers are operated at I_{RW} = 300 mA and I_{TA} = 4 A. The transmitting Laser 1 is operated at a laser temperature of 20 °C, which results in an emission wavelength of 1062.78 nm (Figure 51). In order to obtain spectral beam combining of Laser 1 and 3, the angle of incidence and the emission wavelength of Laser 3 are adjusted accordingly. The corresponding wavelength is 1062.05 nm at a laser temperature of 13 °C. Once these two lasers are combined, the position of the VBG should not be changed. This fixed position of the grating pre-defines the required wavelengths and angles of incidence for any additional laser. Spectral beam combining with Laser 2 is obtained at a laser temperature of 26.4 °C and an emission wavelength of 1063.19 nm. All three lasers provide narrow emission bandwidths with $\Delta\lambda_{FWHM} \leq 9$ pm. The measured side-lobes are suppressed by 10 dB and may be caused by unexpected optical feedback requiring further investigations.
The overlap between the three lasers is controlled by observing the beam waist profiles (Figure 52) and an image of the collimated, combined beam at a longer distance (Figure 53). Both figures indicate a good overlap of the individual lasers.
The total power measured for the individual lasers adds up to 3.78 W. After beam combining an output power of 3.39 W is measured. This results in a combining efficiency of 90%. The corresponding $M^2_{4\sigma}$ values of the combined beam are 1.9 in the slow axis and 1.5 in the fast axis (Figure 54).

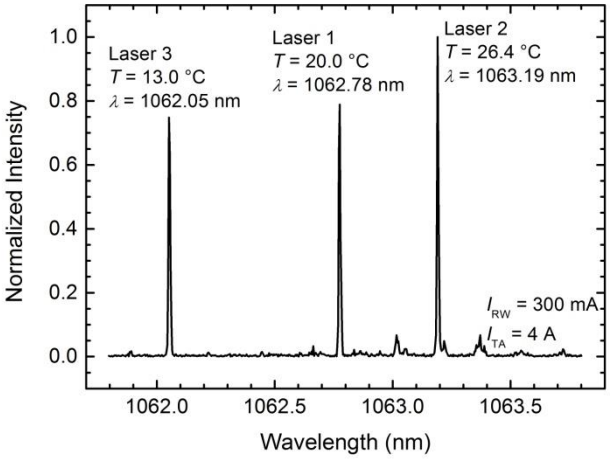

Figure 51: Resulting spectrum of three beam combined lasers, revealing the individual contributions.

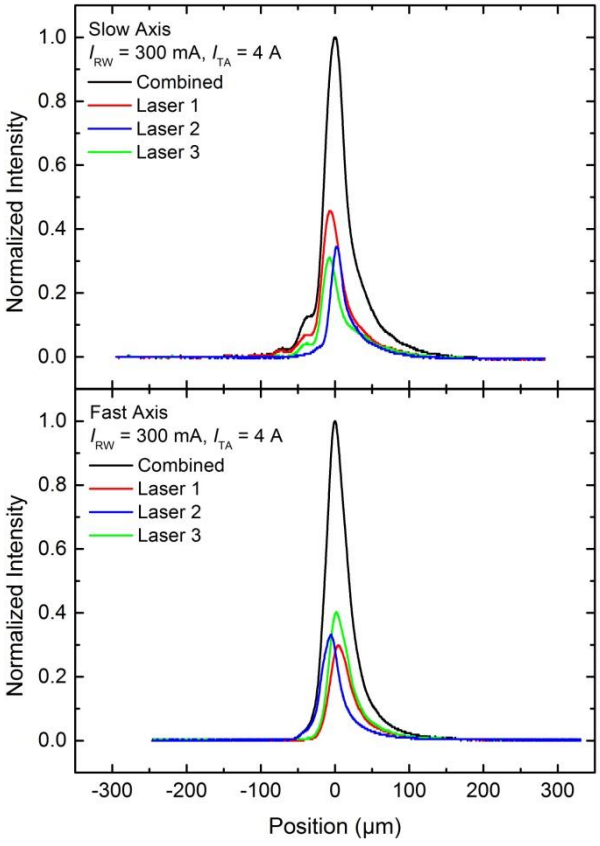

Figure 52: Normalized beam waist intensity profiles of three overlapping DBR-tapered diode lasers in both transverse directions.

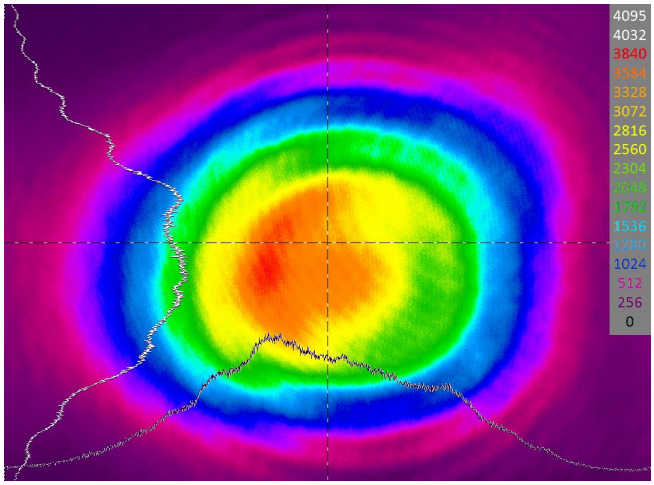

Figure 53: Image of the collimated, combined beam at a longer distance.

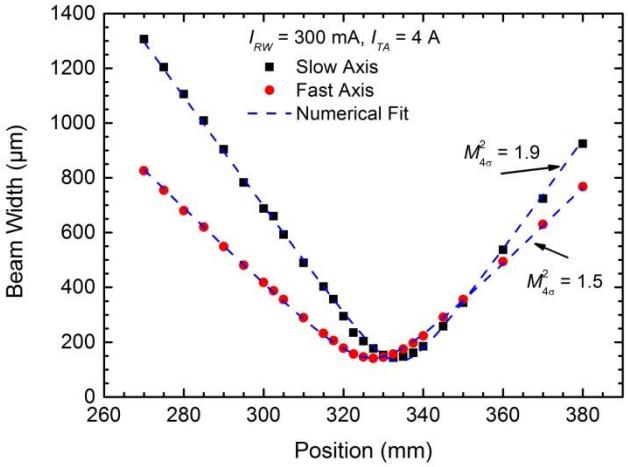

Figure 54: Beam widths of the combined beam measured along the beam waist at I_{RW} = 300 A and I_{TA} = 4 A.

6.5. Frequency conversion of three combined lasers

For simultaneous nonlinear interactions frequency doubling of Laser 2 is used as a reference. The required crystal temperature is 44.7 °C, resulting in a maximum second harmonic output power of 40 mW at 531.59 nm. The available pump power and the corresponding optical conversion efficiency are 1.03 W and 4%, respectively. Without changing the crystal position or its temperature, Laser 1 is wavelength tuned in order to obtain efficient sum-frequency generation of Laser 1 and Laser 3. The resulting laser temperature of 39.1 °C reduces the available pump

power to 0.63 W. The output power available for SFG adds up to a total of 1.76 W and results in 100 mW of green light (6%). The output power for simultaneous interactions is given by the sum of the individual nonlinear contributions and results in a total of 140 mW (5%). A second option for simultaneous interactions would have been SFG with Laser 2 and Laser 3, and SHG with Laser 1. However, this scenario was not carried out in this work

In order to obtain similar wavelengths from the two nonlinear processes, the spectral emission of Laser 1 is fine-tuned accordingly. Figure 55 shows the spectrum of green laser emission generated by simultaneous nonlinear interactions. The spectrum is located at the desired wavelength and has a spectral bandwidth < 5 pm indicating a good match between the obtained emission wavelengths. The side-lobes in Figure 55 are also observed in the near-infrared (Figure 51) and may be caused by unexpected optical feedback.

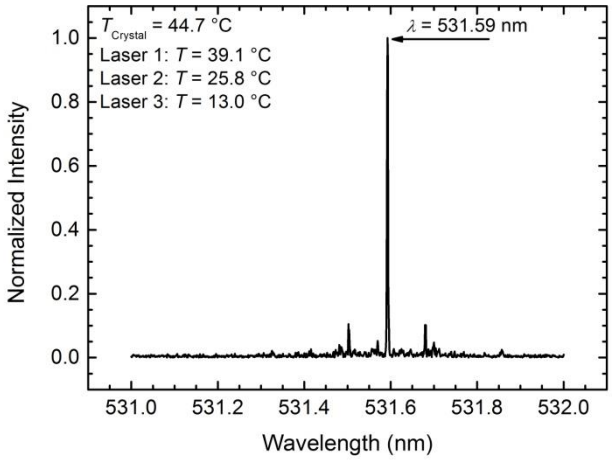

Figure 55: Emission spectrum of simultaneous SHG and SFG. At a fixed crystal temperature the wavelength of Laser 1 is adjusted in order to obtain matching emission wavelength for SHG and SFG.

Analyzing the green emission at matching wavelengths with a photodiode and an oscilloscope reveals the above mentioned interference effects resulting from the superposition of coherent waves [141]. Due to these effects the combined signal is given by the sum of the individual contributions but shows additional random modulations that are not seen in case of separate SHG and SFG (Figure 56). The random nature of this behavior may result from wavelength fluctuations of the diode lasers. The detected modulations disappear by detuning the temperature of Laser 1, which indicates the requirement of matching green emission wavelengths in order to observe these effects.

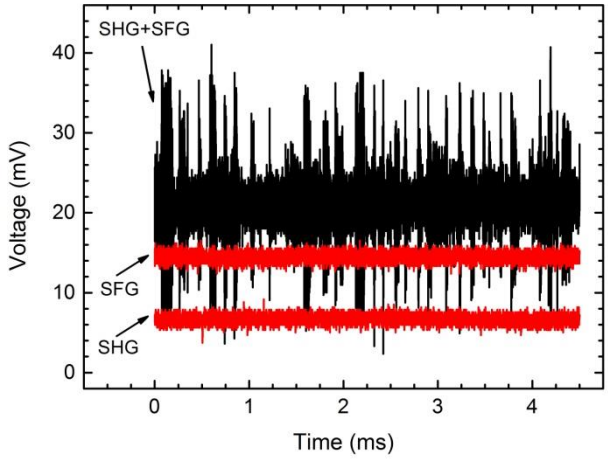

Figure 56: Direct comparison of the measured photodiode signal at individual and simultaneous SHG and SFG. The measurement reveals the onset of interference effects caused by the superposition of coherent waves.

The spatial quality of the combined green beam shows values of $M^2_{4\sigma}$ = 2.3 in the slow axis and $M^2_{4\sigma}$ = 1.6 in the fast axis (Figure 57). The measured values are comparable to the fundamental laser emission but indicate the lack of spatial filtering as observed in Section 5.3. In order to improve the spatial quality of simultaneous nonlinear interactions the overlap of the involved beams needs to be improved even further.

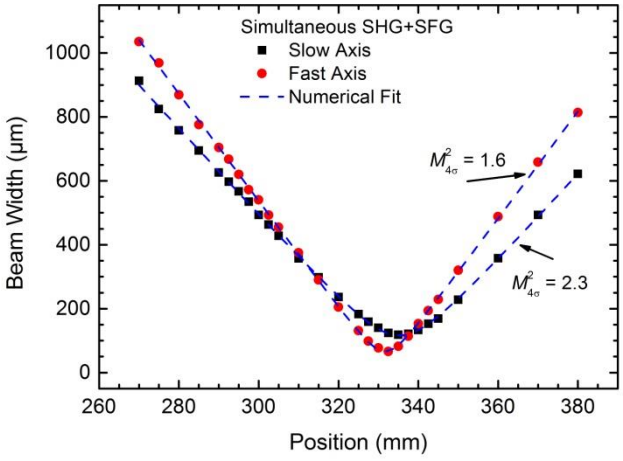

Figure 57: Beam widths of the simultaneously generated green emission measured along the beam waist.

Frequency conversion of three beam combined lasers enables a total of six nonlinear interactions. Figure 58 shows the generated output power as a function of crystal

temperature. Due to the different emission wavelengths of the three lasers separated by 1 nm, the individual nonlinear contributions can be clearly distinguished by their phase-matching temperature. The only exception is the central maximum that is based on simultaneously phase-matched frequency doubling and sum-frequency generation. The difference in output power for comparable nonlinear interactions results from variations in fundamental pump power due to increased laser temperatures, the overlap of the individual lasers, and the crystal position being optimized for SHG of Laser 2 and SFG of Laser 1 and Laser 3.

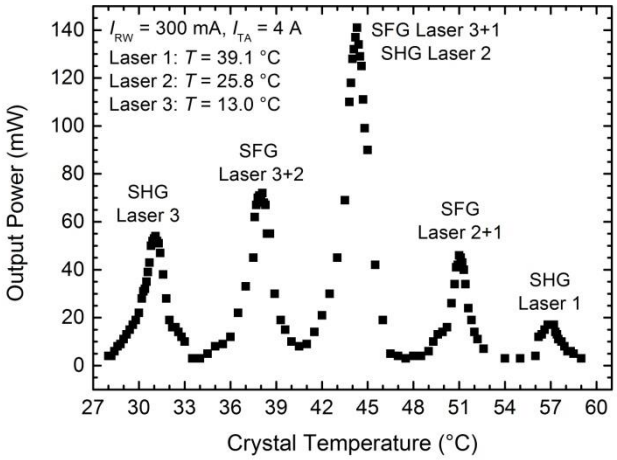

Figure 58: Output power as a function of crystal temperature in case of nonlinear frequency conversion with three combined fundamental lasers. Each maximum represents phase-matching for the corresponding nonlinear interaction. The central maximum consists of contributions from simultaneous SHG and SFG.

The results indicate that spectral beam combining with subsequent nonlinear frequency conversion can be expanded using multiple lasers and a multiplexed VBG. The total number of lasers to be combined in a single grating is limited by its design parameters. The number of simultaneous frequency conversions with multiple lasers is limited by the spectral acceptance bandwidth of the nonlinear crystal. It is shown that the output power in such systems is determined by the sum of the individual contributions, indicating the great potential towards power scaling in advanced diode laser systems.

7. Diode laser based pumping of titanium sapphire lasers

Regarding biomedical applications of green diode laser systems, the main focus in this work is on direct pumping of Ti:sapphire lasers for optical coherence tomography (OCT). In most cases green emission is provided by frequency converted solid state lasers, which can have low wall-plug efficiencies and significantly add to the dimensions and price of Ti:sapphire laser systems. Obtaining the required high-power green light emission directly with simple and more efficient diode lasers is challenging. Applying nonlinear frequency conversion can overcome these limitations. This chapter summarizes the results obtained by direct pumping of Ti:sapphire lasers with a frequency doubled diode laser [142].

7.1. Direct pumping of Ti:sapphire lasers

Ti:sapphire lasers belong to the group of transition-metal-ion lasers characterized by a tunability over a wide spectral range of several hundred nanometers [2],[143]. In case of titanium doped sapphire laser crystals the laser emission ranges between 600 nm - 1100 nm [144]. In mode-locked operation Ti:sapphire lasers provide ultrashort femtosecond pulses [145] that are required in many biomedical imaging applications such as two-photon microscopy, coherent anti-Stokes Raman scattering microscopy or optical coherence tomography [33],[34],[35].

Ti:sapphire lasers are characterized by a maximum absorption around 500 nm [143] and high pump thresholds. Therefore, pump lasers should ideally provide more than 1 W (CW) of green light with good spatial quality and high efficiencies without adding to the size of the Ti:sapphire systems. Direct pumping of Ti:sapphire lasers has been demonstrated with laser systems such as argon-ion lasers, neodymium based solid state lasers, thin disk lasers or fiber lasers [143],[146],[147],[148],[149].

A more efficient approach towards green laser emission is the use of direct green light emitting lasers. Green emitting diode lasers were shown with output powers up to 1 W limited by the laser crystal qualities or spatial qualities [150],[151]. With diode pumped Pr^{3+}-doped laser crystals more than 700 mW were obtained at 523 nm [152].

A solution towards increased output powers of several watts is frequency conversion of optically pumped infrared lasers [85],[109],[153]. Direct pumping of Ti:sapphire lasers with a 5 W frequency doubled optically pumped semiconductor laser resulted in an output power of 0.5 W at pulsewidths < 20 fs [154]. A major disadvantage of such configurations is that two conversion processes are required to generate green light, which negatively affects the overall wall-plug efficiencies.

These drawbacks are overcome by more efficient blue diode lasers or frequency converted diode lasers that may also lead towards low-cost Ti:sapphire lasers with small footprints. In addition, the short upper-state lifetimes of diode lasers in comparison to ≈ 3 µs for Ti:sapphire laser crystals [137],[144] reduce the risk of transferring intensity noise caused by relaxation oscillations to the output of the

Ti:sapphire laser. Different groups examined the potential of blue gallium nitride based pump lasers with output powers of $P \approx 1$ W. Direct pumping at 450 nm resulted in Ti:sapphire laser emission of 13 mW at pulsewidths of 114 fs [155]. Up to 101 mW and pulsewidths of 15 fs were obtained with double-sided pumping [156],[157]. Unfortunately, pumping at such short wavelengths introduced additional losses within the laser crystal that significantly reduced the conversion efficiencies and were not observed at green pump wavelengths [155].
This leaves the option of frequency converted diode lasers. As shown above, DBR-tapered diode lasers fulfill all requirements for efficient green light generation [32],[103], and frequency conversion results in high-power emission with good spatial quality. Based on previous results obtained with a single emitter, a portable and robust green diode laser system is developed for direct pumping of Ti:sapphire lasers.

7.2. Experimental setup for a diode based pump laser

The setup illustrated in Figure 59 is a more compact version of the approach published by Jensen *et al.* [32]. A 1062 nm DBR-tapered diode laser is collimated in both axes, corrected for astigmatism, and protected against optical feedback. The diode laser is connected to an electronic filter that suppresses electronic noise from the high-power switch-mode power supply and therefore prevents a noise transfer when pumping a Ti:sapphire laser. In order to reduce the footprint of the setup, two mirrors tilt the beam over 180°. A lens with a focal length of $f = 100$ mm generates a beam waist of approximately 60 µm inside the 5% MgO:$LiNbO_3$ crystal. A dichroic mirror separates the second harmonic from the fundamental laser emission. An additional lens with a focal length of $f = 200$ mm collimates the green light to an approximately 2.5 mm wide beam for further experiments.

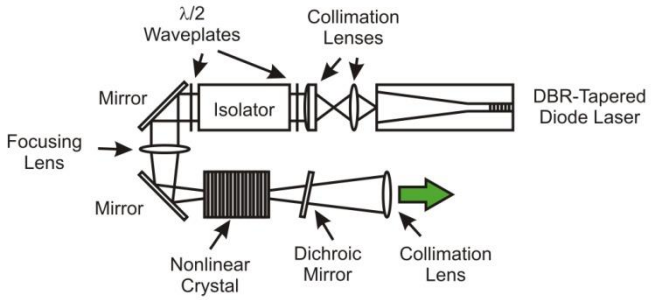

Figure 59: Experimental setup for compact diode laser based single-pass frequency conversion.

7.3. Characterization of the diode based pump laser

The RW and TA of the diode laser are operated at injection currents of 300 mA and 14 A, respectively. The maximum fundamental pump power available for frequency conversion is 8.8 W. Second harmonic generation at a crystal temperature of 37 °C results in a maximum of 1.28 W of green light (Figure 60). The maximum conversion efficiency is 14.5%. The corresponding nonlinear and wall-plug efficiencies are 1.9 %/W and 4%, respectively.

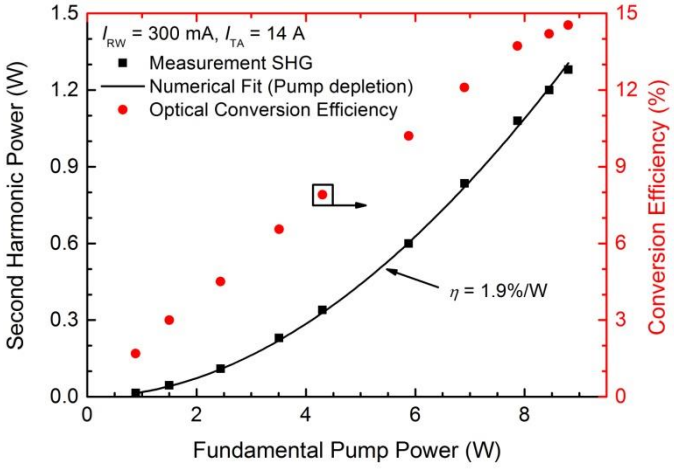

Figure 60: Second harmonic power and conversion efficiency versus pump power of the frequency converted diode laser.

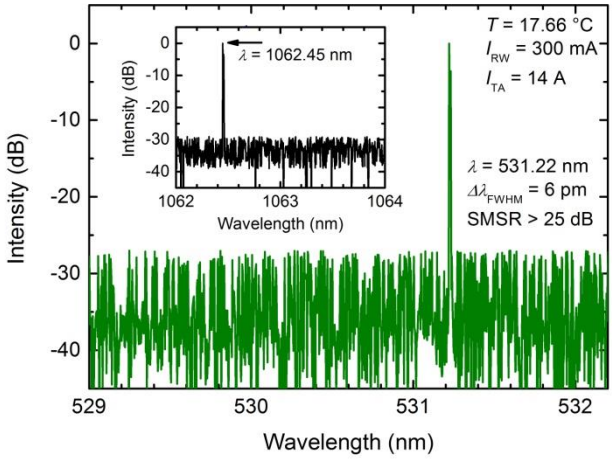

Figure 61: Spectrum of the second harmonic at maximum performance. The inset shows the fundamental emission spectrum.

Optimum phase-matching is obtained at a laser temperature of 17.66 °C. This results in fundamental and second harmonic emission wavelengths of 1062.45 nm and

531.22 nm, respectively (Figure 61). Due to the intrinsic wavelength stabilization of the laser, the fundamental and second harmonic emission show narrow spectral bandwidths of $\Delta\lambda$ = 6 pm and side-mode suppressions > 25 dB.
With spatial qualities of M^2 = 1.3 in the fast axis and M^2 = 1.4 in the slow axis the generated green emission is nearly diffraction-limited (Figure 62). The amount of power contained in the central lobe ($1/e^2$) is 94%.

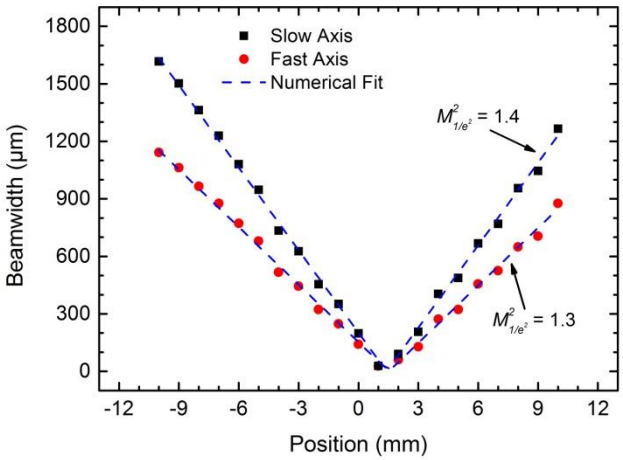

Figure 62: Measured $1/e^2$ beam widths of the second harmonic radiation at maximum performance. The numerical fit shows a good agreement with the data points and indicates nearly diffraction limited emission.

7.4. Experimental results for diode pumped Ti:sapphire lasers

The compact Ti:sapphire laser is illustrated in Figure 63. It was introduced as a highly stable, reproducible, user-friendly, low-cost oscillator with high potential for clinical applications [158].
In the experiments a spherical lens (f = 35 mm) is applied for focusing green emission into the Ti:sapphire laser crystal. The corresponding pump laser is selected with a flip mirror. The laser crystal has a total length of 3 mm and is positioned at Brewster angle. In addition, the crystal is characterized by a figure of merit > 150 and an absorption coefficient of α = 4.5 cm^{-1}. The former is defined by the ratio of the absorption coefficients at the pump and emission wavelengths [159].
The Ti:sapphire laser is based on an x-folded, Kerr lens mode-locked oscillator. It consists of several chirped mirrors compensating for dispersion. Curved mirrors (M_1, M_2) with a radius of curvature of R = 50 mm generate a beam waist of 18 µm inside the crystal. Kerr lens mode-locking is obtained by a change in the stability range and external perturbations to one end mirror (M_3). Using the Kerr effect inside the Ti:sapphire crystal, these perturbations cause intensity dependent changes of the refractive index, resulting in more efficient pulsed moded operation. With a length

of about 1.75 m and $v_{Rep} = c/2L$ [53], the repetition rate v_{Rep} of this oscillator exceeds 80 MHz. The second end mirror (M_4) is used as an output coupler with 3% transmission for additional measurements.

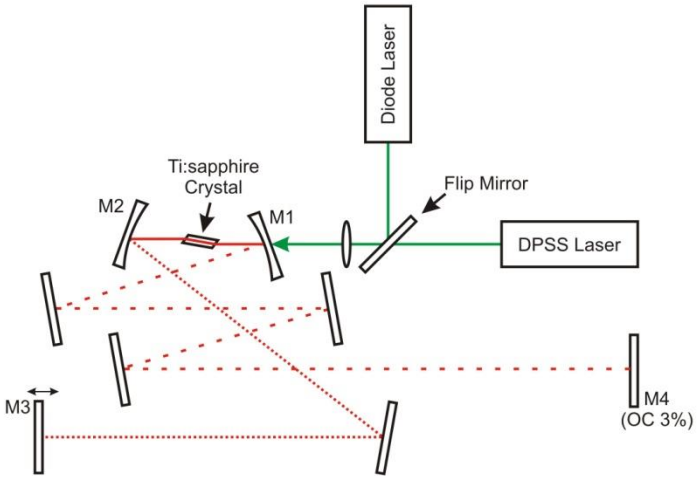

Figure 63: Illustration of the Ti:sapphire oscillator used in the experiments. The two arms of the 1.75 m long oscillator are shown with dashed and dotted lines. A flip mirror is used to select a laser system for direct pumping.

The commercial pump laser used for comparison is a diode pumped solid state (DPSS) laser (*Laser Quantum, Excel Laser*). It provides a diffraction limited beam (M^2 < 1.1) with a beam diameter of 1.8 mm and a maximum power of 1.5 W at 532 nm. Its wall-plug efficiency is below 2%.

When pumping the Ti:sapphire laser with the commercial system, a maximum power of 180 mW is obtained (Figure 64). The corresponding conversion efficiency from green to near-infrared is 12%. Direct pumping with 1.1 W from the diode laser leads to an emission of 105 mW. The optical conversion efficiency is reduced to 9.5%. Exchanging the collimation lens (f = 160 mm) in order to reduce the beam width of the diode laser down to 2 mm, has a negligible effect and results in a maximum of 110 mW at 1.2 W of green light (9.2%). Compared to the commercial pump laser similar noise properties are measured.

The direct comparison shows that direct pumping with the commercial DPSS laser exceeds the performance achieved with the diode laser by 20 mW to 30 mW at similar pump powers. This deviation corresponds to a 25% drop in optical conversion efficiency for a diode pumped Ti:sapphire laser. The estimated pump threshold increases from 0.2 W to 0.33 W. The slope efficiency decreases from 13.8% to 12.7%. The advantage of diode pumped Ti:sapphire lasers becomes obvious when comparing the wall-plug efficiencies. Due to the superior efficiency of the diode laser the wall-plug efficiency of the Ti:sapphire laser is still improved by a factor > 2.

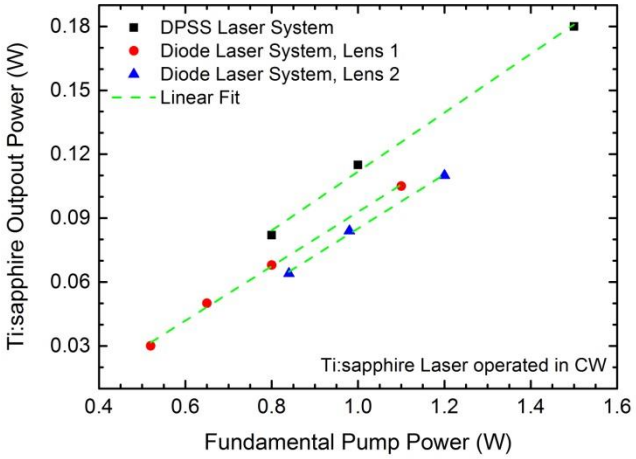

Figure 64: Obtained output power of the direct pumped Ti:sapphire laser operated in CW mode. Lens 1: f = 200 mm. Lens 2: f = 160 mm.

The deviation observed for CW Ti:sapphire lasers is also seen in mode-locked operation (Figure 65). With the diode laser, a maximum of 82 mW is obtained at 1.2 W of pump power (6.8%). The maximum efficiency of 7.1% is measured at a larger beam width, generating 78 mW. Applying the commercial pump laser, 86 mW are achieved at 1 W of pump power (8.6%).

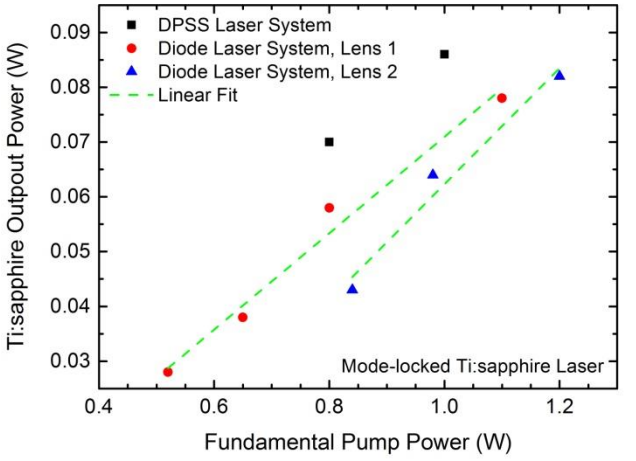

Figure 65: Obtained output power of the direct pumped, mode-locked Ti:sapphire laser (f_1 = 200 mm, f_2 = 160 mm).

One explanation for reduced optical conversion efficiencies obtained with the diode laser can be the reduced spatial quality negatively affecting the overlap of the pump beam and generated emission within the Ti:sapphire crystal. In addition, no changes were made to the oscillator when switching from a commercial to a diode based

pump laser. An optimization with respect to the diode laser could reduce or eliminate the observed deviations.

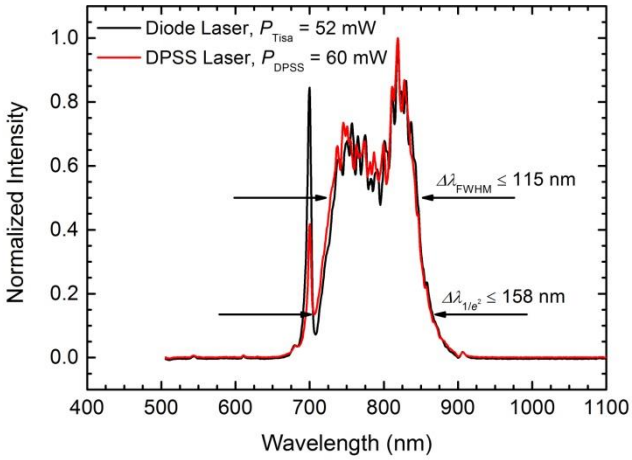

Figure 66: Emission spectra of a mode-locked Ti:sapphire laser directly pumped with a diode laser or DPSS laser.

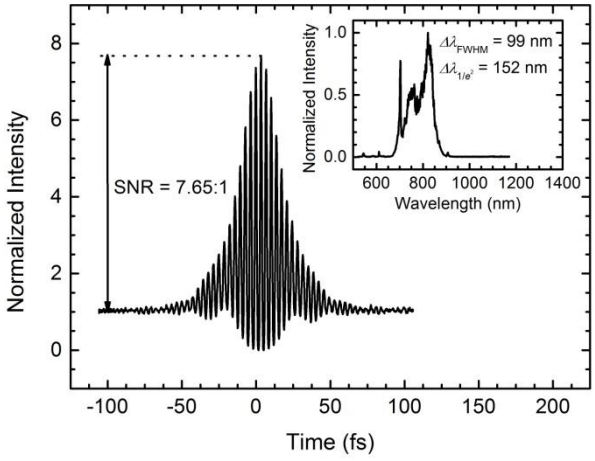

Figure 67: Interferometric autocorrelation trace of the diode pumped Ti:sapphire laser. The inset shows the corresponding spectrum of the mode-locked laser.

In order to estimate the performance of the mode-locked Ti:sapphire laser, emission spectra and interferometric autocorrelation traces are measured. Both pump lasers are set to 1.2 W of pump power. This results in a Ti:sapphire laser emission of 52 mW with the diode laser and 60 mW with the commercial system. The reduced performance compared to the results shown above is due to changes made for the oscillator in order to achieve maximum bandwidths. The emission spectra obtained in mode-locked operation show spectral widths of $\Delta\lambda_{FWHM}$ = 112 nm for the diode

laser and $\Delta\lambda_{FWHM}$ = 115 nm for the commercial laser, respectively (Figure 66). The spectral widths measured according to the $1/e^2$ criteria are 158 nm and correspond to bandwidths of 78 THz. The distinct side-lobes at 700 nm of the measured spectra are caused by a sharp phase change induced by the chirped mirrors.

The interferometric autocorrelation trace for the diode pumped Ti:sapphire laser is shown in Figure 67. From this trace a pulse width of less than 20 fs is estimated. The trace shows slightly imperfect alignment and dispersion management. This is indicated by the unusual behavior in the wings of the trace and a reduced signal-to-noise ratio of 7.65:1 compared to the ideal ratio of 8:1 [160]. Due to the non-Gaussian spectral profile the generated pulses are not transform limited, which would result in minimum pulse widths [161].

It is demonstrated that frequency doubled diode lasers are suitable for direct pumping of ultrashort pulsed Ti:sapphire lasers. Compared to a commercial pump laser, similar noise properties are measured. The reduced power performance with the diode laser can be compensated by a superior wall-plug efficiency. Further optimization of the oscillator with respect to the diode laser may help to improve the pump conversion efficiency. In addition, smaller footprints of diode based pump lasers will enable more efficient, low-cost Ti:sapphire lasers with reduced dimensions.

8. Diode pumped Ti:sapphire lasers for OCT

Despite the promising results achieved with direct pumping of Ti:sapphire lasers, the question remains how diode pumped Ti:sapphire lasers perform in biomedical applications such as optical coherence tomography (OCT). This chapter summarizes the results obtained with a diode based system applied to the skin and retina [162].

8.1. Optical coherence tomography

OCT is a well-established, non-invasive, *in vivo* imaging technique in order to obtain 3D images of the morphology of biological tissues [163]. It allows for applications such as early detection of retinal pathologies, guiding of surgical and microsurgical procedures, and optical biopsy often in conjunction with screening of early malignancies [164].

The underlying principle is interferometric imaging of a scattering sample. Light of a low coherent source is split up into a reference arm and a sample arm of an interferometer. In time-domain OCT, depth resolved images are obtained by monitoring the interference intensity while continuously changing the longitudinal path length of the reference arm [164]. Once the path differences between the two arms are within the coherence length of the source a cross-correlated signal is measured and can be translated into depth information. Such a single local measurement is called an A-scan. Lateral scanning across the sample enables the reconstruction of cross-sectional images, which can be stacked to obtain a three dimensional view.

In frequency-domain OCT, the reference arm is fixed and depth resolved images can be obtained by evaluating the measured interference pattern with a spectrometer. The Fourier transform of the measured spectrum provides depth-resolved reflectivity profiles [164]. The measurable penetration depth is given by the ability of the detector to measure high frequencies. Without a required movement of optical components, this method is faster and more stable than time-domain imaging. Furthermore, measuring individual spectral components rather than the entire interference signal increases the sensitivity [165].

The transverse resolution of an OCT system is determined by the ability to focus the incident beam. The axial resolution Δl is given by the following relation [164]

$$\Delta l = \frac{2ln2\lambda_0^2}{\pi\Delta\lambda}. \tag{60}$$

According to this equation the axial resolution mainly depends on the center wavelength λ_0 and the bandwidth $\Delta\lambda$ of the applied light source. Typical sources are broadband near-infrared lasers with center frequencies located within a range of 700 nm - 1300 nm. Compared to longer wavelengths or the visible spectral range, this spectral region enables increased penetration depths because of 2 - 3 orders of

magnitude lower absorption by main tissue components such as water, hemoglobin, and melanin [166]. Due to the wavelength dependent optical tissue properties affecting the penetration depth, contrast, and axial resolution, the laser parameters have to be properly chosen [167].

8.2. Diode based laser system for OCT measurements

Based on the concept shown in chapter 7, a compact green diode laser with a footprint of 140 mm x 90 mm is developed for a potential integration into a Ti:sapphire laser system. The laser is collimated using an aspheric lens with a focal length of f = 2 mm (NA = 0.5) and a cylindrical lens with a focal length of f = 4 mm (NA = 0.5). The combination of these two lenses generates a nearly circular beam with roughly 1 mm in diameter. In order to prevent optical feedback the AR-coated lenses are followed by a 30 dB optical isolator and a $\lambda/2$ waveplate. In between two mirrors positioned at angles of 45° an achromat with a focal length of f = 40 mm generates a beam waist of about 35 µm, which proved to be optimum in the experiments.

Frequency conversion is carried out in a 30 mm long, 10° angle cut 5% MgO:$LiNbO_3$ crystal (*HCPhotonics*). Although angle cut crystals are especially applied to suppress optical feedback, the optical isolator still has to be used to protect the diode laser. The periodically poled crystal has a poling period of 6.92 µm.

Behind the crystal, the fundamental laser emission and the second harmonic are separated with a dichroic mirror. An additional lens (f = 75 mm) collimates the green laser radiation to an approximately 1 mm wide beam available for direct pumping of Ti:sapphire laser oscillators.

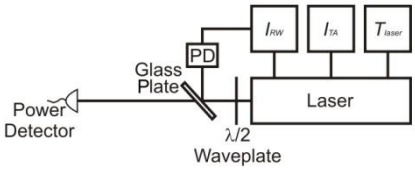

Figure 68: Setup for active stabilization of the green diode laser system using electronic feedback from a photodiode (PD).

In order to apply this diode laser in an OCT setup, it should ideally provide sufficient output power (P > 1.3 W) with a power stability of ± 0.5%. In the described setup the diode laser is stabilized by an external photodiode feedback loop regulating the injection current to the RW of the laser (Figure 68). Figure 69 shows the corresponding measurement over one hour. Due to the feedback loop the output power of 1.45 W is kept stable within ± 3 mW (± 0.2%), which fulfills the requirements given above.

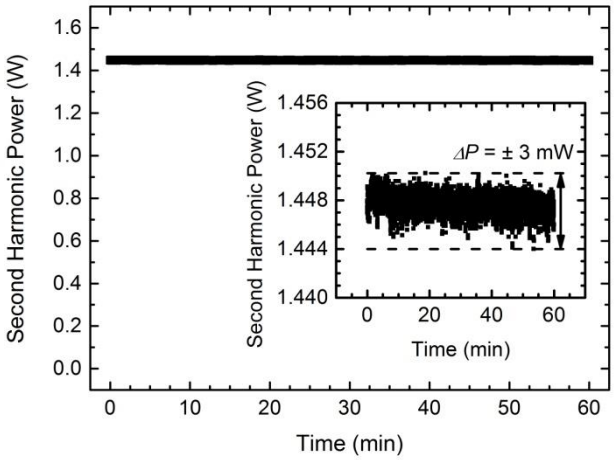

Figure 69: Output power of the compact green diode laser system measured over one hour. The inset shows an enhanced view of the measured data points.

8.3. OCT imaging with a diode pumped Ti:sapphire laser

The diode pumped Ti:sapphire laser is based on an oscillator as previously introduced in [158] and section 0. For retina measurements the oscillator is integrated into a spectrometer based frequency-domain OCT system (Figure 70). The OCT device is based on a solid state pumped Ti:sapphire laser system with a light emitting diode fixation target (FIX) and a scanning laser ophthalmoscope (SLO) for tracking eye-motion. The fiber based design of the OCT system enables simultaneous integration of different light sources, as indicated here with a direct diode pumped Ti:sapphire laser (DDPSSL) and a superluminescent diode (ASE). Fiber-optic couplers split the emission into a shared patient interface and external delay reference arms (REF). Each reference arm consists of a fiber coupled collimator, an attenuator, and a reflector. This compensates differences in dispersion caused by fiber length mismatches and the propagation in biological tissue. The interference signals are evaluated using camera-based spectrometers. The corresponding cameras are selected with respect to the applied wavelengths. Data acquisition and processing are used for real time display of the obtained images. The speed of the OCT system is given by depth sampling line rates of 70 kHz.

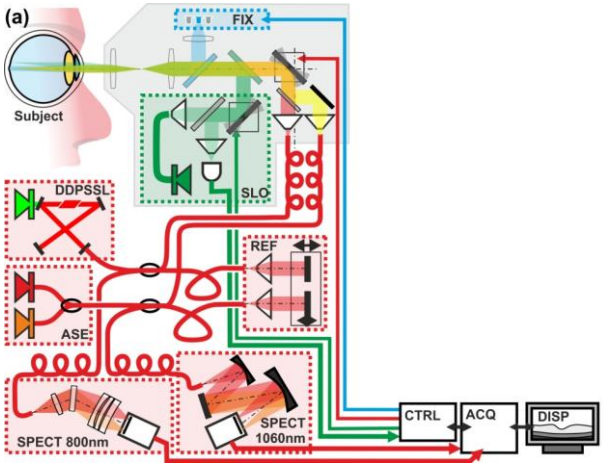

Figure 70: Experimental setup for a dual wavelength OCT system for retina imaging. (Courtesy of A. Unterhuber, Med. Univ. Vienna)

Retina measurements are carried out with different light sources. The corresponding source parameters are summarized in Table 3. For eye safety the output powers are reduced below the safety limit. Figure 71 shows a direct comparison of the OCT images obtained with different light sources at 800 nm and 880 nm.

The images show that the low absorption at 800 nm in an ocular medium is well suited for obtaining information about the architectural morphology of the retina as an indicator of pathological changes [168],[169]. It should be noted that the images are averaged over 100 (a), 50 (b), and 20 frames (c). The difference in the number of frames is based on the axial resolution with the individual sources. Averaging images with high axial resolution allows for a low number of frames. Saturations effects at larger numbers would reduce the image quality. On the other hand, low resolution images can be averaged with multiple frames in order to improve the final image. The direct comparison of the three sources reveals the difference in resolution resulting from the applied emission bandwidths listed in Table 3. While the image obtained with the superluminescent diode shows a poor axial resolution, the difference becomes less obvious when comparing Ti:sapphire lasers with moderate (b) or ultrabroad bandwidths (c).

Table 3: Spectral bandwidths and output power of different sources applied in retina OCT measurements.

Light source	Spectral bandwidth $\Delta\lambda_{FWHM}$ / nm	Applied output power P / mW
Diode pumped Ti:sapphire laser	90 @ 800 nm	0.8
Solid state pumped Ti:sapphire laser	170 @ 800 nm	0.8
Superluminescent diode	47 @ 880 nm	1.2
Superluminescent diode	111 @ 1070 nm	4.0

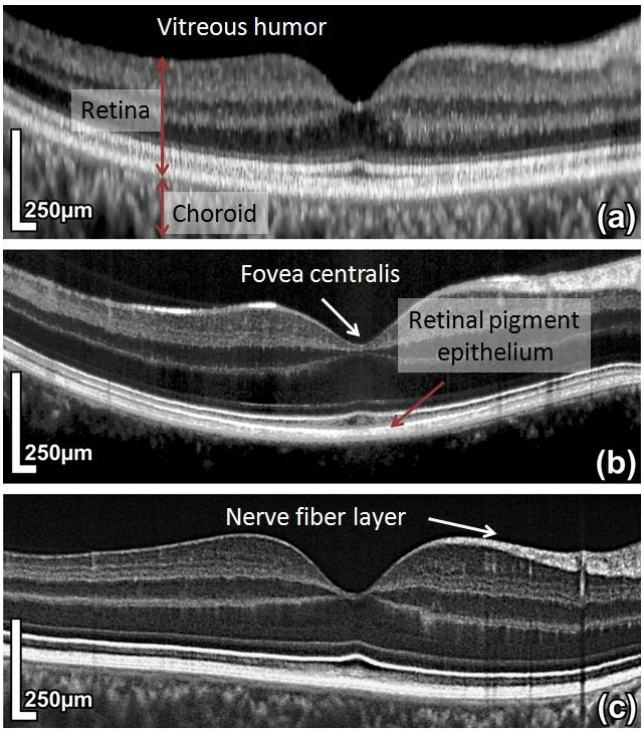

Figure 71: In vivo OCT image of the retina at center wavelengths of 800 nm and 880 nm. The images show the results obtained with a superluminescent diode (a), a diode pumped Ti:sappire laser (b) and a solid state pumped ultrabroad bandwidth Ti:sapphire laser system (c).

Applying sources around 800 nm helps to resolve intraretinal layers down to the choroid. The main limiting factor regarding the penetration depth is the strong scattering and absorption by melanin in the retinal pigment epithelium. In order to penetrate deeper into the choroid longer wavelengths need to be applied. Figure 72 shows a direct comparison of images obtained with different light sources at comparable bandwidths. It can be seen that the longer center wavelength of a 1070 nm superluminescent diode enables imaging below the retinal pigment epithelium at the expense of axial resolution. Comparing the images obtained with Ti:sapphire lasers shows that the image for the solid state pumped laser systems seems to be more grainy, which may result from dispersion compensation artifacts in the setup.

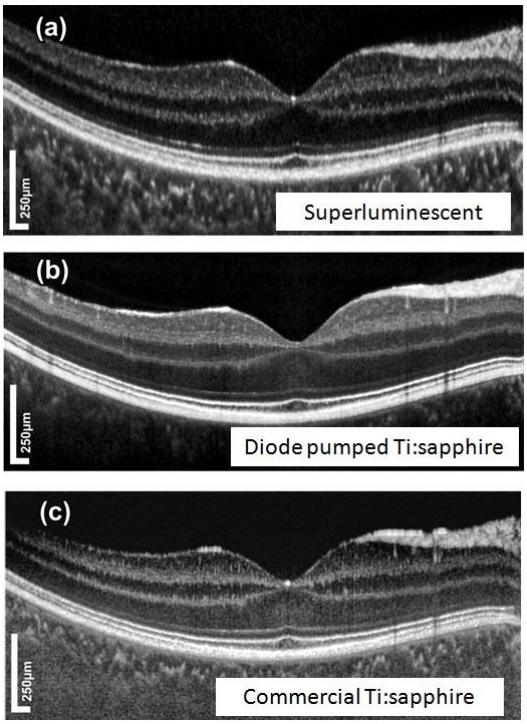

Figure 72: In vivo OCT image of the retina at center wavelengths of 800 nm and 1070 nm. The images show the results obtained with a superluminescent diode (a), a diode pumped Ti:sappire laser (b) and a solid state pumped Ti:sapphire laser system (c) at comparable bandwidths.

For skin measurements a similar OCT system is applied enabling a transversal resolution of 12 µm over a scanned region of approximately 8 mm x 8 mm with 1024 sampling points per B-scan. The image acquisition rate is 47 kHz (47000 A-scans/s). The source parameters applied in the measurements are summarized in Table 4.

Table 4: Spectral bandwidths and spatial resolutions for light sources applied in OCT skin measurements.

Light source	Spectral bandwidth $\Delta\lambda_{FWHM}$ / nm	axial resolution Δl / µm
Diode pumped Ti:sapphire laser	30 @ 800 nm	< 10
Diode pumped Ti:sapphire laser	90 @ 800 nm	< 4
Solid state pumped Ti:sapphire laser	240 @ 800 nm	< 3

Skin imaging is of high importance in order to diagnose morphological changes that are potentially caused by malignant conditions and various skin diseases occurring in epithelial tissues. [170],[171],[172]. Using OCT based imaging techniques, the obtained imaging depth of about 1 mm - 2 mm is comparable to typical mechanical biopsies. In comparison to this traditional method, optical biopsy allows for *in situ*,

real-time measurements with high resolution and has become a promising non-invasive technique for imaging of micro-morphological details in tissue. Skin OCT has been demonstrated in numerous applications such as tumor detection [173], monitoring of wound healing processes and treatment effects [174],[175], and the analysis of inflammatory skin conditions and burn depths [172],[176].
Figure 73 shows skin images obtained with all three Ti:sapphire laser systems. The images are acquired at an output power of 2 mW. In all cases, the images visualize the morphology of several cutaneous layers such as the epidermis and dermis, which is of significant importance for early cancer detection [177]. In direct comparison to the solid state pumped system the image quality at reduced spectral bandwidths is sufficient and in principle allows measurements at reduced green pump power. In all cases the achieved penetration depths are mainly limited by the emission wavelength. Longer wavelength may be required in order to obtain greater depths at the expense of axial resolution.

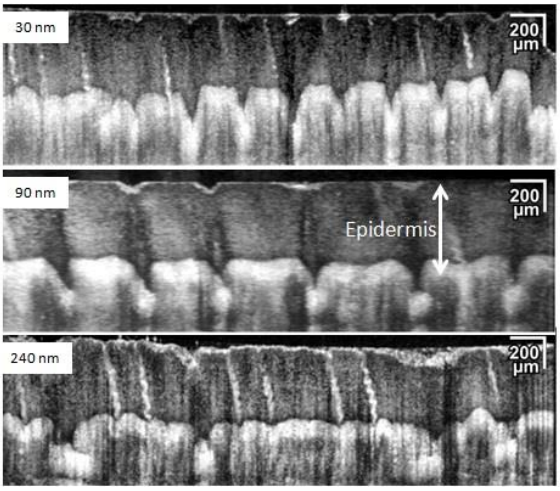

Figure 73: In vivo OCT image of human skin obtained with 800 nm Ti:sapphire lasers. The upper two images show standard resolution OCT with a diode pumped Ti:sapphire laser at different spectral bandwidths. The bottom image shows ultrahigh resolution OCT with a solid state pumped system.

The results obtained for retina and skin OCT clearly show the potential of diode pumped Ti:sapphire laser systems for OCT measurements. In direct comparison with solid state pumped systems a diode pumped laser provides similar results. Increased pump thresholds for ultrabroad bandwidth Ti:sapphire lasers in high-resolution OCT systems may be overcome by implementing high-power beam combined green diode lasers, strengthening the application potential of diode lasers in this biomedical field.

Conclusion

Diode lasers are increasingly attractive for numerous applications. In the biomedical field the provided output power, spatial emission properties, and wavelength coverage of diode lasers have been decisive aspects for their applications in dermatology, diffuse spectroscopy and imaging, or fluorescence measurements. One major challenge in diode laser technology is to obtain high-power laser emission at wavelengths < 600 nm. Especially the green spectral range is of high importance for dermatological applications or in direct pumping of ultrashort pulsed lasers in conjunction with optical coherence tomography, two-photon microscopy or coherent anti-Stokes Raman scattering microscopy.

Nonlinear frequency conversion of state-of-the-art near-infrared diode lasers represents a necessary means to overcome these current limitations in diode laser technology. Unfortunately, frequency doubling of a single emitter is limited by thermal effects potentially resulting in laser degradation and failure. In this work new concepts for power-scaling of green diode laser systems are introduced, enhancing their application potential.

The underlying principle for power scaling is spectral beam combining. This technique incoherently combines multiple lasers with an external optical component. With two 1062 nm DBR-tapered diode lasers and a reflecting volume Bragg grating more than 16 W of output power at combining efficiencies > 93% are obtained. In comparison to lasers limited to specific atomic transitions the wavelength tunability of diode lasers simplifies the process of obtaining an overlap of the combined beams. Without affecting the spatial properties of the combined beams, spectral beam combining of diode lasers has a high application potential in conjunction with efficient, compact and cost-effective laser systems with increased brightness.

The condition of overlapping beams proves to be an ideal condition for subsequent frequency conversion. Based on sum-frequency generation of two beam combined diode lasers the amount of green light compared to single emitter frequency doubling is increased by a factor of 2.5 - 3.2. At maximum performance 3.9 W are achieved. It is also shown that nonlinear frequency conversion significantly improves the spatial quality. Generating multiple watts of diffraction-limited green light therefore increases the biomedical application potential of such diode laser systems.

In order to increase the output power even further, the developed concept can be expanded combining multiple diode lasers in a multiplexed grating. This is shown for the example of three lasers incoherently combined in a compact and efficient manner. In case of frequency conversion, the unique tunability of diode lasers allows for matching emission wavelengths of simultaneous nonlinear interactions. The obtained output power is given by the sum of the individual contributions and indicates the potential for power scaling. The limiting factors in terms of extending the concept are the grating properties and the acceptance bandwidths of nonlinear crystals. Within these limits future setups can be based on an increased number of

simultaneous nonlinear frequency conversions, leading towards advanced, visible, high-power diode laser systems.

In order to prove the application potential of green diode laser systems, a frequency doubled DBR-tapered diode laser is applied for direct pumping of a mode-locked Ti:sapphire laser. The resulting pump efficiencies are reduced to 75% of the values achieved with a commercial green diode pumped solid state laser. However, due to a superior wall-plug efficiency of the diode laser the overall efficiency of the Ti:sapphire laser is improved by a factor of 2. In mode-locked operation, a spectral bandwidth of 112 nm (FWHM) allows for sub-20 fs short pulses and proves the competitive potential of diode lasers in conjunction with compact and efficient diode pumped Ti:sapphire lasers.

Applying a diode pumped Ti:sapphire laser in OCT measurements of the retina and skin shows similar results as obtained by solid state pumped systems. Implementing the developed concept of beam combining based green diode laser systems will help to overcome the high pump threshold for ultrabroad bandwidth Ti:sapphire lasers required for high-resolution OCT, and strengthen the application potential of diode lasers in this biomedical field.

References

[1] T. H. Maiman, Nature **187**, 493-494 (1960).

[2] O. Svelto, S. Longhi, G. Della Valle, S. Kück, G. Huber, M. Pollnau, H. Hillmer, S. Hansmann, R. Engelbrecht, H. Brand, J. Kaiser, A. B. Peterson, R. Malz, S. Steinberg, G. Marowsky, U. Brinkmann, D. Lot, A. Borsutzky, H. Wächter, M. W. Sigrist, E. Saldin, E. Schneidmiller, M. Yurkov, K. Midorikawa, J. Hein, R. Sauerbrey, and J. Helmcke, Springer Handbook of Lasers and Optics, F. Träger (ed.), Springer, New York (2007).

[3] A. Knigge, G. Erbert, J. Jonsson, W. Pittroff, R. Staske, B. Sumpf, M. Weyers, and G. Tränkle, Electron. Lett. **41**, 250-251 (2005).

[4] M. Kanskar, T. Earles, T. Goodnough, E. Stiers, D. Botez, and L. Mawst, Electron. Lett. **41**, 245-247 (2005).

[5] R. C. Youngquist, S. Carr, and D. E. N. Davies, Opt. Lett. **12**, 158-160 (1987).

[6] K. W. Berndt, I. Gryczynski, and J. R. Lakowicz, Rev. Sci. Instrum. **61**, 1816-1820 (1990).

[7] L. V. Wang and H. Wu, Biomedical Imaging: Principles and Imaging, Wiley, New Jersey (2007).

[8] T. Kleine-Ostmann, P. Knobloch, M. Koch, S. Hoffmann, M. Breede, M. Hofmann, G. Hein, K. Pierz, M. Sperling, and K. Donhuijsen, Electron. Lett. **37**, 1461-1463 (2001).

[9] F. F. M. de Mul, J. van Spijker, D. van der Plas, J. Greve, J. G. Aarnoudse, and T. M. Smits, Appl. Opt. **23**, 2970-2973 (1984).

[10] C. A. Puliafito, T. F. Deutsch, J. Boll, K. To, Arch. Ophthalmol. **105**, 424-427 (1987).

[11] T. J. Dougherty, Sem. Surg. Oncol. **5**, 6-16 (1989).

[12] L. Longo, S. Evangelista, G. Tinacci, and A. G. Sesti, Las. Surg. Med. **7**, 444-447 (1987).

[13] A. Müller, S. Marschall, O. B. Jensen, J. Fricke, H. Wenzel, B. Sumpf, and P. E. Andersen, „Diode laser based light sources for biomedical applications," Laser Phot. Rev. **7**, 605-627 (2013).

[14] H. Wenzel, F. Bugge, M. Dallmer, F. Dittmar, J. Fricke, K.-H. Hasler, and G. Erbert, IEEE Photon. Technol. Lett. **20**, 214-216 (2008).

[15] K.-H. Hasler, B. Sumpf, P. Adamiec, F. Bugge, J. Fricke, P. Ressel, H. Wenzel, G. Erbert and G. Tränkle, IEEE Photon. Technol. Lett. **20**, 1648-1650 (2008).

[16] K. Paschke, S. Einfeldt, A. Ginolas, K. Häusler, P. Ressel, B. Sumpf, H. Wenzel, and G. Erbert, Conference on Lasers and Electro-Optics (CLEO), CMN4 (2008).

[17] W. Pittroff, G. Erbert, B. Eppich, C. Fiebig, K. Vogel, and G. Tränkle, IEEE Trans. Compon. Packag. Technol. **33**, 206-214 (2010).
[18] L. Goldberg, H. F. Taylor, J. F. Weller, and D. R. Scifres, Appl. Phys. Lett. **46**, 236-238 (1985).
[19] D. J. Derickson, R. J. Helkey, A. Mar, J. R. Karin, J. G. Wasserbauer, and J. E. Bowers, IEEE J. Quantum Electron. **28**, 2186-2202 (1992).
[20] C. Lin, P. L. Liu, T. C. Darnell, D. J. Eilenberger, and R. L. Hartman. Electron. Lett. **16**, 600-602 (1980).
[21] P. Unger, High Power Diode Lasers - Fundamentals, Technology, Applications, with contributions by numerous experts, R. Diehl (ed.), Springer, Berlin (2000).
[22] W. J. Alford, T. D. Raymond, and A. A. Allerman, J. Opt. Soc. Am. B **19**, 663-666 (2002).
[23] M. Behringer, High Power Diode Lasers: Technology and Applications, F. Bachmann, P. Loosen, and R. Poprawe (eds.), Springer, Berlin (2007).
[24] G. V. Agrawal and N. K. Dutta, Semiconductor Lasers 2nd Edition, Van Nostrand Reinhold, New York (1993).
[25] M. W. Fleming and A. Mooradian, IEEE J. Quantum Electron. **17**, 44-59 (1981).
[26] K. C. Harvey and C. J. Myatt, Opt. Lett. **16**, 910-912 (1991).
[27] R. W. Boyd, Nonlinear Optics 2nd Edition, Academic Press, San Diego (2003).
[28] H. Taniguchi, H. Ishii, R. Minato, Y. Ohki, T. Namegaya, and A. Kasukawa, IEEE J. Sel. Top. Quant. Electron. **13**, 1176-1179 (2007).
[29] B. Sumpf, M. Zorn, M. Maiwald, R. Staske, J. Fricke, P. Ressel, G. Erbert, M. Weyers, and G. Tränkle, Phot. Technol. Lett. **20**, 575-577 (2008).
[30] Nichia product list (2012). Available at: http://www.nichia.co.jp/en/product/laser.html (Accessed: 20 November 2012).
[31] B. Sumpf, K.-H. Hasler, P. Adamiec, F. Bugge, F. Dittmar, J. Fricke, H. Wenzel, M. Zorn, G. Erbert, and G. Tränkle, IEEE J. Sel. Top. Quantum Electron. **15**, 1009-1020 (2009).
[32] O. B. Jensen, P. E. Andersen, B. Sumpf, K.-H. Hasler, G. Erbert, and P. M. Petersen, Opt. Express **17**, 6532-6539 (2009).
[33] W. Denk, J. H. Strickler, and W. W. Webb, Science **248**, 73-76 (1990).
[34] P. D. Maker and R. W. Terhune, Phys. Rev. **137**, A801-A818 (1965).
[35] D. Huang, E. A. Swanson, C. P. Lin, J. S. Schuman, W. G. Stinson, W. Chang, M. R. Hee, T. Flotte, K. Gregory, C. A. Puliafito, and J. G. Fujimoto, Science **254**, 1178-1181 (1991).
[36] M.-W. Hsiung, B.-H. Kang, W.-F. Su, L. Pai, and H.-W. Wang, Ann. Otol. Rhinol. Laryngol. **112**, 534-539 (2003).

[37] Y. Kishimoto, S. Hirano, N. Kato, A. Suehiro, S.-I. Kanemaru, and J. Ito, Ann. Otol. Rhinol. Laryngol. **117**, 881-885 (2008).
[38] H. Miyazaki, J. Kato, H. Watanabe, H. Harada, H. Kakizaki, A. Tetsumura, A. Sato, and K. Omura, Oral Surg. Oral Med. Oral Pathol. Oral Radiol. Endod. **107**, 164-172 (2009).
[39] A. Knauer, G. Erbert, R. Staske, B. Sumpf, H. Wenzel, and M. Weyers, Semicond. Sci. Technol. **20**, 621-624 (2005).
[40] B. Sumpf, K.-H. Hasler, P. Adamiec, F. Bugge, J. Fricke, P. Ressel, H. Wenzel, G. Erbert, and G. Tränkle, Proc SPIE **7230**, 72301E (2009).
[41] M. Manasevit, Appl. Phys. Lett. **12**, 156-158 (1968).
[42] A. Y. Cho, J. R. Arthur, Jr., Prog. Solid State Chem. **10**, 157-192 (1975).
[43] P. Crump, G. Blume, K. Paschke, R. Staske, A. Pietrzak, U. Zeimer, S. Einfeldt, A. Ginolas, F. Bugge, K. Häusler, P. Ressel, H. Wenzel, and G. Erbert, Proc. SPIE **7198**, 719814 (2009).
[44] K.-J. Boller, B. Beier, and R. Wallenstein, High Power Diode Lasers - Fundamentals, Technology, Applications with contributions by numerous experts, R. Diehl (ed.), Springer, Berlin (2000).
[45] E. S. Kintzer, J. N. Walpole, S. R. Chinn, C. A. Wang, and L. J. Missaggia, IEEE Phot. Technol. Lett. **5**, 605-608 (1993).
[46] W. Both and J. Piprek, J. Therm. Anal. **36**, 1441-1456 (1990).
[47] G. Erbert, A. Bärwolff, J. Sebastian, and J. Tomm, High Power Diode Lasers - Fundamentals, Technology, Applications with contributions by numerous experts, R. Diehl (ed.), Springer, Berlin (2000).
[48] B. Sumpf, M. Maiwald, A. Müller, A. Ginolas, K. Häusler, G. Erbert, and G. Tränkle, IEEE Compon. Packag. Manuf. Technol. **2**, 116-121 (2012).
[49] M. Maiwald, A. Ginolas, A. Müller, A. Sahm, B. Sumpf, G. Erbert, and G. Tränkle, IEEE Phot. Technol. Lett. **20**, 1627-1629 (2008).
[50] M. G. Littman and H. J. Metcalf, Appl. Opt. **17**, 2224-2227 (1978).
[51] K. Liu and M. G. Littman, Opt. Lett. **6**, 117-118 (1981).
[52] H. Kogelnik and C. V. Shank, Appl. Phys. Lett. **18**, 152-154 (1971).
[53] B. E. A. Saleh and M. C. Teich, Fundamentals of Photonics, J. W. Goodman (Ed.), Wiley Interscience, New York (1991).
[54] S. Wang, IEEE J. Quantum Electron. **QE-10**, 413-427 (1974).
[55] J. Fricke, H. Wenzel, M. Matalla, A. Klehr, and G. Erbert, Semicond. Sci. Technol. **20**, 1149-1152 (2005).
[56] J. Fricke, W. John, A. Klehr, P. Ressel, L. Weixelbaum, H. Wenzel, and G. Erbert, Semicond. Sci. Technol. **27**, 055009 (2012).
[57] J. N. Walpole, Opt. Quantum Electron. **28**, 623-645 (1996).
[58] A. E. Siegman, DPSS (Diode Pumped Solid State) Lasers: Applications and Issues, M. Dowley (Ed.), Vol. 17 of OSA Trends in Optics and Photonics (Optical Society of America, 1998), paper MQ1.

[59] P. A. Franken, A. E. Hill, C. W. Peters, and G. Weinreich, Phys. Rev. Lett. **7**, 118-119 (1961).
[60] W. P. Risk, T. R. Gosnell, and A. V. Nurmikko, Compact Blue-Green Lasers, Cambridge University Press, Cambridge (2003).
[61] R. L. Sutherland, Handbook of Nonlinear Optics Second Edition, Revised and Expanded, Marcel Dekker Inc., New York (2003).
[62] J. A. Giordmaine, Phys. Rev. Lett. **8**, 19-20 (1962).
[63] P. D. Maker, R. W. Terhune, M. Nisenoff, and C. M. Savage, Phys. Rev. Lett. **8**, 21-22 (1962).
[64] I. Shoji, T. Kondo, A. Kitamoto, M. Shirane, and R. Ito, J. Opt. Soc. Am. B. **14**, 2268-2294 (1997).
[65] O. Gayer, Z. Sacks, E. Galun, and A. Arie, Appl. Phys. B **91**, 343-348 (2008).
[66] J. A. Armstrong, N. Bloembergen, J. Ducuing, and P. S. Pershan, Phys. Rev. **127**, 1918-1939 (1962).
[67] P. A. Franken and J. F. Ward, Rev. Mod. Phys. **35**, 23-39 (1963).
[68] M. Yamada, N. Nada, M. Saitoh, and K. Watanabe, Appl. Phys. Lett. **62**, 435-436 (1993).
[69] H. Ito, C. Takyu, and H. Inaba, Electron. Lett. **27**, 1221-1222 (1991).
[70] J. L. Jackel, C. E. Rice, and J. J: Veselka, Appl. Phys. Lett. **41**, 607-608 (1982).
[71] Y. S. Kim and R. T. Smith, J. Appl. Phys. **40**, 4637-4641 (1969).
[72] M. M. Fejer, G. A. Magel, D. H. Jundt, and R. L. Byer, IEEE J. Quantum Electron. **28**, 2631-2654 (1992).
[73] M. Iwai, T. Yoshino, S. Yamaguchi, M. Imaeda, N. Pavel, I. Shoji, and T. Taira, Appl. Phys. Lett. **83**, 3659-3661 (2003).
[74] G. D. Boyd and D. A. Kleinman, J. Appl. Phys. **39**, 3597-3639 (1968).
[75] L. G. Gouy, C. R. Acad. Sci. Paris **110**, 1251-1253 (1890).
[76] F. M. Librecht and J. A. Simons, IEEE J. Quantum Electron. **11**, 850-852 (1975).
[77] A. Steinbach, M. Rauner, F. C. Cruz, and J. C. Bergquist, Opt. Comm. **123**, 207-214 (1996).
[78] T. Freegrade, J. Coutts, J. Walz, D. Leibfried, and T. W. Hänsch, J. Opt. Soc. Am. B **14**, 2010-2016 (1997).
[79] M. Übernickel, R. Güther, G. Blume, C. Fiebig, K. Paschke, and G. Erbert, Appl. Phys. B **99**, 457-464 (2010).
[80] K. Kato, IEEE J. Quantum Electron. **QE-22**, 1013-1014 (1986).
[81] C. Chen,Y. Wu, A. Jiang, B. Wu, G.You, R. Li, and S. Lin, J. Opt. Soc. Am. B **6**, 616-621 (1989).
[82] I. Shoji, H. Nakamura, K. Ohdaira, T. Kondo, R. Ito, T. Okamoto, K. Tatsuki, and S. Kubota, J. Opt. Soc. Am. B. **16**, 620-624 (1999).

[83] C.-T. Chen, Y. Wu, A. Jiang, B. Wu, G. You, R. Li, and S. Lin, J. Opt. Soc. Am. B. **6**, 616-621 (1989).
[84] J. H. Lee, S. M. Lee, T. Kim, and Y. J. Park, Appl. Phys. Lett. **89**, 241107 (2006).
[85] T. Meier, B. Willke, and K. Danzmann, Opt. Lett. **35**, 3742-3744 (2010).
[86] B. Boulanger, I. Rousseau, J. P. Fève, M. Maglione, B. Ménaert, and G. Marnier, IEEE J. Quantum Electron. **35**, 281-286 (1999).
[87] A. Alexandrovski, M. Feijer, and G. Mitchell, Conference on Lasers and Electro-Optics (CLEO), CFF5 (1999).
[88] M. N. Satyanarayan, A. Deepthy, and H. L. Bhat, Crit. Rev. Solid State Mat. Sci. **24**, 103-191 (1999).
[89] H. Vanherzeele and J. D. Bierlein, Opt. Lett. **17**, 982-984 (1992).
[90] T. Y. Fan, C. E. Huang, B. Q. Hu, R. C. Eckardt, Y. X. Fan, R. L. Byer, and R. S. Feigelson, Appl. Opt. **26**, 2390-2394 (1987).
[91] J. D. Bierlein and H. Vanherzeele, J. Opt. Soc. Am. B **6**, 622-633 (1989).
[92] D. N. Nikogosyan, Nonlinear Optical Crystals: A Complete Survey, Springer, New York (2005).
[93] G. K. Samanta, S. Chaitanya Kumar, M. Mathew, C. Canalias, V. Pasiskevicius, F. Laurell, and M. Ebrahim-Zadeh, Opt. Lett. **33**, 2955-2957 (2008).
[94] A. Bruner, D. Eger, M. B. Oron, P. Blau, M. Katz, and S. Ruschin, Opt. Lett. **28**, 194-196 (2003).
[95] S. Sinha, D. S. Hum, K. E. Urbanek, Y.-W. Lee, M. J. F. Digonnet, M. M. Fejer, and R. L. Byer, J. Lightwave Technol. **26**, 3866-3871 (2008).
[96] G. D. Boyd, R. C. Miller, K. Nassau, W. L. Bond, and A. Savage, Appl. Phys. Lett. **5**, 234-236 (1964).
[97] K. Nakamura, T. Hatanaka, and H. Ito, Jpn. J. Appl. Phys. **40**, L337-L339 (2001).
[98] A. Ashkin, G. D. Boyd, J. M. Dziedzic, R. G. Smith, A. A. Ballman, J. J. Levinstein, and K. Nassau, Appl. Phys. Lett. **9**, 72-73 (1966).
[99] A. M. Glass, Opt. Eng. **17**, 470-479 (1978).
[100] D. A. Bryan, R. Gerson, and H. E. Tomaschke, Appl. Phys. Lett. **44**, 847-849 (1984).
[101] H. Furuya, A. Morikawa, K. Mizuuchi, and K. Yamamoto, Jpn. J. Appl. Phys. **45**, 6704-6707 (2006).
[102] C. Fiebig, S. Pekarek, K. Paschke, M. Übernickel, T. Südmeyer, U. Keller, and G. Erbert, Proc. SPIE **7918**, 79180R (2011).
[103] A. Müller, O. B. Jensen, K.-H. Hasler, B. Sumpf, G. Erbert, P. E. Andersen, and P. M. Petersen, Opt. Lett. **37**, 3753-3755 (2012).
[104] G. D. Miller, R. G. Batchko, W. M. Tulloch, D. R. Weise, M. M. Fejer, and R. L. Byer, Opt. Lett. **22**, 1834-1836 (1997).

[105] H. K. Nguyen, M. H. Hu, N. Nishiyama, N. J. Visovsky, Y. Li, K. Song, X. Liu, J. Gollier, L. C. Hughes Jr., R. Bhat, and C.-E. Zah, IEEE Phot. Technol. Lett. **18**, 682-684 (2006).
[106] K. Sakai, Y. Koyata, S. Itakura, and Y. Hirano, J. Lightwave Technol. **27**, 590-596 (2009).
[107] G. K. Samanta, S. C. Kumar, K. Devi, and M. Ebrahim-Zadeh, Opt. Lett. **35**, 3513-3515 (2010).
[108] S. Spiekermann, F. Laurell, V. Pasiskevicius, H. Karlsson, and I. Freitag, Appl. Phys. B **79**, 211-219 (2004).
[109] L. McDonagh and R. Wallenstein, Opt. Lett. **32**, 802-804 (2007).
[110] L. E. Hunziker, Q.-Z. Shu, D. Bauer, C. Ihli, G. J. Mahnke, M. Rebut, J. R. Chilla, A. L. Caprara, H. Zhou, E. S. Weiss, and M. K. Reed, Proc. SPIE **6451**, 64510A (2007).
[111] Z. Zhuo, T. Li, X. Li, and H. Yang, Opt. Comm. **274**, 176-181 (2007).
[112] W. J. Kozlovsky, C. D. Nabors, and R. L. Byer, IEEE J. Quantum Electron. **24**, 913-919 (1988).
[113] U. Brauch, P. Loosen, and H. Opower, High Power Diode Lasers - Fundamentals, Technology, Applications, with contributions by numerous experts, R. Diehl (ed.), Springer, Berlin (2000).
[114] A. Müller, D. Vijayakumar, O. B. Jensen, K.-H. Hasler, B. Sumpf, G. Erbert, P. E. Andersen, and P. M. Petersen, Opt. Express **19**, 1228-1235 (2011).
[115] T. Y. Fan, IEEE J. Sel. Top. Quantum Electron. **11**, 567-577 (2005).
[116] S. J. McNaught, C. P. Asman, H. Injeyan, A. Jankevics, A. M. Johnson, G. C. Jones, H. Komine, J. Machan, J. Marmo, M. McClellan, R. Simpson, J. Sollee, M. M. Valley, M. Weber, and S. B. Weiss, Frontiers in Optics, OSA Technical Digest (CD) (Optical Society of America, 2009), paper FThD2.
[117] C. X. Yu, S. J. Augst, S. M. Redmond, K. C. Goldizen, D. V. Murphy, A. Sanchez, and T. Y. Fan, Opt. Lett. **36**, 2686-2688 (2011).
[118] S. M. Redmond, D. J. Ripin, C. X. Yu, S. J. Augst, T. Y. Fan, P. A. Thielen, J. E. Rothenberg, and G. D. Goodno, Opt. Lett. **37**, 2832-2834 (2012).
[119] B. Liu, Y. Liu, and Y. Braiman, Opt. Express **18**, 7361-7368 (2010).
[120] B. Thestrup, M. Chi, B. Sass, and P. M. Petersen, Appl. Phys. Lett. **82**, 680-682 (2003).
[121] C. Wirth, O. Schmidt, I. Tsybin, T. Schreiber, R. Eberhardt, J. Limpert, A. Tünnermann, K. Ludewigt, M. Gowin, E. ten Have, and M. Jung, Opt. Lett. **36**, 3118-3120 (2011).
[122] C. Wirth, O. Schmidt, I. Tsybin, T. Schreiber, T. Peschel, F. Brückner, T. Clausnitzer, J. Limpert, R. Eberhardt, A. Tünnermann, M. Gowin, E. ten Have, K. Ludewigt, and M. Jung, Opt. Express **17**, 1178-1183 (2009).
[123] N. Lindlein and G. Leuchs, Springer Handbook of Lasers and Optics, F. Träger (ed.), Springer, New York (2007).

[124] V. Daneu, A. Sanchez, T. Y. Fan, H. K. Choi, G. W. Turner, and C. C. Cook, Opt. Lett. **25**, 405-407 (2000).
[125] D. Vijayakumar, O. B. Jensen, R. Ostendorf, T. Westphalen, and B. Thestrup, Opt. Express **18**, 893-898 (2010).
[126] B. Chann, R. K. Huang, L. J. Missaggia, C. T. Harris, Z. L. Liau, A. K. Goyal, J. P. Donnelly, T. Y. Fan, A. Sanchez-Rubio, and G. W. Turner, Opt. Lett. **30**, 2104-2106 (2005).
[127] O. Andrusyak, V. Smirnov, G. Venus, and L. Glebov, Opt. Comm. **282**, 2560-2563 (2009).
[128] O. M. Efimov, L. B. Glebov, V. I. Smirnov, and L. Glebova, United States Patent 6586141 (2003).
[129] O. Andrusyak, V. Smirnov, G. Venus, V. Rotar, and L. Glebov, IEEE Sel. Top. Quantum Electron. **15**, 344-353 (2009).
[130] H. Kogelnik, Bell Syst. Tech. J. **48**, 2909-2945 (1969).
[131] I. V. Ciapurin, D. R. Drachenberg, V. I. Smirnov, G. B. Venus, and L. B. Glebov, Opt. Eng. **51**, 058001 (2012).
[132] I. V. Ciapurin, L. B. Glebov, and V. I. Smirnov, Opt. Eng. **45**, 015802 (2006).
[133] O. Andrusyak, I. Ciapurin, V. Smirnov, G. Venus, N. Vorobiev, and L. Glebov, Proc. SPIE **6873**, 687314 (2008).
[134] I. Ciapurin, V. Smirnov, and L. Glebov, 17th Solid State and Diode Laser Technology Review (SSDLTR) Technical Digest, Beam-4 (2004).
[135] S. Helmfried and G. Arvidsson, J. Opt. Soc. Am. B **8**, 2326-2329 (1991).
[136] Y. Qu and S. Singh, Phys. Rev. A **47**, 3259-3263 (1993).
[137] J. Ohtsubo, Semiconductor Lasers Stability, Instability and Chaos, Springer, Berlin (2005).
[138] E. Karamehmedović, C. Pedersen, O. B. Jensen, and P. Tidemand-Lichtenberg, Appl. Phys. B **96**, 409-413 (2009).
[139] B. Shen, G. Zheng, J. Tan and Y. He, Opt. Eng. **50**, 074301 (2011).
[140] O. B. Jensen, A. K. Hansen, A. Müller, B. Sumpf, A. Unterhuber, W. Drexler, P. M. Petersen, and P. E. Andersen, IEEE J. Sel. Top. Quantum Electron. **20**, 7100515 (2013).
[141] E. Hecht, Optics Fourth Edition, Addison Wesley, San Francisco (2002).
[142] A. Müller, O. B. Jensen, A. Unterhuber, T. Le, A. Stingl, K.-H. Hasler, B. Sumpf, G. Erbert, P. E. Andersen, and P. M. Petersen, Opt. Express **19**, 12156 (2011).
[143] G. F. Albrecht, J. M. Eggleston, and J. J. Ewing, Opt. Comm. **52**, 401-404 (1985).
[144] P. F. Moulton, J. Opt. Soc. Am. B **3**, 125-133 (1986).
[145] A. Stingl, M. Lenzner, C. Spielmann, and F. Krausz, Opt. Lett. **20**, 602-604 (1995).

[146] P. Albers, E. Stark, and G. Huber, J. Opt. Soc. Am. B **3**, 134-139 (1986).
[147] G. T. Maker and A. I. Ferguson, Opt. Lett. **15**, 375-377 (1990).
[148] T. Imahoko, K. Takasago, M. Kamata, J. Sakuma, T. Sumiyoshi, H. Sekita and M. Obara, Appl. Phys. B **89**, 217-222 (2007).
[149] G. K. Samanta, C. K. Suddapalli, K. Devi, and M. Ebrahim-Zadeh, Conference on Lasers and Electro-Optics (CLEO), JTuD115 (2010).
[150] S. Takagi, Y. Enya, T. Kyono, M. Adachi, Y. Yoshizumi, T. Sumitomo, Y. Yamanaka, T. Kumano, S. Tokuyama, K. Sumiyoshi, N. Saga, M. Ueno, K. Katayama, T. Ikegami, T. Nakamura, K. Yanashima, H. Nakajima, K. Tasai, K. Naganuma, N. Fuutagawa, Y. Takiguchi, T. Hamaguchi, and M. Ikeda, Appl. Phys. Express **5**, 082102 (2012).
[151] S. Masui, T. Miyoshi, T. Yanamoto, S.-I. Nagahama, Conference on Lasers and Electro-Optics Pacific Rim (CLEO-PR), WH3-1 (2013).
[152] T. Gün, P. Metz, and G. Huber, Opt. Lett. **36**, 1002-1004 (2011).
[153] D. V. Tovstonog, S. Kurimura, I. Suzuki, K. Takeno, S. Moriwaki, N. Ohmae, N. Mio, and T. Katagai, Opt. Express **16**, 11294-11299 (2008).
[154] B. Resan, E. Coadou, S. Petersen, A. Thomas, P. Walther, R. Viselga, J.-M. Heritier, J. Chilla, W. Tulloch, and A. Fry, Proc. SPIE **6871**, 687116 (2008).
[155] P. W. Roth, A. J. Maclean, D. Burns, and A. J. Kemp, Optics Letters **36**, 304-306 (2011).
[156] P. W. Roth, D. Burns, and A. J. Kemp, Opt. Express **20**, 20629-20634 (2012).
[157] C. G. Durfee, T. Storz, J. Garlick, S. Hill, J. A. Squier, M. Kirchner, G. Taft, K. Shea, H. Kapteyn, M. Murnane, and S. Backus, Opt. Express **20**, 13677-13683 (2012)
[158] A. Unterhuber, B. Považay, B. Hermann, H. Sattmann, W. Drexler, V. Yakovlev, G. Tempea, C. Schubert, E. M. Anger, P. K. Ahnelt, M. Stur, J. E. Morgan, A. Cowey, G. Jung, T. Le, and A. Stingl, Opt. Lett. **28**, 905-907 (2003).
[159] J. F. Pinto, L. Esterowitz, G. H. Rosenblatt, M. Kokta, and D. Peressini, IEEE J. Quantum Electron **30**, 2612-2616 (1994).
[160] W. Sibbett, Nonlinear Optics in Signal Processing, R. W. Eason and A. Miller (Ed.), Chapman & Hall, London (1993).
[161] M. Wollenhaupt, A. Assion, and T. Baumert, Springer Handbook of Lasers and Optics, F. Träger (ed.), Springer, New York (2007).
[162] A. Unterhuber, B. Povazay, A. Müller, O. B. Jensen, T. Otto, I. Boettcher, M. Duelk, R. Kessler, R. Engelhardt, M. Esmaeelpour, T. Le, P. E. Andersen, C. Velez, G. Zinser, and W. Drexler, Opt. Lett. **38**, 4312-4315 (2013).
[163] D. Huang, E.A. Swanson, C.P. Lin, J.S. Schuman, W.G. Stinson, W. Chang, M.R. Hee, T. Flotte, K. Gregory, C.A. Puliafito, and J.G. Fujimoto, Science **254**, 1178-1181 (1991).

[164] M. E. Brezinski, Optical Coherence Tomography: Principles and Applications, Academic Press, Burlington (2006).
[165] R. Leitgeb, C. K. Hitzenberger and A. F. Fercher, Opt. Express **11**, 889-894 (2003).
[166] J. Mobley and T. Vo-Dinh, Biomedical Photonics Handbook, T. Vo-Dinh (ed.), CRC Press, Boca Raton (2003).
[167] A. W. Sainter, T. A. King, and M. R. Dickinson, J. Biomed. Opt. **9**, 193-199 (2004).
[168] E. A. Boettner and J. R. Wolter, Invest. Ophthalmol. Vis. Sci. **1**, 776-783 (1962).
[169] W. Drexler and J. G. Fujimoto, Prog Retin. Eye Res. **27**, 45-88 (2008).
[170] J. M. Olmedo, K. E. Warschaw, L. M. Schmitt, and D. L. Swanson, Dermatol. Surg. **33**, 421-426 (2007).
[171] T. Gambichler, G. Moussa, M. Sand, D. Sand, A. Orlikov, P. Altmeyer, and K. Hoffmann, J. Biomed. Opt. **10**, 064030-064035 (2005).
[172] J. Welzel, M. Bruhns, and H. H. Wolff, Arch. Dermatol. Res. **295**, 50-55 (2003).
[173] F. G. Bechara, T. Gambichler, M. Stücker, A. Orlikov, S. Rotterdam, P. Altmeyer, and K. Hoffmann, Skin Res. Technol. **10**, 169-173 (2004).
[174] A. T. Yeh, B. Kao, W. G. Jung, Z. Chen, J. S. Nelson, and B. J. Tromberg, J. Biomed. Opt. **9**, 248-253 (2004).
[175] A. Pagnoni, A. Knuettel, P. Welker, M. Rist, T. Stoudemayer, L. Kolbe, I. Sadiq, and A. M. Kligman, Skin Res. Technol. **5**, 83-87 (1999).
[176] S. M. Srinivas, J. F. de Boer, H. Park, K. Keikhanzadeh, H. E. Huang, J. Zhang, W. Q. Jung, Z. Chen, and J. S. Nelson, J. Biomed. Opt. **9**, 207-212 (2004).
[177] D. Komitowski, J. Investig. Dermatol. **78**, 395-401 (1982).

Appendix

The time-varying field of a plane wave propagating along the longitudinal axis z is expressed by the following relation [60]:

$$E_j(z,t) = A_j e^{i(k_j z - \omega_j t + \varphi_j)} + c.c. \tag{A1}$$

In case of SHG, an electric field E_2 incident on a nonlinear crystal induces an oscillating polarization P_4. According to the nonlinear wave equation [61],

$$-\frac{d^2E_j}{dz^2} + \frac{n_j^2}{c^2}\frac{\partial^2 E_j}{\partial t^2} = -\frac{1}{\varepsilon_0 c^2}\frac{\partial^2 P_j}{\partial t^2}, \tag{A2}$$

this induced polarization drives the generation of an additional electric field E_4, not originally present in the nonlinear medium. In case of SFG, two electric fields E_1 and E_3 induce an oscillating polarization P_5 generating an additional electric field E_5. Assuming that E_2 solely contributes to frequency doubling and E_1 and E_3 exclusively contribute to sum-frequency generation, results in a total of five electric fields

$$E_1(z,t) = A_1 e^{i(k_1 z - \omega_1 t + \varphi_1)} \tag{A3}$$

$$E_2(z,t) = A_2 e^{i(k_2 z - \omega_2 t + \varphi_2)} \tag{A4}$$

$$E_3(z,t) = A_3 e^{i(k_3 z - \omega_3 t + \varphi_3)} \tag{A5}$$

$$E_4(z,t) = A_4 e^{i(2k_2 z - \omega_4 t + 2\varphi_2)} \tag{A6}$$

$$E_5(z,t) = A_5 e^{i((k_1+k_3)z - \omega_5 t + (\varphi_1+\varphi_3))} \tag{A7}$$

and five induced nonlinear polarizations

$$P_1(z,t) = 4\varepsilon_0 d_{eff} A_5 A_3^* e^{i((k_5-k_3)z - \omega_1 t + \varphi_1)} \tag{A8}$$

$$P_2(z,t) = 4\varepsilon_0 d_{eff} A_4 A_2^* e^{i((k_4-k_2)z - \omega_2 t + \varphi_2)} \tag{A9}$$

$$P_3(z,t) = 4\varepsilon_0 d_{eff} A_5 A_1^* e^{i((k_5-k_1)z - \omega_3 t + \varphi_3)} \tag{A10}$$

$$P_4(z,t) = 2\varepsilon_0 d_{eff} A_2^2 e^{i(2k_2 z - \omega_4 t + 2\varphi_2)} \tag{A11}$$

$$P_5(z,t) = 4\varepsilon_0 d_{eff} A_1 A_3 e^{i((k_1+k_3)z - \omega_5 t + (\varphi_1+\varphi_3))} \tag{A12}$$

Solving the left side of the nonlinear wave equation, under the assumption of slowly varying amplitudes

$$\left|\frac{d^2A_j}{dz^2}\right| \ll \left|k_j \frac{dA_j}{dz}\right|, \tag{A13}$$

and

$$k_j = \frac{n_j \omega_j}{c}, \tag{A14}$$

results in the following expression

$$\begin{aligned} -\nabla^2 E_j + \frac{n_j^2}{c^2}\frac{\partial^2 E_j}{\partial t^2} = & -2\frac{dA_1}{dz} i k_1 e^{i(k_1 z - \omega_1 t + \varphi_1)} \\ & -2\frac{dA_2}{dz} i k_2 e^{i(k_2 z - \omega_2 t + \varphi_2)} \\ & -2\frac{dA_3}{dz} i k_3 e^{i(k_3 z - \omega_3 t + \varphi_3)} \\ & -2\frac{dA_4}{dz} i k_4 e^{i(k_4 z - \omega_4 t + 2\varphi_2)} \\ & -2\frac{dA_5}{dz} i k_5 e^{i\left(k_5 z - \omega_5 t + (\varphi_1 + \varphi_3)\right)}. \end{aligned} \tag{A15}$$

Assuming a coherent summation of nonlinear interactions ($k = k_4 = k_5$, $\omega = \omega_4 = \omega_5$, and $\varphi = 2\varphi_2 = \varphi_1 + \varphi_3$) the left side of the nonlinear wave equation can be simplified to

$$\begin{aligned} -\nabla^2 E_j + \frac{n_j^2}{c^2}\frac{\partial^2 E_j}{\partial t^2} = & -2\frac{dA_1}{dz} i k_1 e^{i(k_1 z - \omega_1 t + \varphi_1)} \\ & -2\frac{dA_2}{dz} i k_2 e^{i(k_2 z - \omega_2 t + \varphi_2)} \\ & -2\frac{dA_3}{dz} i k_3 e^{i(k_3 z - \omega_3 t + \varphi_3)} \\ & -2ik\left(\frac{dA_4}{dz} + \frac{dA_5}{dz}\right) e^{i(kz - \omega t + \varphi)}. \end{aligned} \tag{A16}$$

The right side of the nonlinear wave equation results in

$$\begin{aligned} -\frac{1}{\varepsilon_0 c^2}\frac{\partial^2 P}{\partial t^2} = & \frac{4 d_{eff} A_5 A_3^* \omega_1^2 e^{i\left((k_5 - k_3)z - \omega_1 t + \varphi_1\right)}}{c^2} \\ & + \frac{4 d_{eff} A_4 A_2^* \omega_2^2 e^{i\left((k_4 - k_2)z - \omega_2 t + \varphi_2\right)}}{c^2} \\ & + \frac{4 d_{eff} A_5 A_1^* \omega_3^2 e^{i\left((k_5 - k_1)z - \omega_3 t + \varphi_3\right)}}{c^2} \\ & + \frac{2 d_{eff} A_2^2 \omega_4^2 e^{i(2k_2 z - \omega_4 t + 2\varphi_2)}}{c^2} \\ & + \frac{4 d_{eff} A_1 A_3 \omega_5^2 e^{i\left((k_1 + k_3)z - \omega_5 t + (\varphi_1 + \varphi_3)\right)}}{c^2} \end{aligned} \tag{A17}$$

Neglecting all contributions that are not phase-matched results in the following coupled amplitude equations

$$\frac{dA_1}{dz} = i\frac{2\omega_1 d_{eff}}{n_1 c} A_5 A_3^* e^{i(k_5 - k_3 - k_1)z} \tag{A18}$$

$$\frac{dA_2}{dz} = i\frac{2\omega_2 d_{eff}}{n_2 c} A_4 A_2^* e^{i(k_4 - 2k_2)z} \tag{A19}$$

$$\frac{dA_3}{dz} = i\frac{2\omega_3 d_{eff}}{n_3 c} A_5 A_1^* e^{i(k_5 - k_1 - k_3)z} \tag{A20}$$

$$\frac{dA}{dz} = \frac{dA_4}{dz} + \frac{dA_5}{dz} = i\frac{d_{eff}\omega e^{i\Delta kz}}{nc}(A_2^2 + 2A_1 A_3). \tag{A21}$$

The equations (A18) - (A20) represent the coupled amplitude equations that take the depletion of the three fundamental waves into account [27]. The last equation represents the coupled amplitude equation for simultaneous SHG and SFG. The corresponding intensity is obtained by integration over the entire crystal length:

$$\begin{aligned} A_2(L) &= i\frac{d_{eff}\omega}{nc}(A_2^2 + 2A_1 A_3)\int_0^L e^{i\Delta kz}\, dz \\ &= i\frac{d_{eff}\omega}{nc}(A_2^2 + 2A_1 A_3)\left(\frac{e^{i\Delta kL} - 1}{i\Delta k}\right). \end{aligned} \tag{A22}$$

Substituting the amplitudes with

$$I = 2n\varepsilon_0 c|A|^2. \tag{A23}$$

results in

$$I = i\frac{2\varepsilon_0 d_{eff}^2 \omega^2}{nc}|A_2^2 + 2A_1 A_3|^2 \left|\frac{e^{i\Delta kL} - 1}{i\Delta k}\right|^2 \tag{A24}$$

and

$$\begin{aligned} I = &\frac{2\pi^2 d_{eff}^2}{n n_2^2 \lambda^2 \varepsilon_0 c} I_2^2 L^2\, sinc^2\left(\frac{\Delta kL}{2}\right) \\ &+ \frac{8\pi^2 d_{eff}^2}{n n_1 n_3 \lambda^2 \varepsilon_0 c} I_1 I_3 L^2\, sinc^2\left(\frac{\Delta kL}{2}\right) \\ &+ \frac{4\pi^2 d_{eff}^2}{n\lambda^2 \varepsilon_0 c}\frac{I_2\sqrt{I_1 I_3}}{n_2\sqrt{n_1 n_3}} L^2\, sinc^2\left(\frac{\Delta kL}{2}\right), \end{aligned} \tag{A25}$$

respectively. This last equation consists of individual contributions from SHG and SFG and a third coupling term. Considering the above scenario of matching frequencies and phases, this third term represents the contribution from occurring

interference effects. However, because the superposition of coherent waves does not alter the total intensity this increase is always compensated [141]. The average intensity in case of simultaneous nonlinear interactions is therefore always determined by the summation of the individual contributions.